Nanomaterial-Enabled Out-of-Autoclave and Out-of-Oven Manufacturing of Fiber Reinforced Polymer Composites

by

Steven Serrano

S.B., Massachusetts Institute of Technology (2022)

Submitted to the Department of Aeronautics and Astronautics
in partial fulfillment of the requirements for the degree of

Master of Science in Aeronautics and Astronautics

at the

MASSACHUSETTS INSTITUTE OF TECHNOLOGY

September 2023

Author . . . .
Department of Aeronautics and Astronautics
August 15, 2023

Certified by . . . .
Brian L. Wardle
Professor of Aeronautics and Astronautics, Professor of Mechanical Engineering
Thesis Supervisor

Accepted by . . . .
Jonathan How
Chair, Graduate Program Committee

Nanomaterial-Enabled Out-of-Autoclave and Out-of-Oven Manufacturing of Fiber Reinforced Polymer Composites

by

Steven Serrano

Submitted to the Department of Aeronautics and Astronautics
on August 15, 2023, in partial fulfillment of the
requirements for the degree of
Master of Science in Aeronautics and Astronautics

Abstract

Fiber reinforced polymer composite materials have been a staple of the aerospace industry, integral to creating lightweight flight vehicles due to their high specific material properties. These materials often come in a prepreg form, where microfibers are pre-impregnated with a polymer matrix to form lamina that are stacked to form a composite laminate. These aerospace-grade composite structures generally require an autoclave cure, which uses both temperature and pressure to cure the thermoset polymer (or consolidate the thermoplastic polymer) in the prepreg and remove voids throughout the laminate. In this thesis, curing of autoclave-grade thermosetting prepregs using vacuum-bag only (VBO) processes are investigated and further developed through the employment of nanomaterials, both within the laminate itself and externally as a conductive heating mechanism. A preliminary void reduction study was conducted on the effects of placing different nanoporous networks (NPNs) in the interlaminar regions of a VBO manufactured quasi-isotropic laminate using autoclave-grade glass fiber reinforced polymer (GFRP) unidirectional prepreg. It was shown that vertically aligned carbon nanotubes (VA-CNTs), electrospun polymer nanofiber (EPN) veils, and polyimide (PI) aerogel thin films may each successfully evacuate voids via capillary-pressure enhanced polymer flow, as the laminate was void-free. A subsequent study placing PI aerogel NPN in each interlaminar region was shown to successfully create a void-free GFRP laminate on a hot plate using VBO manufacturing. Autoclave woven CFRP prepreg laminates were also manufactured using the same VBO with NPN technique, with PI aerogel in each interlaminar region. Laminates were shown to have minimal void content (< 0.03 vol%) using an advantageously thinner aerogel film than previous work. A previously studied out-of-oven (OoO) curing process using a carbon nanotube (CNT) thin film heating element was modeled using ANSYS Composite Cure Simulation (ACCS) to predict the temperature and degree of cure (DoC) of CFRP laminates using cure kinetics equations and the finite element method. The Limited-memory Broyden-Fletcher-Goldfarb-Shanno with Bound constraints (L-BFGS-B) algorithm was implemented to optimize the cure cycle with respect to time and DoC constraints. Two optimized cure cycles were revealed via the optimization scheme, showing significant (60% to 65%) reductions in manufacturing time. A third accelerated-cure cycle did not use the optimization scheme, but rather utilized an empirical estimation of resin rheology, time history of temperature, and DoC to obtain a cure cycle that had comparable resin flow to that of the manufacturer recommended cure cycle (MRCC) per a defined flow metric. Laminates utilizing the three accelerated cures, the MRCC cure, and a cure with an extended first hold were all modeled in ANSYS and manufactured with a CNT heater OoO set-up and an EPN NPN. The model was found to overestimate the DoC of the manufactured 152 mm x 152 mm x 2 mm (16 ply) laminates by ∼5% on average. The accelerated-cure laminates were shown to have a relatively high void content, indicating that additional considerations are necessary to successfully accelerate the VBO CFRP cure cycle. However, the laminate cured with an extended first hold, as well as the MRCC laminate, were found to have minimal void content (0.02 vol% and 0.08 vol%, respectively). Furthermore, the accelerated-cure laminate with a second hold of 200°C for 36.5 minutes was found to yield a nominal DoC (90.5%) and a comparable glass transition temperature (T_g) to that of the MRCC cured laminate. Together, the results found in this work show that nanomaterials (i.e. NPNs and CNT heating elements) enable the VBO manufacturing of several types of autoclave prepregs and improve manufacturing throughput via cure cycle modifications that can allow significant acceleration of the overall cure cycle.

Thesis Supervisor: Brian L. Wardle
Title: Professor of Aeronautics and Astronautics, Professor of Mechanical Engineering

Acknowledgments

Closing in on 5 years at MIT, it has been nothing but a truly fulfilling experience. I have been given the amazing opportunity to grow as a student, researcher, athlete, and person, and I have many people to thank for this. First and foremost, I would like to thank the PI, the professor, and most of all, the wonderful mentor that Professor Brian L. Wardle is to me. He took a chance on me in my third year of undergrad, and from that moment in time it has been nothing but a pleasure to work with his amazing guidance. His amazing and positive attitude toward academia was extremely motivating and made it less intimidating for a first-generation student like myself to pursue higher education. I am thankful for all the help he has given me in advancing my knowledge, and I am forever grateful to have been given the opportunity to grow in ways I did not think were possible.

Moreover, the author and thesis supervisor would like to thank Saab AB for donation of the AS4/8552 UD CFRP prepreg, Hexcel (France) for donation of the EC9/913 UD GFRP prepreg, and Dr. Seth Kessler and Dr. Estelle Kalfon-Cohen from Metis Design Corporation for their expertise and donation of CNT heaters.

I would like to thank my fellow labmates at necstlab for the amazing experience during my time in graduate school. Palak was my number one help, answering hundreds of questions for no reason other than the goodness in her heart. Carina, Jingyao, and Carolina were the postdocs that poured their vast knowledge into questions I would ask them and were extremely helpful in advancing projects I was lucky enough to work on. Chris, Shaan, Alisa, Yuying, you four made me feel at home, and I am thankful for the shared laughs and struggles we had together. Luiz, I'm thankful for your really good chicken hearts and for showing me the cool developments you made. Erick, thanks for being there to help with experiments when I needed it most, and for reminding me of sweet home Chicago. For those I did not mention, I am very grateful for all the lab outing experiences we were able to share together. I could not be more thankful to have the amazing support system I did at necstlab.

I would like to thank my friends from home in the Chicagoland area, who de-

spite the 1000-mile distance, continued to keep our bond: Arthur, Mike, Jovanni, Mohamed, Stan, Eyad, and Omar. Every time I came back home, I looked forward to spending time together with them. They have been very much the group I turned to when times got tough, keeping me grounded through it all. I am forever grateful for the support shown to me no matter the changes in our lives, and I am thankful for the encouragement this group has given me in all of my endeavors.

Lastly, I would like to thank my loving and supportive family: my beloved mother, Ada Serrano, my wonderful father Rigoberto Serrano, and my admirable sister Jasmine Serrano. They all have been extremely supportive of every dream, goal, and journey I have striven to accomplish. I am extremely proud to have them as my family, and I am so thankful for all the times they were there for me, no matter the circumstance. My parents both fought tooth and nail to see me fly, and I hope that my 5 years here at MIT can resemble a tiny piece of the hard work the two of them have completed to raise me as immigrants with very little to start with. Jasmine has been and is an amazing role model and someone I look up to, and I am truly thankful to have a sister that is so supportive. I learned a lot from the experiences she had to face as the older sibling, and I am grateful to have been guided by her strong wisdom. I am especially grateful for the grit and determination my family has instilled in me, demonstrating how obstacles can be overcome with proper hard work and dedication. Without my family, I would not be half the person I am today, and I am truly grateful for their presence in my life.

I am grateful to everyone listed above and not, who have assisted me in arriving at this point in my career. It is truly a group effort.

"We choose to go to the moon in this decade and do the other things, not because they are easy, but because they are hard."
- John F. Kennedy

Contents

List of Figures

THIS PAGE INTENTIONALLY LEFT BLANK

List of Tables

Abbreviations and Symbols

ASTM	American Society for Testing and Materials
ACCS	ANSYS Composite Cure Simulation (software)
CFRP	carbon fiber reinforced polymer/plastic
CNT	carbon nanotube
CVD	chemical vapor deposition
DE	differential evolution (algorithm)
DoC	degree of cure of thermoset polymer
DMA	dynamic mechanical analysis
DSC	differential scanning calorimetry
EPN	electrospun polymer nanofiber
FEA	finite element analysis
FRP	fiber reinforced polymer
GFRP	glass fiber reinforced polymer/plastic
GNPT	guaranteed non-porous Teflon
$\boldsymbol{\Delta H}$	heat of reaction
MRCC	manufacturer recommended cure cycle
$\boldsymbol{N_{flow}}$	resin flow coefficient
NPN	nanoporous network

L-BFGS-B	Limited-memory Broyden-Fletcher-Goldfarb-Shanno with Bound constraints (optimization method)
$\boldsymbol{\eta}$	viscosity
OoO	out-of-oven
OoA	out-of-autoclave
PEEK	polyether ether ketone
PI	polyimide
PID	proportional integral derivative (control)
SBS	short beam shear
SEM	scanning electron microscopy
VA-CNT	vertically aligned carbon nanotube (forest)
VBO	vacuum-bag only
µCT	micro-computed (x-ray) tomography
$\boldsymbol{T_g}$	glass transition temperature
$\boldsymbol{t}$	time
$\boldsymbol{T}$	temperature

Chapter 1

Introduction

The motivation for the nanoengineered manufacturing of composites in this work is provided, followed by an overview of the thesis.

1.1 Motivation

The aerospace industry has always sought to reduce weight on both aircraft and spacecraft alike. Weight reduction in flight vehicles results in savings in other areas, such as batteries or fuel, in addition to payload. This drives the need for advanced materials that allow for these system level improvements. Advanced composite materials have been engineered to achieve these improvements by harnessing the superior mechanical properties of high aspect ratio microfibers (∼200-800 GPa stiffness for carbon fibers) [1, 2] and expanding them to the macroscale via composite laminae and laminates. An individual composite lamina typically consists of a sheet of parallel or woven microfibers (commonly carbon or glass fibers) pre-impregnated with a thermoset or thermoplastic polymer, most often a thermoset B-staged epoxy resin. When these laminae are stacked together and cured, they form an advanced composite laminate structure. Although noted to be more expensive to process compared to their metal counterparts [3], these composite structures have superior in-plane specific properties compared to other industry standard materials, such as aluminum and stainless steel, and are therefore well-suited for aerospace applications [4]. Along with their high specific strength and moduli, composite structures also provide high resistance to fatigue [5] and corrosion [6]. Furthermore, composite materials also provide the advantage of being highly tailorable to specific geometries and directional material properties, allowing for further simplifications in design as well as the reduction of parts and fasteners [7].

Composite materials are playing an increasing role in the structural make-up of important industries [8–10]. A major industry that utilizes these materials is aviation, where industry leaders such as Boeing with the 787 Dreamliner [11] and Airbus with the AX350 [12] comprise their airplanes of over 50% advanced composites by weight. In any context, but particularly with global imperatives toward sustainability and energy efficiency, it is imperative to develop highly efficient and effective solutions to the manufacturing of composite materials today.

Autoclave curing of prepreg composites is currently the most practiced method for curing aerospace-grade composites. It involves subjecting a prepreg layup to elevated temperature and pressure in order to cure the thermoset resin present in the composite (or consolidate a thermoplastic). For smaller components, this is manageable, but as the components become larger, on the order of magnitude of an airplane wing, larger autoclave pressure vessels are required to cure these structures. Not only is it difficult to conduct this process due to geometric constraints, it results in high energy consumption, as the autoclaves require an elevated temperature and pressure environment in a broad volume of space to cure the composites using inefficient convection.

A secondary method that has become prevalent in the composites realm today is known as Out-of-Autoclave (OoA) curing. An alternative prepreg designed to be cured under vacuum-bag only (VBO) conditions is used for laminates cured in an oven, with pressure applied to the composite only due to the vacuum being pulled during cure (atmospheric pressure) [13]. A comparison between autoclave and OoA manufacturing processes for composite prepreg is shown in Fig. 1-1.

Such VBO OoA prepregs can eliminate the need for autoclave pressure. However, the high energy involved in the heating of the entire oven volume to heat the composite

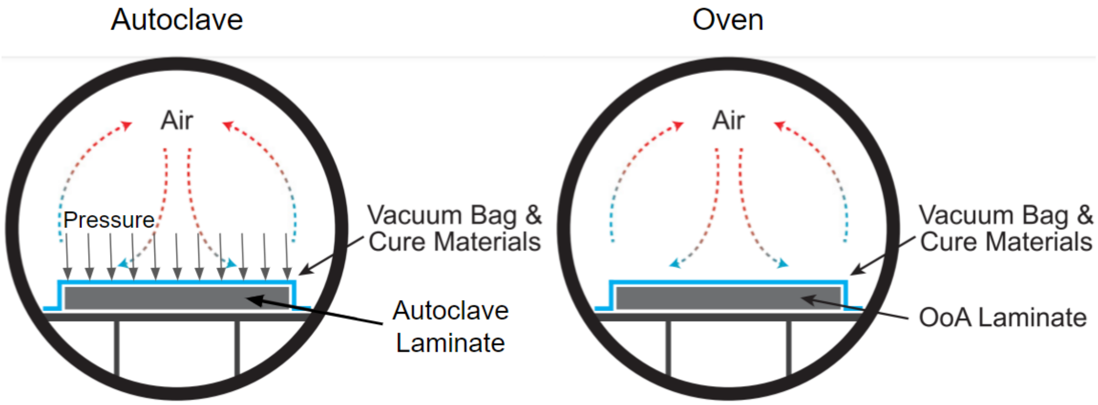

Figure 1-1: Comparison of autoclave and OoA manufacturing processes for FRP composites. OoA requires a special prepreg designed for low-pressure conditions. Figure adapted from [14].

via convection, as well as geometric constraints, continue to be an issue for OoA systems. Furthermore, autoclave prepregs have more flight heritage and reliability compared to OoA prepregs, and autoclave prepregs are more robust, as OoA systems currently struggle to maintain their quality. If key parameters in the curing process are not met, laminate quality decreases significantly, particularly in properties associated with the resin-rich interlaminar (inter-ply) regions [15].

Alternative methods have been conceived for curing composites, without the requirement of large machinery, each with its own advantages and disadvantages. Both high-energy electromagnetic radiation (gamma ray, X-ray, ultraviolet, accelerated electron beams) and thermal curing (conduction, thermal radiation) techniques for composite manufacturing have been explored extensively in both academia and industry [16]. A leading alternative method involves utilizing the conductive heating of thin carbon nanotube (CNT) films and, via their favorable thermal [17–20] and electrical [21–25] properties, applying resistive heating to cure the composite, in a process known as Out-of-Oven (OoO) curing [14, 22, 26, 27]. Through this heating process, OoA prepregs can be cured into void-free composite parts while also saving thermal energy. A comparison of oven-curing and OoO curing is shown in Fig. 1-2. This process can now also be taken a step further, using autoclave-formulated prepregs instead of OoA prepregs, through the use of nanoporous networks (NPNs) as an alternative way to achieve high pressures in the interlaminar region between plies of woven and unidirectional prepreg [28–30]. A comparison between autoclave and OoO with NPN processing is shown in Fig. 1-3. While void removal is made possible via these NPNs, further study is required on the mechanical properties of OoO and VBO (via NPN) curing of autoclave-formulated prepreg FRP laminates, as well as the optimal curing conditions for the OoO technology.

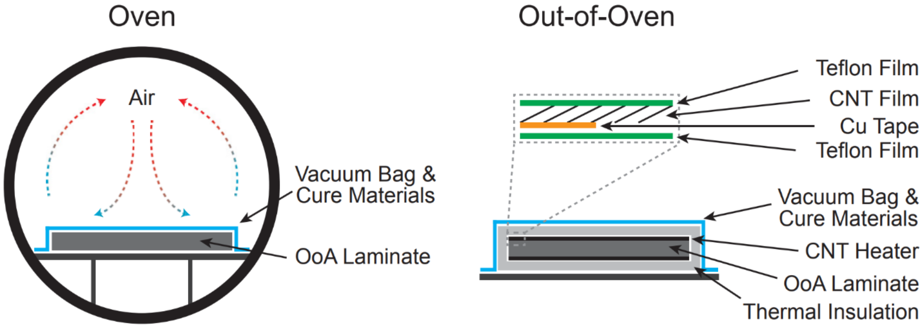

Figure 1-2: Comparison of oven and Out-of-Oven (OoO) manufacturing processes for OoA prepreg laminate curing. OoO allows for direct contact with the laminate, leading to significant energy savings. Figure from [14].

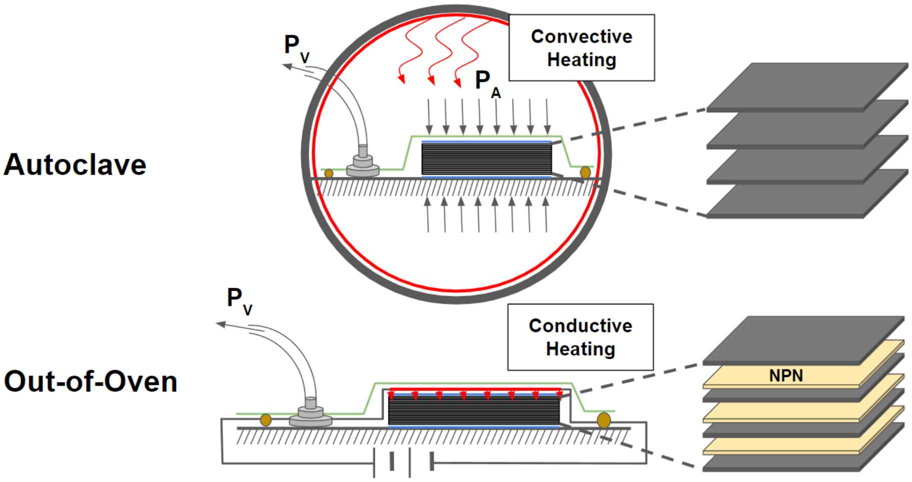

Figure 1-3: Comparison of autoclave (top) and Out-of-Oven (bottom) manufacturing processes for autoclave prepreg laminate curing. OoO allows for direct contact with the laminate, leading to significant energy savings. OoO with autoclave prepreg is enabled by nanoporous network (NPN) sheets in the interlaminar region that provide capillary pressure.

1.2 Thesis Outline

The main purpose of this thesis is to investigate the ability of nanomaterials to enable the Out-of-Autoclave and Out-of-Oven manufacturing of several kinds of prepregs intended for autoclaves, without the loss of mechanical properties, as well as to further optimize the OoO process by harnessing the ability of the CNT resistive heating mechanism to achieve accelerated cure cycles.

Chapter 2 provides a background on the variety of curing techniques tested and used to cure fiber reinforced polymer (FRP) composites, as well as background on NPNs, accelerated curing of FRP composites, and ANSYS Composite Cure Simulation.

Chapter 3 provides the objectives of this thesis, as well as the general approach taken to achieve the objectives.

Chapter 4 contains the results of an in-depth study on the use of NPNs in three new material systems and configurations: oven-cured autoclave woven Carbon Fiber Reinforced Polymer (CFRP) prepreg in flat laminates, oven-cured autoclave unidirectional Glass Fiber Reinforced Polymer (GFRP) prepreg in quasi-isotropic flat laminates, and oven-cured autoclave unidirectional CFRP prepreg in quasi-isotropic L-shaped laminates.

Chapter 5 contains the modeling results using ANSYS Composite Cure Simulation (ACCS) and optimization in Python that were used to inform cure cycle design decisions for an accelerated cure of CFRP autoclave prepreg via the OoO with NPN manufacturing approach. The resulting optimized cure cycle is then used in manufacturing CFRP laminates, and testing is conducted to check for maintained mechanical properties.

Chapter 6 summarizes the findings of the previous chapters and outlines future work based on the findings.

THIS PAGE INTENTIONALLY LEFT BLANK

Chapter 2

Background

Traditional aerospace advanced composite curing methods consist of the autoclave method as well as the more recent oven and vacuum-bag only (VBO) method with out-of-autoclave (OoA) prepreg. While used extensively, these traditional curing methods utilize convective heating and require a pressure vessel (autoclave) to provide the temperature and pressure required to cure the composite laminates. Alternate curing methods consist of radiation curing (electron beam, gamma-ray, X-ray, ultraviolet), radiation heating (infrared, laser, microwave), and conductive heating (Out-of-Oven curing, hot plate, electrical, etc.), each with their own benefits and drawbacks [16]. Out-of-Oven (OoO) curing is especially of interest, as it has the ability to achieve accelerated curing cycles by utilizing favorable thermal and electrical properties of CNTs, while also having demonstrated energy efficiency. Other accelerated curing techniques can provide advantages in the throughput of components, but each also has its own advantages and disadvantages. Alternative curing methods often face challenges due to the absence of applied pressure, which plays a crucial role in ensuring the quality of laminates, particularly the mechanical properties of the matrix-rich interlaminar region. As a result, alternative options such as nanoporous networks (NPNs) have gained considerable attention. NPNs have been shown to enable the OoO process for autoclave prepregs, providing pressures comparable to autoclave pressure within the interlaminar region. Since the OoO curing cycle can be accelerated, optimization algorithms can be applied (here via ANSYS

Composite Cure Simulation and Python scripting) to achieve an optimal curing cycle with respect to time, while maintaining a set Degree of Cure (DoC), among other quality-assuring constraints (see Chapter 5).

2.1 Traditional Curing Methods for FRPs

Autoclaves are temperature and pressure-controlled vessels that create the necessary environmental conditions for convective curing of advanced polymer matrix composites (PMCs). They are known for producing high quality parts with low void content and high fiber volume fractions [7, 16, 31–33], and thus, have been studied for decades, increasing their reliability over time. B-staged thermosetting epoxy-based FRP composite laminates are placed on a tooling base and caul plate, vacuum is pulled in order to evacuate enclosed air and volatiles within the laminate, and the laminate is subjected to the manufacturer-recommended cure cycle (MRCC) temperature and pressure (vacuum pressure plus autoclave pressure) conditions that are highly reproducible [34].

Although autoclaves are known to produce the highest quality prepreg laminates, they suffer from several issues stemming from the use of convective curing. Autoclave cured parts are susceptible to temperature gradients [35, 36] that cause variability in composite DoC [35], leading to, among other issues, warped parts and residual stresses. Furthermore, convective curing requires a large volume of space (relative to the part volume) to be brought to the same temperature and pressure, and most of that energy is completely lost in the energy inefficient process of heating the working fluid (usually air, sometimes with additional nitrogen), the tooling, and the vessel itself. The autoclave pressure vessel also poses challenges as the size of parts increases. The need for larger autoclaves to accommodate these larger parts creates geometric constraints and substantially raises the manufacturing costs [37].

More recently, the OoA method has become more prevalent, due to its ability to produce composites that are mechanically competitive to autoclave cured composites [38]. While OoA is a general term referring to many processes that do not require an autoclave (such as infusion), it usually refers to prepreg composites cured with an oven without the pressure of an autoclave. Although very similar to the autoclave process, the key difference in the OoA method is that OoA prepregs do not require external pressure as autoclave prepregs do, a result of developments in both prepreg ply design and in resin chemistry that make the cure kinetics suitable for OoA curing [39]. Specifically, the resin formulation is adjusted such that the viscosity profile of the resin employed is altered, and/or intentional dry regions in OoA prepreg serve as void extraction channels [15, 40, 41]. Further adjustments such as a modified layup process, a debulking step where vacuum is pulled at room temperature, and an altered cure cycle are what make the OoA process feasible [42]. This allows for OoA prepreg to be used in a wider range of potential heating mechanisms, such as oven curing and conductive curing, among many others [14, 43].

Although the potential is high for the OoA process to become the manufacturing process of the aerospace industry, OoA manufacturing currently does not come without disadvantages. The quality of resulting OoA laminates decreases more significantly compared to autoclave laminates if manufacturing conditions are not nominal [15, 38], creating challenges in quality control. Also, as OoA prepregs are frequently cured in ovens, the OoA manufacturing process faces the same geometric constraint issues characteristic of autoclave pressure vessels: substantial energy requirements, geometric constraints, and variability in laminate temperature during cure.

2.2 Alternative Curing Methods for FRPs

Several alternative curing methods exist for FRPs and composites in general. Focusing here on the most prevalent thermosetting epoxy class of polymers, alternative methods for curing resins in FRPs can be distinguished into three categories: radiation curing, radiation heating, and conductive heating [16].

Radiation curing is the curing of composites by the ionization of radiation sensitive polymers, using high-energy electromagnetic radiation (electron beam, gamma-ray, X-ray, ultraviolet) to achieve the bond breakage of the polymers. Each of these requires a resin that is also radiation sensitive, allowing for ionic or free radical intermediates to initiate crosslinking polymerization [44, 45]. Electron beam radiation involves accelerating electrons into the composite to provide the necessary energy for initiating the curing process. Gamma-ray and x-ray curing work similarly to achieve initiation of the polymerization process [46, 47]. Ultraviolet (UV) curing involves using UV light to cure the composite, however, the UV light does not have a high penetration depth compared to other radiation curing techniques, so transparent and thin composites are the main targets for this method.

Radiation curing is well suited for curing thicker parts [48, 49], has a significant increase in material throughput, allows for different kinds of matrix resins in the same composite laminate, reduces volatile emissions, provides additional control, and enables low temperature curing that can reduce resulting internal stresses in the composite [45]. However, it can also have geometric issues as parts become large, as proper shielding from radiation is required to house the part and complete the cure. Lower mechanical properties compared to thermal curing techniques are still a prevalent issue [50], and manufacturing difficulties, such as ineffective void evacuation due to the lack of pressure, continue to be a problem.

Radiation heating involves using electromagnetic radiation converted into heat to achieve the necessary temperatures to induce exothermic reactions and polymerization of the polymer matrix. Infrared, laser, and microwave heating all initially heat the surface but do not penetrate through the material. Reliance on conduction from the surface into the laminate causes radiation heat curing to suffer from cure imbalances [16, 51], as the surface needs to be heated to a high temperature to successfully cure thick regions, and if precise conditions are not met, over-curing can occur at the surface. Furthermore, the lack of pressure employed using radiation heating mechanisms can also result in high void content [51].

Conductive heating of aerospace-grade composite laminates is another alternative technique that has been broadly studied. Hot presses are the most common version, as they can provide both heat and pressure while curing the composite, similar to autoclaves [52]. However, this process is limited to relatively flat components due to the geometric constraint set by the hot press itself. Induction heating has been studied not only as a curing mechanism but also for welding thermoplastics [53]. It involves harnessing eddy currents that enable resistive and dielectric heating, as well as magnetic hysteresis that enables heating via friction losses. However, to achieve induction heating, particles generally must be introduced into the composite in relatively high quantities (50% by weight in [54]), which can lead to losses in specific mechanical properties. Carbon fibers are electrically conductive, which allows for induction heating without the additional introduction of particles. However, the exact heating mechanism isn't perfectly clear [16], as there are several potential avenues of heat generation via induction heating, and also, induction heating has not been successfully applied at a large scale. Ultrasonic heating involves using mechanical vibrations to induce friction heating, but also has severe consequences on part quality, as the vibrations can cause damage to the fibers. Thin sized nanomaterial heaters have also been utilized as an external application of heat onto FRP composites, as their low thermal mass allows for minimized energy loss, and they contain the ability to quickly change temperature with low amounts of energy [14, 55–63]. The prolific exploitation of a thin nanomaterial heater that is of interest to this thesis is the use of CNT thin films in the OoO process [14, 21, 22, 26–28], which is described in detail in Sec. 2.4.

2.3 Accelerated Curing

In aerospace-grade parts, as discussed above for the focus of this work, the polymer being cured as the matrix is typically a thermoset. Thermosetting resins typically used in aerospace-grade composites include polyesters, epoxies, phenolics, and polyimides, bismaleimides, and benzoxazines, each with its own advantages and disadvantages. Epoxies are the most prevalent for aerospace structural applications [64], due to their high specific strength and stiffness, as well as their exceptional corrosion and fatigue resistance [65]. Thermoset resins cure slowly at room temperature, but the application of additional heat causes exothermic reactions to occur that cross-link the polymer.

These cross-linking connections created during the composite curing process cause the thermoset resin reactions to be irreversible [66]. Thermoplastic resins typically used in aerospace-grade composites include polyphenylene sulfide and polyether ether ketone, among many others. In contrast, thermoplastic resins never cure, but rather are "glassy" semi-crystalline or amorphous polymers [67]. At lower temperatures, temporary links take the place of the cross-linking that occurs in thermosetting resins, retaining the shape of the thermoplastic. However, by increasing the temperature above a certain threshold (∼400°C for PEEK [68]), the induced stronger molecular motions override the weaker links, allowing for changes in shape to occur.

Cure kinetics of the various thermoset resins define the cure cycles prescribed to cure the FRP composites. The chemistry of the polymer used in a composite defines the resin viscosity and exothermic reaction speed, and thus, different polymers require different cure cycles. In thermoset composites, prepreg is typically required to be cured starting from B-stage cured resin, where the mixing of the resin and curing agent has occurred and the chemical reaction has started but can be effectively halted by lowering the temperature (typically via freezer storage). From this point in the curing process, the temperature is ramped up to a set value, which maintains a lower viscosity to enable void removal from the composite and also begins the cross-linking process to fully cure the laminate. The hold is maintained during which the gelation of the resin takes place, raising the viscosity of the composite. Finally, the temperature is further increased to raise the Degree of Cure (DoC) to a higher value (90% to 95% is acceptable, per [69]) to increase the mechanical properties of the matrix and solidify the resin. The manufacturer recommended cure cycle for Hexcel 8552 resin, a common aerospace-grade epoxy resin compatible with carbon fiber reinforcement, is shown as an example, with the first temperature hold at 110 °C for 1 hour, and the second temperature hold at 180 °C for 2 hours, as shown in Fig. 2-1. Some systems have only one ramp and one hold, but the cycle below for 8552 resin is more typical.

Areas of interest for optimization reside in the two ramp rates, as well as the isothermal hold times and temperatures at both temperature holds. The varying viscosity profile and gel time at different temperatures of epoxy resin can give way to

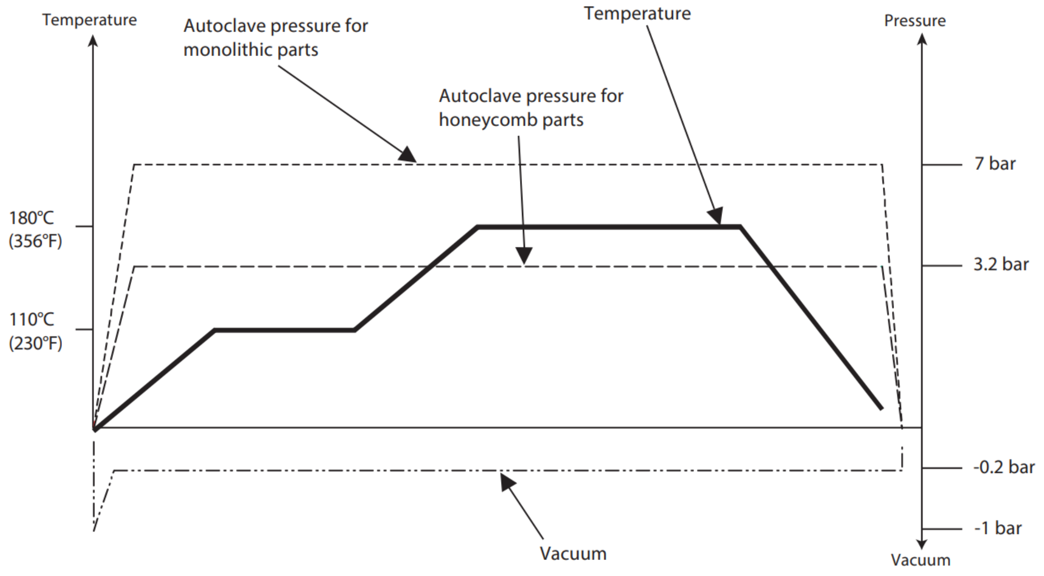

Figure 2-1: Hexcel 8552 resin MRCC. Figure from [70].

further optimization, especially if the heating source is able to provide rapid changes in temperature. These options have been explored in thermoset autoclave [71] and OoA [72, 73] prepreg laminates in previous work. However, these options fail to eliminate voids completely, or require the use of a different resin altogether, which can affect material properties significantly [74].

2.4 Out-of-Oven (OoO) Curing

The process of Out-of-Oven (OoO) curing utilizes carbon nanotube (CNT) heaters placed on the surface of the laminate to create a temperature environment, while the pressure environment is obtained through the VBO manufacturing of the composite. Thermal heating using horizontally-aligned CNT microheaters was introduced for composites several years ago [22, 69]. It was demonstrated that using Joule heating in such CNT sheets, an acceptable Degree of Cure (DoC) is attained, as well as the ability to obtain near 100% energy transfer as opposed to autoclaves, which have significant energy losses (Fig. 2-2).

This first iteration of OoO involved integrating a chemical vapor deposition (CVD) grown CNT film into the structure. Subsequent studies [14, 26, 27] demonstrated how

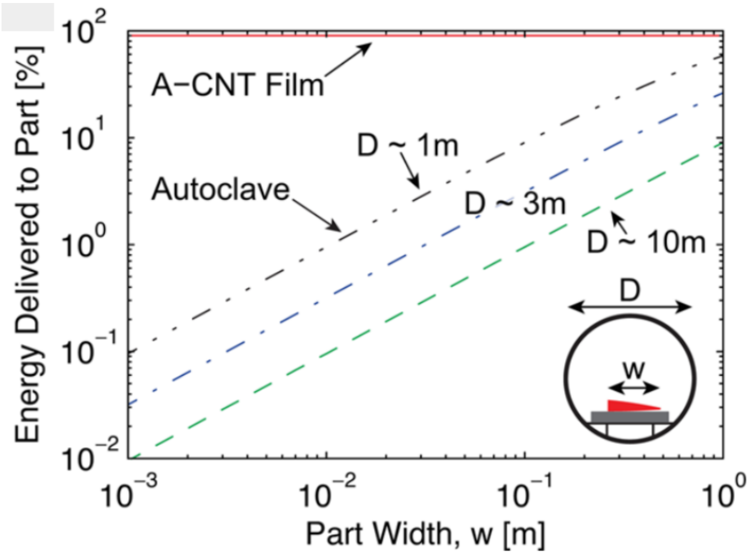

Figure 2-2: Out-of-Oven vs. autoclave energy transfer efficiency by part width. Figure from [69].

OoA prepregs and thermoplastic prepregs can be cured void-free while maintaining mechanical properties. Thermal circuit diagrams comparing OoA and OoO show that OoO has the additional benefit of direct contact with the laminate (Fig. 2-3).

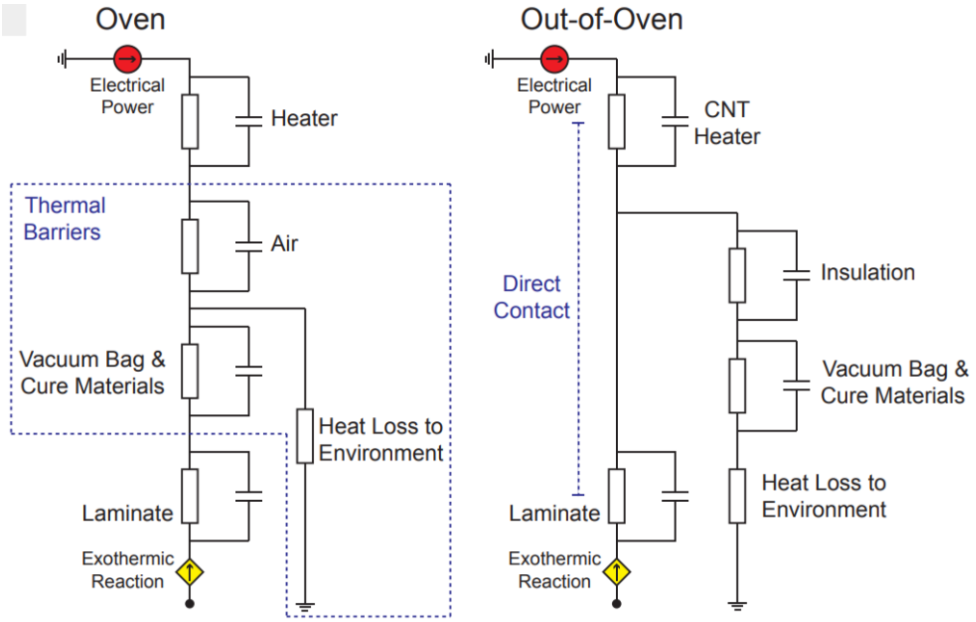

Figure 2-3: Out-of-Autoclave (OoA) vs. Out-of-Oven (OoO) thermal circuit diagrams. Note that the OoO energy transfer efficiency is much higher due to the direct contact between the heating film and the laminate. Figure from [14].

More recent studies explore the ability of OoO with autoclave prepreg [28] with the use of vertically aligned carbon nanotubes (VA-CNTs) as nanoporous networks (NPNs) in the interlaminar region that provide additional capillary pressure to draw resin into the void-prone interlaminar region. It was found that there was no statistically significant difference in terms of void content (both measured at 0 vol% with a voxel size of 650 nm) and short beam shear (SBS) strength between autoclave and OoO processed laminates [28]. Thus, nanoporous networks have become a topic of interest for curing autoclave prepreg FRPs.

Aside from energy savings, the OoO with NPN manufacturing process has the potential for accelerated curing using CNT thin films as the conductive heat source, due to their low thermal mass (areal density of ~25 g/m^2 [27]), direct or nearly-direct contact with the composite laminate (depending on if the CNT heater is integrated into the composite or its separate entity), and their ability to heat up rapidly (12.3 °C/s [19]), allowing for increased throughput. Furthermore, the OoO with NPN system is especially beneficial due to its ability to conform to any part geometry that uses autoclave prepreg. It was mentioned in Sec. 2.1 and Sec. 2.2 that geometric constraints frequently hindered autoclave prepreg manufacturing, among many other manufacturing processes for FRPs. This is not the case for OoO and NPN with autoclave prepreg, as heaters can be adjusted to any composite geometry as needed. A benefit is an additional reduction in the number of parts (Fig. 2-4), which saves time, energy, and is highly efficient while maintaining mechanical properties.

2.5 Nanoporous Networks (NPNs)

Nanoporous networks (NPNs) are material systems that contain nanoscale sized pores. NPNs have been studied extensively [75–79] and have recently been found to wick polymer resin through the nanopores via capillary action, resulting in the apparent "wetting" of the NPN material. Previous work has demonstrated that CNTs, electrospun polymer nanofibers (EPNs), and polyimide (PI) aerogel materials have been successful in removing voids in autoclave carbon fiber reinforced polymer (CFRP)

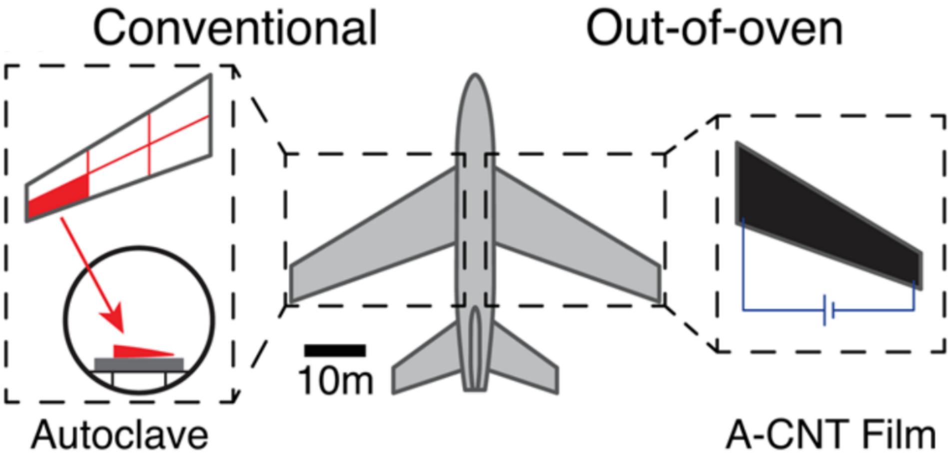

Figure 2-4: Autoclave vs. Out-of-Oven (OoO) part size comparison. OoO is not constrained by geometry, allowing for manufacture of larger, simpler, mechanically equal aircraft and spacecraft parts. Figure from [69].

unidirectional and woven composites [28–30]. Mechanical properties have also been tested for unidirectional prepreg flat panel and L-shaped CFRP laminates, but further data is required for NPN application as a general system. NPNs provide the additional benefit of being tailorable, with properties such as capillary pressure and permeability relying on NPN pore size, porosity, and constituent material [29, 80]. This can prove to be useful when using different resin systems, fiber systems, and prepreg types (unidirectional or woven). NPNs can be conformable to uneven surfaces of autoclave prepreg laminae and can provide capillary pressure that replaces autoclave pressure in the interlaminar region (Fig. 2-5).

2.6 ANSYS Composite Cure Simulation (ACCS)

ANSYS is a commercially available finite element analysis (FEA) software that is used in many fields of engineering and physics. ANSYS Composite Cure Simulation is an add-on to ANSYS Mechanical and can be used in conjunction with Transient Thermal and Static Structural analyses. It is used as a tool for high fidelity analysis of a cure cycle on composite curing. After creating the basis for a composite laminate and fully defining ply orientations and the appropriate shell geometry, the Transient

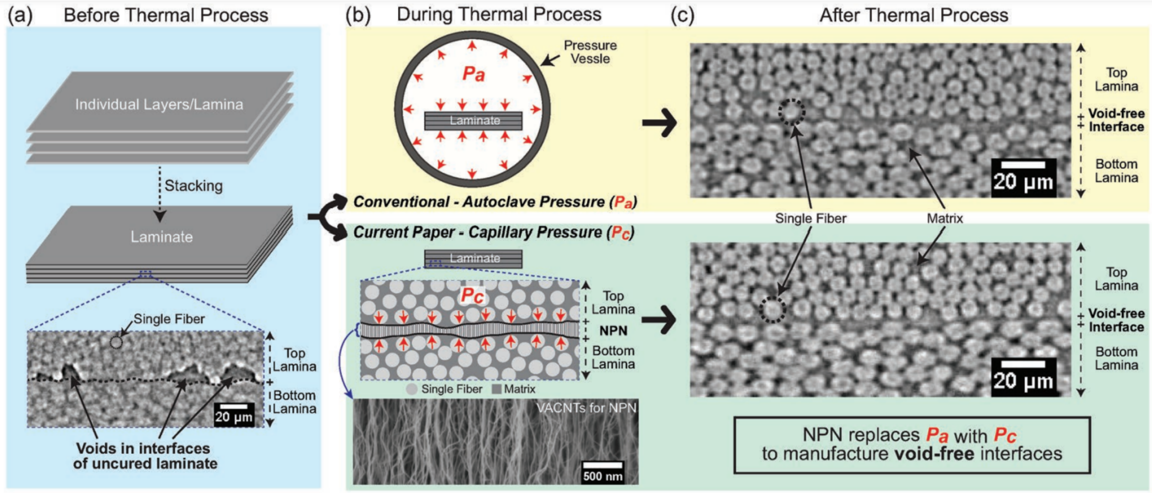

Figure 2-5: Autoclave pressure vs. NPN capillary pressure in interlaminar region during OoO and NPN processing of composite laminates. Figure from [28].

Thermal Analysis finds the DoC and overall temperature distribution at all times during the cure, which can be transferred to a Static Structural analysis for residual stress calculation (Fig. 2-6).

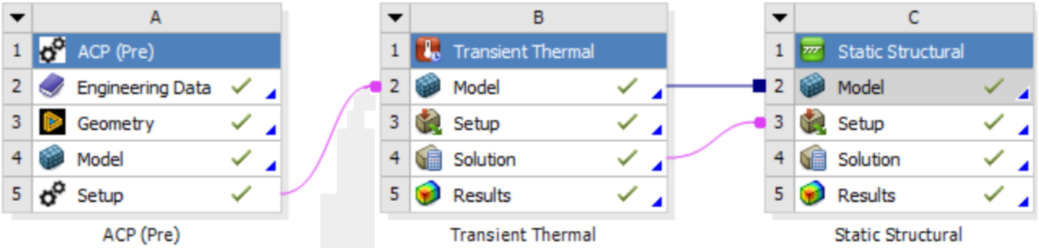

Figure 2-6: Typical work flow for ANSYS Composite Cure Simulation (ACCS) studies. Adapted from [81].

ACCS utilizes extensive material properties obtained from differential scanning calorimetry (DSC) analysis of the resin. These properties are inputted into cure kinetics equations to model key variables such as DoC with Nth Order, Autocatalytic, Kamal Sourur, Avrami-Erofeev, and Karnakas-Partridge equations for $\frac{\partial(DoC)}{\partial t}$; proportional diffusion limitation $difLim$ and parallel diffusion limitation K_D; released heat $\dot{q}$; and glass transition temperature T_g [81]. ACCS models the material in four states: liquid, ungelled glassy, rubbery, and glassy states, and linearly interpolates between them based on temperature, glass transition temperature T_g, DoC, and gelation

DoC [81]. Two methods are offered for solving the finite element model: Transient Solution Method and Fast Solution Method. The transient solution method heavily relies on cure temperature history and is more computationally intensive, while the fast solution assumes that the laminate is thin (<5 mm) and that the temperature distribution is uniform across the laminate. For this thesis, the full transient solution method was employed, to acquire key characteristics such as DoC and temperature and their distribution across the laminate. The characteristics of the composite laminate highly depend on the cure temperature history and cure conditions, and the transient thermal analysis considers the continuous development of material properties with higher fidelity [81]. The ACCS simulation is used in conjunction with additional software and programming to optimize the cure cycle to minimize cycle time while under constraints, principally a target DoC.

2.7 Summary and Conclusions

Traditional and alternative curing methods for fiber-reinforced polymer (FRP) composites have been extensively studied, optimized for, and utilized for aerospace manufacturing processes. Of these processes, Out-of-oven (OoO) curing has been shown to be among the most robust and adaptable. OoO curing in tandem with nanoporous network interlaminar placement has been shown to be a promising manufacturing process for autoclave prepregs. With the use of finite element tools such as ANSYS Composite Cure Simulation, along with well studied optimization algorithms applied to composites manufacturing in the past, an OoO with NPN highly optimized curing manufacturing process for FRP composites can be studied toward throughput, reliability, and adaptability.

Chapter 3

Objectives and Approach

The objectives of this thesis, as well as the approach taken to meet them, are given below and further expanded upon in Chapters 4 and 5, split between the investigation of VBO curing of NPN reinforced FRPs in Chapter 4, and searching for optimized (and accelerated) curing cycles for the OoO process in Chapter 5.

3.1 Objectives

This thesis focuses heavily on the Out-of-Oven (OoO) and nanoporous network (NPN) technologies as described in Chapters 1 and 2 and explored in previous works. The overarching goal is to further develop the OoO with NPN manufacturing processes for autoclave prepreg composite laminates for aerospace industry use. The specific objectives for this thesis follow this overarching goal:

- Demonstrate whether various nanoporous networks (NPNs) have the ability to remove voids in autoclave prepreg composites that are cured under vacuum-bag only (VBO) conditions for various material systems and geometries
- Investigate whether material properties of autoclave prepreg composites cured with NPN interlaminar reinforcement under VBO conditions are mechanically equivalent or superior to composites cured under autoclave temperature and pressure conditions

- Explore whether the OoO with NPN manufacturing technique is viable, can successfully utilize a variety of alternative temperature curing cycles, and can be optimized to reduce cure time
- Investigate whether ANSYS Composite Cure Simulation (ACCS) combined with Python optimization algorithms can be used to search for optimized cure cycles

3.2 Approach

To meet these objectives, a wide search among several material systems and OoO cure cycle possibilities is employed. This is to establish, if possible, the application of both the OoO and NPN techniques to as broad a set of aerospace-relevant autoclave-formulated prepreg types as possible, as well as to ensure an accurate and optimized OoO cure cycle. The approach to meet each of these objectives is the following:

- Conduct VBO curing with either electrospun polymer nanofiber (EPN) or polyimide (PI) aerogel NPN, and use micro-computed tomography (µCT) and scanning electron microscopy (SEM) to measure void content and interlaminar thickness, using woven carbon fiber reinforced polymer (CFRP) composites and PI aerogel in a flat plate configuration as well as unidirectional glass fiber reinforced polymer (GFRP) and PI aerogel in a flat plate, quasi-isotropic configuration, checking for maintained manufacturing quality
- Conduct an MRCC cure cycle, and cure cycles acquired from ANSYS Composite Cure Simulation combined with a python optimization algorithm, for CFRP flat plate composites using the OoO with NPN manufacturing technique, and use µCT to measure void content, as well as differential scanning calorimetry (DSC) to measure degree of cure (DoC), checking for maintained manufacturing quality
- Conduct SBS testing, adhering to ASTM standards, for specimens from each of the OoO cure cycles attempted, as well as dynamic mechanical analysis (DMA), checking for maintained mechanical properties

Chapter 4

Nanoporous Networks for Out-of-Autoclave Curing

Autoclaves carry the advantage of added pressure that can be integral to the removal of voids, both intralaminar and interlaminar, from a composite laminate. The presence of voids in a composite significantly reduces the physical properties of the laminate [82, 83], due in part to reduced fiber-matrix adhesion, resulting in a facilitated path toward mechanical failure. In this chapter, nanoporous networks (NPNs) are employed to replace autoclave pressure in the interlaminar region with capillary pressure provided by the nanoscale-sized pores. NPNs in this work generally take the form of thin membranes on the scale of microns in thickness, which can be applied similarly to a prepreg ply during layup, or most similarly to a veil material in the interlaminar region of plies. Two different material systems are investigated for laminate quality via void content analysis: Hot-plate cured Autoclave Unidirectional-ply GFRP in a quasi-isotropic layup, and Oven-Cured Autoclave Woven-ply CFRP in a unidirectional lay up.

4.1 Hot-plate Cured Autoclave Unidirectional-ply GFRP

Glass fiber reinforced polymers (GFRPs) are a material system of interest to the aerospace industry due to their competitive specific material properties compared to metals [84, 85], as well as their application in technologies where transparency and structural integrity is desired [86]. Similar to CFRPs, GFRP is often provided by manufacturers in a prepreg form, and thus, nanoporous networks (NPNs) can be used to fabricate autoclave GFRP in a vacuum-bag only (VBO) curing environment. Hexcel Hexply 913/30%/UD192/EC9 673517 prepreg was used for this study, an epoxy e-glass uni-directional prepreg with thermoset polymer resin. This GFRP has applications in aircraft structures in the aerospace industry [87]. More information about the GFRP prepreg can be found in Table 4.1.

Table 4.1: Properties of Hexcel Hexply 913/30%/UD192/EC9 673517 prepreg [88].

913/30%/UD192/EC9 673517 Property	**Property Value or Characteristic**
Fiber	EC9 673517 E-glass unidirectional
Fiber content by volume	~53.3 vol%
Nominal fiber density	2.56 g/cm^3 (0.0925 lbs/in^3)
Resin matrix	913 thermoset polymer
Resin content by weight	30 wt%
Nominal resin density	1.23 g/cm^3 (0.0444 lbs/in^3)
Reinforcement reference	UD192
Glass transition temperature T_g, dry	125°C (257°F)
Gel time at 125°C (257°F)	11.5 min
Cured ply thickness	0.144 mm (0.00567 in)

4.1.1 Sample Preparation

Various methods were used to obtain each of the NPNs. 20 µm tall vertically-aligned carbon nanotubes (VA-CNTs) were fabricated via the chemical vapor deposition (CVD) process, following the processes established in previous work [89, 90]. Two variations of commercial electrospun polymer nanofiber (EPN) polyamide veils by Revolution Fibers were also studied as NPNs, here defined as Type 1 EPN and Type 2 EPN. These EPNs are bespoke commercial films, with the latter being sometimes known as XLB [91], and the former being an earlier version. Last, polyimide (PI) bespoke aerogel films used were obtained from Aerogel Technologies LLC. with a manufacturer-stated porosity of 94 vol%, and varying thickness that is adjusted during the manufacturing process. Thus, four NPNs are considered in this section: (i) VA-CNTs, and 3 polymers (ii) EPN1, (iii) EPN2, and (iv) aerogel. The EPNs are integrated similarly to each other, but the aerogel and VA-CNT NPNs are integrated to the composite plies using significantly different techniques.

20 µm tall VA-CNTs were transferred to the prepreg by first placing the CNTs grown on a catalyzed silicon wafer (via CVD) with the CNT surface face down onto the laminate. Subsequently, a roller was used on the back side of the silicon wafer to apply pressure to transfer the CNTs to the tacky GFRP prepreg surface, and then the silicon wafer was removed, leaving the CNTs on the laminate surface, with at least 95% of CNTs transferred by area (as in [92]). It is important to note that the VA-CNTs do not buckle from this transfer method, per previous work [90]. EPNs were placed directly onto the surface of the GFRP laminate, rolling them onto the prepreg surface with a roller and with the backing paper still attached, and finally removing the backing paper. In order to add a layer of PI aerogel, the following process for deposition of the aerogel layer onto the GFRP prepreg was used:

1. Remove one side of backing paper from the GFRP prepreg

2. Place the exposed side of the prepreg onto an aerogel sheet

3. Use a roller to adhere the aerogel to the GFRP ply

4. Cut a region around the ply (roughly 0.5-1 mm oversized) to detach the aerogel section from the surrounding aerogel sheet

5. Place the GFRP with aerogel onto a hot plate set to 60°C with guaranteed non-porous Teflon (GNPT) on the surface and use a roller to conform the aerogel to the GFRP ply surface, with the aerogel face down, for 10-15 seconds (this step temporarily lowers the resin viscosity, allowing for proper conformation of the NPN to the surface of the laminate via the increase in tackiness)

6. Remove the GFRP with aerogel ply from the hot plate and add the ply with NPN to the overall layup

The aforementioned processes were used in order to create $[0/90/+45/-45]_S$ quasi-isotropic GFRP laminates with NPN. Next, a peel ply was applied to both the top and bottom surfaces of the laminate. Fully stacked laminates were surrounded by 25.4 mm (1 in.) wide and 3.175 mm (0.125 in.) thick cork tape (Batson Cork Tape-.125) along the edges, stacked in enough layers to exceed the thickness of the laminate. Two 25.4 mm (1 in.) x 25.4 mm (1 in.) aluminum plates, each with a 1 mm thickness, were stacked and wrapped in guaranteed non-porous Teflon (GNPT) (Airtech Release Ease 234 TFNP) film to provide sufficient thickness as a caul plate. The caul plate was placed on top of an oversized GNPT film that was in contact with both the laminate and the cork tape. Each cure was then surrounded by vacuum breather material (Northern Composites BR-NB3010) and sealed with a vacuum bag (Airtech Wrightlon 8400). Each cure was done individually and in the same region on the hot plate to avoid potential variance in temperature across the area of the hot plate. A 3-hour debulking step was conducted prior to curing at room temperature and a vacuum pressure measured at 28.5 inHg, and the same vacuum level was maintained throughout the curing step. The temperature profile of the MRCC was followed with 3°C/min ramp rates for both heating and cooling (see Fig. 4-1), and all laminates underwent vacuum-bag only (VBO) curing. A schematic of the stack-up for each laminate is given in Fig. 4-2.

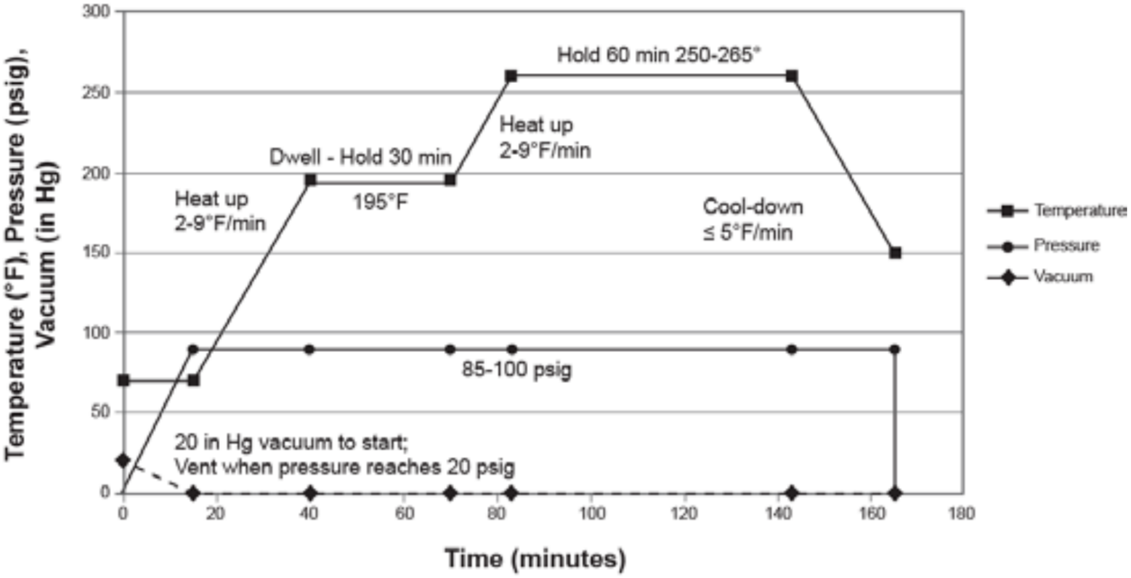

Figure 4-1: MRCC for 913 resin. 3°C/min (5.4°F/min) ramp rates were used for heating and a 2°C/min (3.6°F/min) ramp rate for cooling were used in all laminates manufactured in the GFRP study. The cure cycle was conducted after a 3-hour debulk at room temperature. Figure from [87]. Note units in figure are in °F.

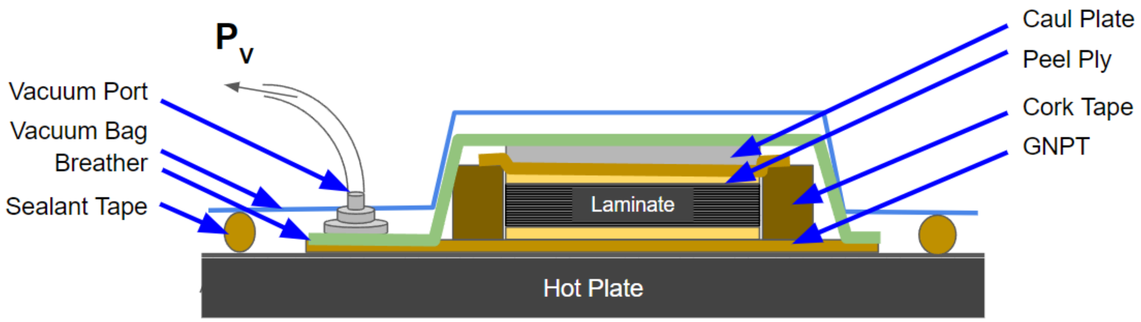

Figure 4-2: Hot plate cure stack-up for GFRP 25.4 mm (1 in.) x 25.4 mm (1 in.) laminate curing.

After completing the cure cycle, the laminates were examined to identify differences in interlaminar thickness via Scanning electron microscopy (SEM). SEM was conducted (Zeiss Sigma 300 VP) with an in-lens secondary electrons detector and a beam voltage of 0.5 kV at a working distance of approximately 4.5-4.7 mm. SEM specimens were prepared by cutting the cured laminate in half with a table bandsaw (MicroLux Variable Speed Mini Band Saw), followed by the polishing of the exposed surface. Automatic grinding was conducted (STRUERS TEGRAPOL 21) with P400, P1200, and P4000 grit silicon carbide sandpaper (approximate particle size of 35, 15, and 9 µm), and automatic polishing was done (Buehler AutoMet 250) with 1 µm diamond and 0.05 µm alumina suspension. SEM was used to investigate across the laminate length along the polished cross section surface. Interlaminar thickness measurements were taken via measurement of the pixel length of the interlaminar thickness and then converted to microns using the pixel size of the SEM images.

In order to measure the void content of the cured laminates, X-ray Micro-Computed Tomography (µCT) was used to image each sample through the length and thickness. The scans were obtained using a Zeiss Versa 620 µCT, which uses the Scout-and-Scan™ Control System software to image 3201 projections of the sample's cross section as it rotates 360°. The scans were obtained with a field of view of approximately 1.5 mm x 1.5 mm and a voxel size of approximately 0.75 µm, resulting in a resolution of approximately 2 µm. In µCT imaging, lighter colors correspond to denser materials, and as such, fibers and resin are significantly brighter than voids, which appear dark grey or black. At times, the voids can have the same brightness as the resin, but in those cases, a ring of darker shading around the edges of the voids is present. It is important to note that given the resolution, µCT can identify macro and micro-sized voids [93, 94], but is unable to image nanoscale voids due to the resolution size. Although not explored in this work, the SEM is known to be able to provide information on nanoscale-sized voids if deemed necessary. All GFRP scans were taken at 80 kV, 10 W of power, and a 5 second exposure time. The source was used with an LE2 filter, and the detector was set to a 4X objective.

Voids were quantified using Fiji ImageJ software [95], using a thresholding method to separate void particle area from the area of fibers and resin. Particles with 50 µm^2 area or higher were counted to avoid interference from image noise after thresholding, corresponding to a void diameter of ∼8 µm, slightly less than the threshold in [96] of 10 µm in diameter. Void content was analyzed from 21 cross-section slices from each of the µCT scans at an equidistant spacing from each other among the ∼2000 total slices. The percent of area that is from voids for each of the slices is used to calculate the average and standard error of the specimen void content.

4.1.2 NPN Selection

A study to compare the four NPN options was conducted to compare the performance of each NPN for the for GFRP unidirectional prepreg material system. For this study, two key selection criteria were utilized. First, it is essential to minimize the final thickness of the NPN in cured laminates. This minimizes the effects of the NPN on the nominal material properties of the composite. Second, removing all voids as a first screening step for subsequent mechanical testing. Overall, the objective is to minimize changes in material properties, geometry, and accessibility.

To test the various NPNs, a 25.4 mm (1 in.) x 25.4 mm (1 in.) $[0/90/+45/-45]_S$ GFRP laminate with a different NPN for each interlaminar region was laid up by hand. A schematic detailing the laminate layers is shown in Fig. 4-3. The aerogels were the first NPNs to be applied using the technique outlined in Sec. 4.1.1, for each of the 4 aerogel layers. The 2 types of EPN and the VA-CNTs were subsequently transferred. Specimens for SEM were prepared as described in Sec. 4.1.1. Images collected via SEM are shown in Fig. 4-4, Fig. 4-5, and Fig. 4-6. There appear to be intralaminar voids in the ply adjacent to the Type 1 EPN NPN, while the rest of the laminate is void-free in the cross section being imaged, although this is an isolated case, as the rest of the ply was void-free in the cross section being imaged. Thus, as a first analysis, all four NPNs seemed to work to remove most voids.

Thickness is a factor taken into consideration, as the additional thickness in the interlaminar region is desired to be minimized to reduce the effect of the interply material on the overall material properties of the system. An increase in composite

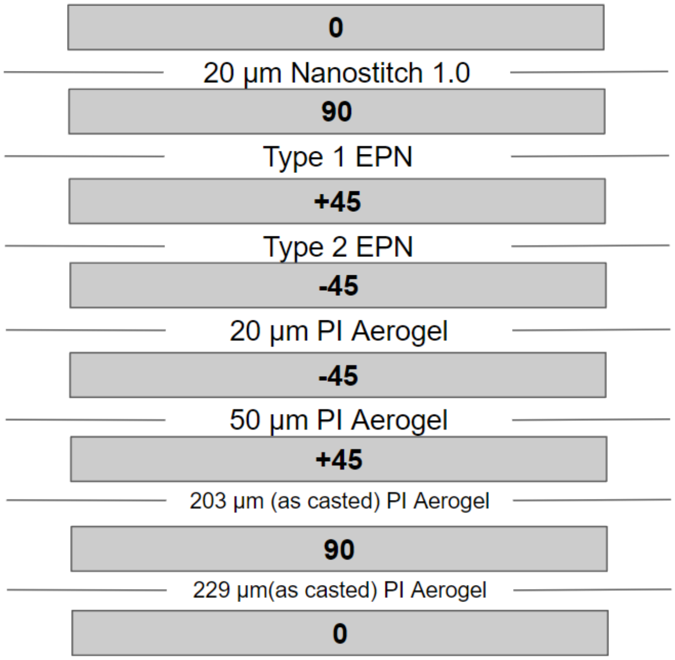

Figure 4-3: Material orientation of GFRP plies, along with NPNs used in interlaminar regions in the preliminary study to select the best NPN options. VA-CNTs, two layers of EPNs of different polymers, and four PI aerogel layers were used as NPNs in the interlaminar region. As casted thicknesses are expected to be roughly double the final aerogel film thickness after shrinkage from manufacturing of the aerogel.

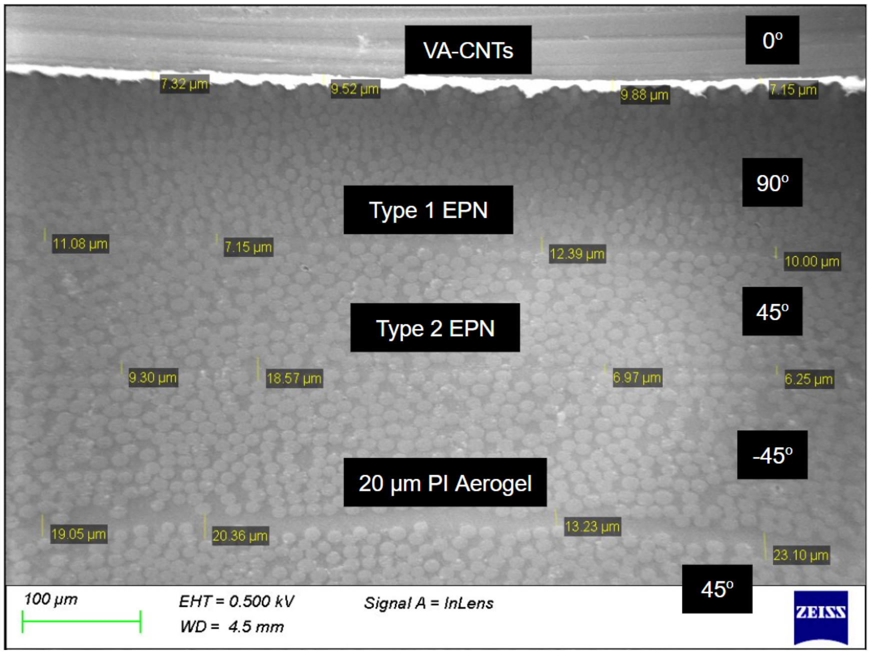

Figure 4-4: Top 5 plies and 4 interlaminar regions of GFRP laminate with various NPNs, along with measurements of interlaminar thickness taken in microns. Note that the CNTs are significantly brighter due to electron charging.

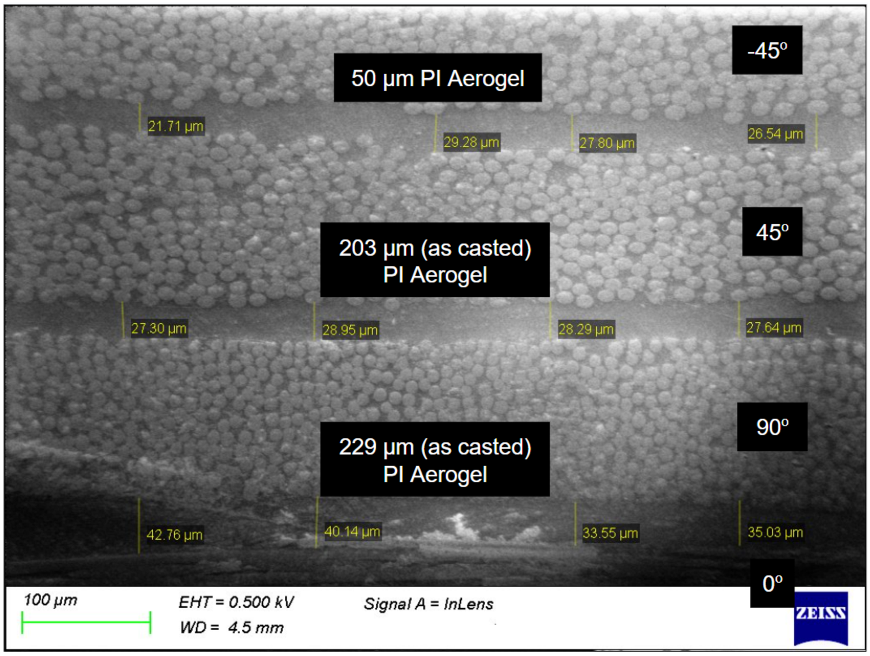

Figure 4-5: Bottom 4 plies and 3 interlaminar regions of GFRP laminate with various NPNs, along with measurements of interlaminar thickness taken in microns.

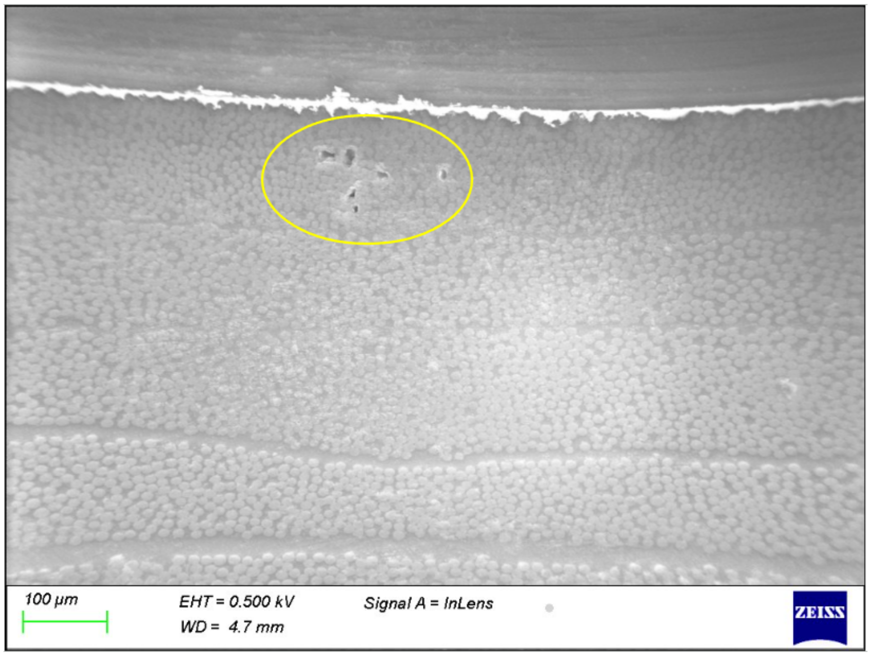

Figure 4-6: Intralaminar voids identified (yellow oval) adjacent to Type 1 EPN and VA-CNT interlaminar regions.

thickness indicates that there is an increase in the nominal amount of resin in the interlaminar region. Removing additional resin from the adjacent plies may lead to the degradation of the mechanical properties of the laminate, and thus, it is important to minimize the thickness of the NPN. The resulting interlaminar thicknesses for each of the NPNs tested are shown in Table 4.2. The 20 µm VA-CNTs, Type 1 EPN, Type 2 EPN, and 20 µm PI aerogel are preferred to the 50 µm, 203 µm (as casted), and 229 µm (as casted) PI aerogels in terms of thickness, while remaining generally equivalent in void content (except the isolated case aforementioned).

Table 4.2: Measured post-cure thickness of interlaminar regions with NPN present. ± are standard error, with 4 samples taken per interlaminar region. 229 µm PI aerogel thicknesses are believed to be an overestimate, as a slight distortion of the image is observed due to the use of the InLens detector.

NPN Material	**Average Thickness of Interlaminar Region (± Standard Error) [μm]**
VA-CNTs	8.47 ± 0.71
Type 1 EPN	10.16 ± 2.23
Type 2 EPN	10.27 ± 5.68
20 µm PI aerogel	16.44 ± 6.45
50 µm PI aerogel	26.33 ± 3.28
203 µm (as casted) PI aerogel	28.05 ± 0.73
229 µm (as casted) PI aerogel	37.82 ± 4.38

µCT was taken in order to check the void content across the width of the specimen. A representative cross section is shown in Fig. 4-7. From the µCT scan cross sections, there are no voids across the width of the laminate within the cross section area, adding Type 1 EPN and VA-CNTs back into the pool of options. In terms of manufacturing and scalability and accessiblity, the EPNs and aerogels were readily available at the time of conducting experiments, so the VA-CNTs were not investigated, although using VA-CNTs (the first reported NPN [28]) could be a potential avenue for future work. Type 1 EPN is easier to handle than Type 2 EPN (which is more fragile and tears easily), and thus, Type 2 EPN was eliminated as an option. As a result of the thickness measurements, void content analysis, availability, and manufacturing considerations, Type 1 EPN and the 20 µm PI aerogel were selected as the NPNs in the subsequent analyses.

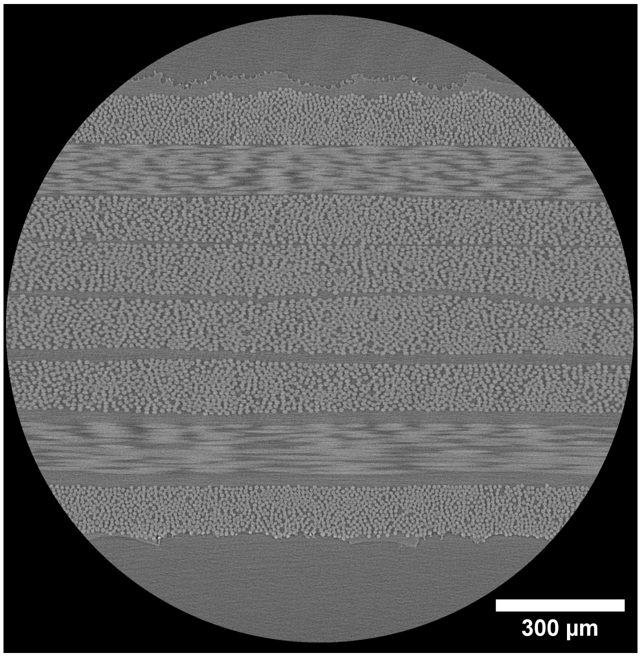

Figure 4-7: Representative µCT cross section of GFRP laminate with various NPNs showing no voids. NPNs from top to bottom: 20 µm VA-CNTs, Type 1 EPN, Type 2 EPN, 20 µm PI aerogel, 50 µm PI aerogel, 203 µm (as casted) PI aerogel, 229 µm (as casted) PI aerogel.

4.1.3 Quality of Manufactured Laminates

After the NPNs were selected, a total of three 25.4 mm (1 in.) x 25.4 mm (1 in.) GFRP $[0/90/+45/-45]_S$ laminates were manufactured, each using VBO pressure and oven convective heating: GFRP with no NPN, GFRP with 20 µm PI aerogel as the NPN, and GFRP with Type 1 EPN as the NPN. Baseline laminates cured in an autoclave in other work [88] show the expected results of no voids, and this was not repeated here. For the thin aerogel laminate, aerogel layers were placed in all 7 interlaminar regions, and for the Type 1 EPN laminate, EPN was placed in all 7 interlaminar regions. Each of the aerogel and Type 1 EPN NPNs were deposited or placed as previously described and the MRCC was followed in the VBO cures (see Sec. 4.1.1).

The sample quality is measured via µCT and SEM as with the preliminary study. µCT was taken to examine the laminate's void content with a field of view of an approximately 1.5 x 1.5 mm cross section (length and width, respectively) across the thickness of the specimen, while SEM images were taken to examine thickness and qualitative sample quality.

SEM

SEM imaging was taken of the 20 µm PI aerogel and Type 1 EPN NPNs within the 8 ply GFRP quasi-isotropic laminates. Thickness measurements were taken and are shown in the SEM images in Fig. 4-8 and Fig. 4-9. The average thickness with standard error for Type 1 EPN interlaminar regions within GFRP was 6.67 ± 0.75 µm, and for 20 µm PI aerogel, it was 12.63 ± 0.82 µm, resulting in the Type 1 NPN having a statistically significant advantage over the 20 µm PI aerogel in terms of thickness. However, the SEM of the Type 1 NPN specimen showed intralaminar voids, which become more prevalent in the µCT scans.

µCT

µCT was conducted across the VBO (no NPN), EPN, and PI aerogel laminates, to investigate the effects of each NPN on the laminate quality. Pixel size was ∼0.75 µm for each of the three scans, allowing for a resolution of objects of ∼2 µm. A representative cross section of the VBO (no NPN) (Fig. 4-10), EPN (Fig. 4-11), and PI aerogel (Fig. 4-12) is shown. Thresholding yielded the results shown in Table 4.3 for void content among the three samples scanned. Particles with 50 μm^2 area or higher were counted to avoid interference from image noise after thresholding, corresponding to a void diameter of ∼8 µm.

The VBO (no NPN) GFRP laminate showed the typical behavior of an autoclave prepreg laminate being cured without adequate pressure [97], with both interlaminar and intralaminar voids, and an overall unacceptable void content above 1 vol%

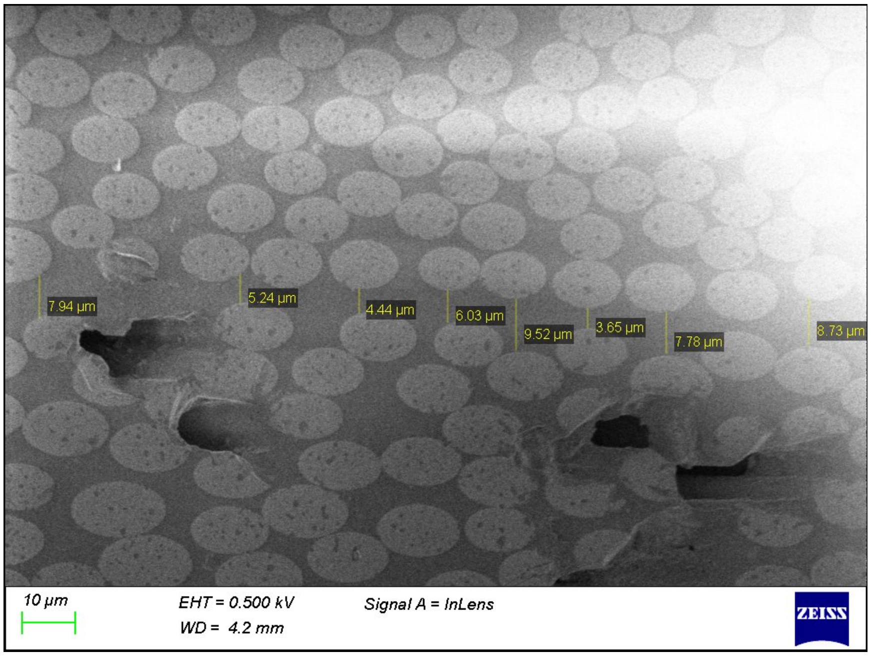

Figure 4-8: SEM thickness measurements of a representative interlaminar region of GFRP with Type 1 EPN as the NPN. Bright spots are due to electron charging. Dark spots are either intralaminar voids in the GFRP ply or artifacts of the surface preparation.

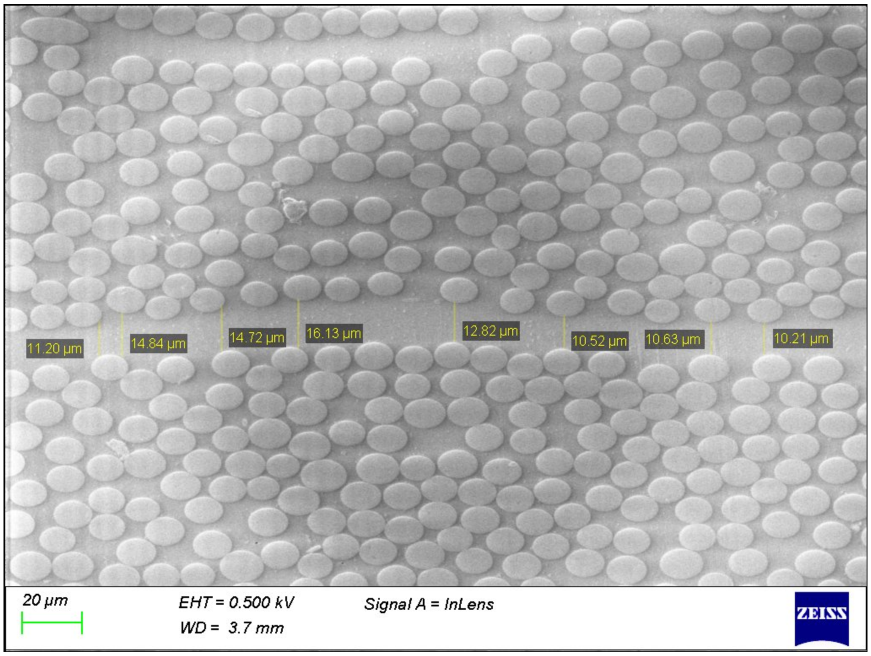

Figure 4-9: SEM thickness measurements of a representative interlaminar region of GFRP with 20 µm PI aerogel as the NPN. Bright spots are due to electron charging.

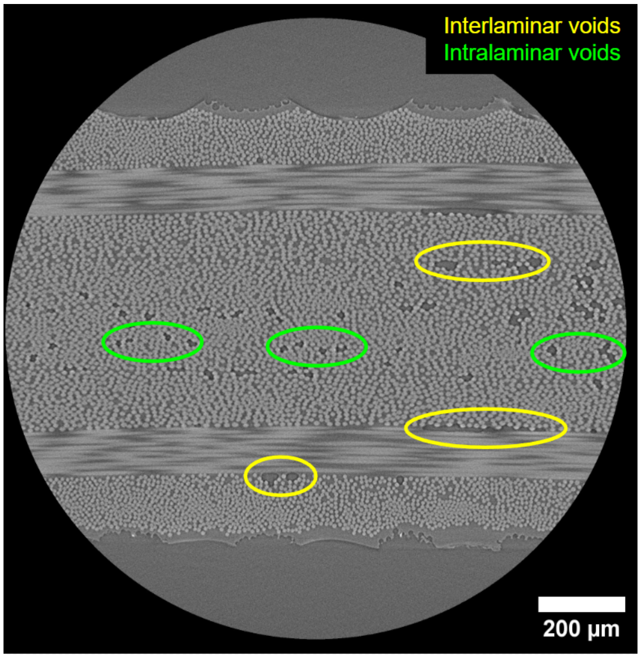

Figure 4-10: Representative µCT image of 1" x 1" hot plate VBO cured quasi-isotropic 8 ply GFRP laminate with no NPN. Both intralaminar and interlaminar voids are present.

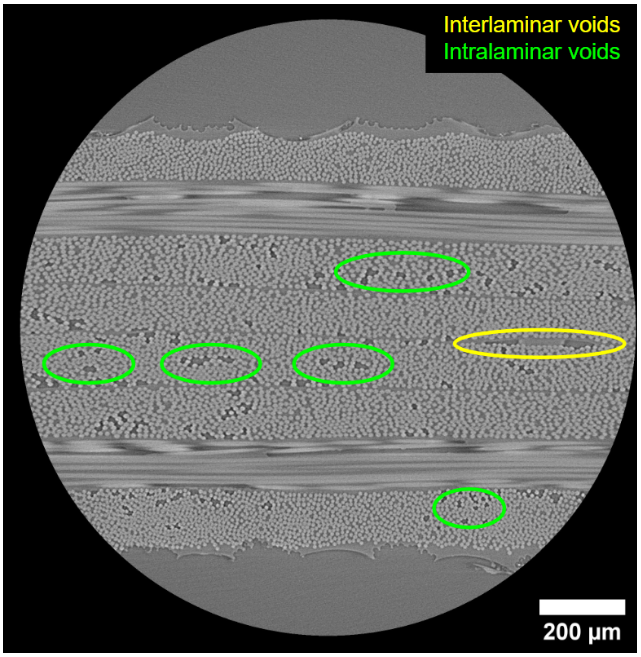

Figure 4-11: Representative µCT image of 1" x 1" hot plate VBO cured quasi-isotropic 8 ply GFRP laminate with Type 1 EPN. Intralaminar voids were found and isolated cases of interlaminar voids were observed.

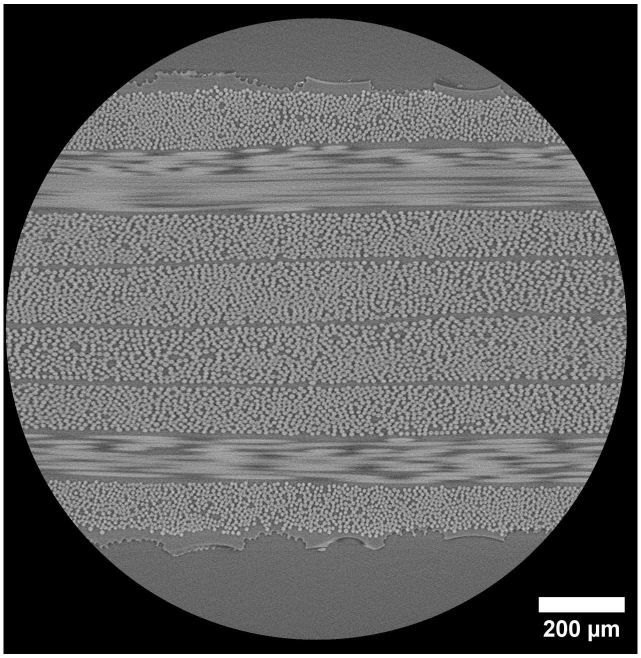

Figure 4-12: Representative µCT image of 1" x 1" hot plate VBO cured quasi-isotropic 8 ply GFRP laminate with 20 µm PI aerogel. The laminate is void-free with a resolution of ∼2 µm (pixel size of 0.74 µm).

Table 4.3: Measured void content of the VBO (no NPN), Type 1 EPN, and 20 µm PI aerogel GFRP laminates, using the thresholding method.

NPN Material	**Void Content (± Standard Error) [vol %]**
VBO (No NPN)	1.29 ± 0.08
Type 1 EPN	2.03 ± 0.13
20 µm PI aerogel	0.00 ± 0.00

(aerospace standard per [83]) was observed. The Type 1 EPN was shown to have a statistically significant increase in void content from the VBO (no NPN) laminate. However, a minimal amount of void content is from interlaminar voids, and there is an increased prevalence of intralaminar voids. The 20 µm PI aerogel does not suffer from a similar result, but instead, successfully evacuates all voids from the GFRP laminate.

An interesting effect of the aerogel is also observed when comparing the µCT images of the VBO (no NPN) and aerogel GFRP laminates. The VBO laminate without NPN shows a high presence of intralaminar voids, pointing to another laminate region where external (such as autoclave) pressure is needed. However, interestingly, the GFRP with PI aerogel in the interply also rid the laminate of the intralaminar voids, an effect analogous to autoclave pressure.

Although the PI aerogel was found to cause a doubling of the interlaminar thickness compared to the Type 1 EPN, the 20 µm PI aerogel is the best alternative of all NPNs in this study, due to its ability to remove voids from autoclave GFRP in a VBO cure, as well as its thin thickness relative to the other NPNs. Furthermore, a thinner version, once aerogels are adapted to come in thinner sheets, may produce a similar void-removal result. Further investigation is required on both the effect of a thinner aerogel layer, as well as the effects of the VBO and aerogel modifications on the mechanical properties of GFRP laminates cured to the MRCC or an altered cure cycle.

4.2 Oven-Cured Autoclave Woven-ply CFRP

In previous work [29], woven autoclave CFRP laminates with NPN cured outside of the autoclave have been shown to produce void-free laminates using a 60 µm thick PI aerogel. The prepreg used in that study had nominal viscosity. Subsequent trials were done to repeat the initial finding with prepreg from a new roll of identical material, but were initially unsuccessful, as the resin of the new roll appeared to have higher viscosity (not quantified here) compared to the old roll, potentially due to handling issues. This section outlines adjustments in processing made to significantly reduce void content in the manufacturing of woven CFRP laminates with prepregs of a lower quality, while also reducing the thickness of the NPN used, from an estimated 60 µm (measured 69 µm) to an estimated 50 µm (measured 40 µm). More information about the CFRP woven prepreg used for this study (Hexcel IM7/8552 6K SPG 196-PW) can be found in Table 4.4.

Table 4.4: Properties of Hexcel IM7/8552 6K SPG 196-PW woven prepreg [70].

Material Property of Hexcel IM7/8552 6K SPG 196-PW Woven Prepreg	**Property Value or Characteristic**
Fiber	IM7 6K, carbon fiber, woven
Nominal fiber content by volume	55.57 vol%
Nominal fiber density	1.56 g/cm^3 (0.056 lbs/in^3)
Resin matrix	8552 thermoset polymer
Resin content by weight	37 wt%
Nominal resin density	1.301 g/cm^3 (0.0470 lbs/in^3)
Reinforcement reference	SPG 196-PW
Glass transition temperature T_g, dry	200°C (392°F)
Gel time at 177°C (350°F)	13 min
Cured ply thickness	0.199 mm (0.0078 in)

4.2.1 NPN Selection

The aerogel films were obtained from Aerogel Technologies LLC., with a manufacturer-stated porosity of 94 vol%. Aerogel has several benefits that favor effective resin wicking into the interlaminar region. The ability to control the thickness of the PI aerogel layer allows for the control of how much resin is brought into the interlaminar region and can allow for more or less conformity to the rough woven prepreg surfaces. Compared to unidirectional laminates (Sec. 4.1), the interlaminar regions of woven-prepreg laminates are both thicker and have a larger range. Additionally, compared to other NPNs tested, PI aerogel has been shown to have the ability to obtain porosity and permeability characteristics [29] that are favorable for resin infiltration of the interlaminar region. Favorable characteristics include a porosity that results in a capillary pressure that is on par with the autoclave [80] and can provide a higher driving force for resin flow into the interlaminar region, and a permeability that is sufficiently high to allow for the resin to wet the NPN effectively. As seen with the GFRP (Sec. 4.1), the permeability and capillary pressure of PI aerogel are sufficient for manufacturing void-free laminates of that material. An SEM of the porous structure of the aerogel is shown in Fig. 4-13.

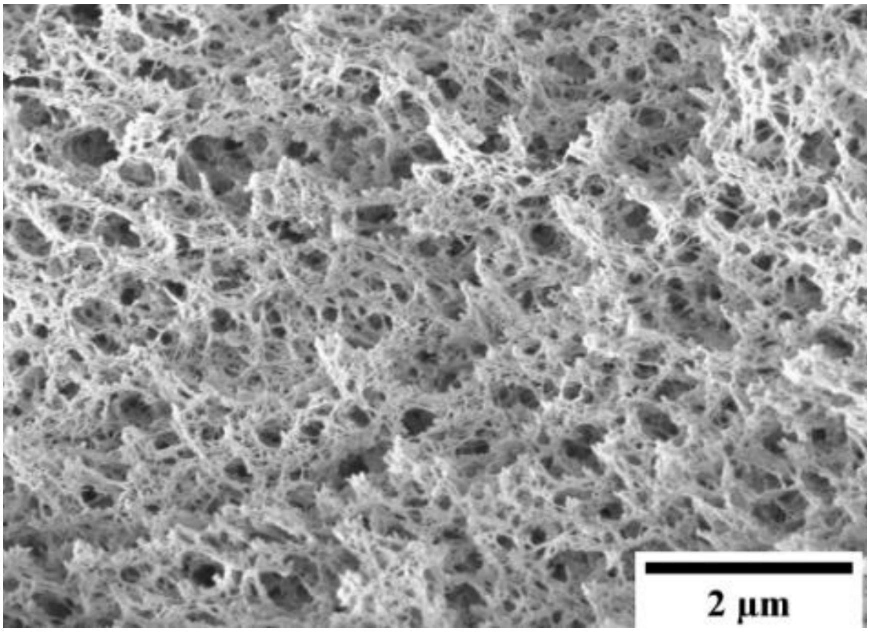

Figure 4-13: Representative SEM image of PI aerogel. Figure from [29].

By increasing the thickness of the PI aerogel layer, the NPN is allowed to conform to the regions that are most difficult to reach and ensures resin infusion in those regions via capillary pressure. A thickness of 60 µm has been found to keep the benefits of the ability to conform to the rough woven prepreg surface and induce resin infusion in void-prone regions without also causing intralaminar voids in previous work [29]. In this study, the NPN was manufactured to result in a final film thickness of 50 µm. However, although the thickness is generally uniform for the PI aerogel films, the final thickness has a wider spread. To find the thickness of the NPN used, µCT imaging of the aerogel film was conducted. The scans were obtained with a field of view of approximately 0.7 mm x 0.7 mm and a voxel size of approximately 0.36 µm, resulting in a resolution of approximately 1 µm. The scan was taken at 100 kV, 14 W of power, and a 7 second exposure time. The source was used with no filter (air), and the detector was set to a 20X objective. The µCT scan is shown in Fig. 4-14, with the interlaminar thickness estimates as ∼40 µm.

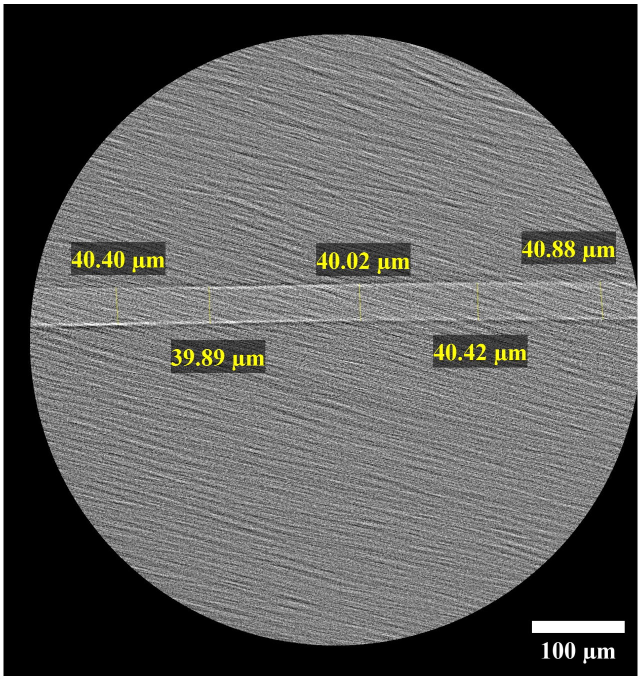

Figure 4-14: Measured thickness of an estimated 50 µm PI aerogel film. The thickness is approximately 40 µm.

4.2.2 Sample Preparation

As with the GFRP study, a similar process for placing of the PI aerogel NPNs was utilized and was as follows:

1. Remove one side of backing paper from the precut CFRP woven prepreg
2. Place the exposed side of the prepreg onto an aerogel sheet
3. Use a roller to adhere the aerogel to the CFRP woven ply

4. Cut a region around the ply (roughly 0.5-1 mm oversized) to detach the aerogel section from the aerogel sheet
5. Place the CFRP woven ply with aerogel onto a hot plate set to 60°C with GNPT on the surface, using a roller to conform the aerogel to the CFRP woven ply surface, with the aerogel in contact with the GNPT, for 15-20 seconds
6. Remove the CFRP woven ply with aerogel from the hot plate and add the ply with NPN to the overall layup

The hot plate rolling step, as discussed in Sec. 4.1, may induce resin flow that allows for proper conformation of the NPN to the surface of the laminate via the increase in tackiness. One key difference between this sample preparation and that of the GFRP is the time spent rolling the ply with NPN system on the hot plate. As the CFRP woven viscosity is lower at 60°C compared to the GFRP, more time was available to adhere the aerogel to the laminate. After 15 seconds, the GFRP ply begins to deform very easily under minor rolling pressure, so the rolling time was significantly more limited in the GFRP case. Here, however, the aim was to roll for no more time than necessary to adhere the aerogel to the NPN layer.

A major difference to be noted between this study and the previous initial study is the thickness of the aerogel layer. The thickness of the previous study was reported to be approximately 69 µm [29]. However, in this study, µCT measurements of the PI aerogel layer showed an approximate thickness of 40 µm (of the estimated ∼50 µm PI aerogel NPN). In both cases, the uniformity of the thickness was not measured, but by eye seemed relatively uniform.

After completing each 25.4 mm (1 in.) x 25.4 mm (1 in.) woven CFRP with NPN layup, a peel ply was applied to both the top and bottom surfaces of both laminates for a smooth surface finish and effective resin wicking. Fully stacked laminates were surrounded by 25.4 mm (1 in.) wide and 3.175 mm (0.125 in.) thick cork tape (Batson Cork Tape- .125) along the edges, stacked in enough layers to exceed the thickness of the laminate. Two 25.4 mm (1 in.) x 25.4 mm (1 in.) aluminum plates, each with a 1 mm thickness, were stacked and wrapped in guaranteed non-porous Teflon (GNPT)

(Airtech Release Ease 234 TFNP) film to provide sufficient thickness as a caul plate. A caul plate was placed on top of each oversized GNPT film. Each GNPT film is in contact with both the laminate and the cork tape. Each cure was then surrounded by vacuum breather material (Northern Composites BR-NB3010) and sealed with a vacuum bag (Airtech Wrightlon 8400). Laminates cured in pairs shared a cork tape edge, which did not produce significant changes in the laminate quality. Vacuum was pulled with a diaphragm pump (MD1C) and measured to be 28.5 inHg.

The first implemented change from the previous study was to cure the laminates in the oven. Cures were done simultaneously in pairs of two on the same base plate in the oven (Thermo Scientific™ Heratherm™ Advanced Protocol Oven 51028126H), where convective curing keeps a consistent temperature profile among the two laminates. The second implemented change from the previous study was to conduct the 3-hour debulking step at 60°C. This lowers the viscosity of the prepreg slightly, allowing for proper consolidation of the laminate, as well as additional conforming of the NPN to the surfaces of the prepreg prior to the final cure cycle. Debulking steps are common in out-of-autoclave (OoA) processing of OoA prepreg. After the debulking step, the vacuum-bag only (VBO) cures were conducted with the manufacturer recommended cure cycle (MRCC) temperature profile for 8552 resin (Fig. 4-15), with a 3°C/min ramp rate for heating, and a 5°C/min ramp rate for cooling. A schematic of the stack-up is shown in Fig. 4-16.

4.2.3 Quality of Manufactured Laminates

µCT was used to check the void content of a laminate made with the old roll and the new roll, as well as cured interlaminar thicknesses. The scans were obtained using a Zeiss Versa 620 µCT, which uses the Scout-and-Scan™ Control System software to image 3201 projections of the sample's cross section as it rotates 360°. The scans were obtained with a field of view of approximately 3.27 mm x 3.27 mm and a voxel size of approximately 1.61 µm, resulting in a resolution of approximately 5 µm. Old and new prepreg laminates were placed in the µCT together to scan both at once. 80 kV and 10 W were used, with an exposure time of 2 seconds, the LE2 filter applied to

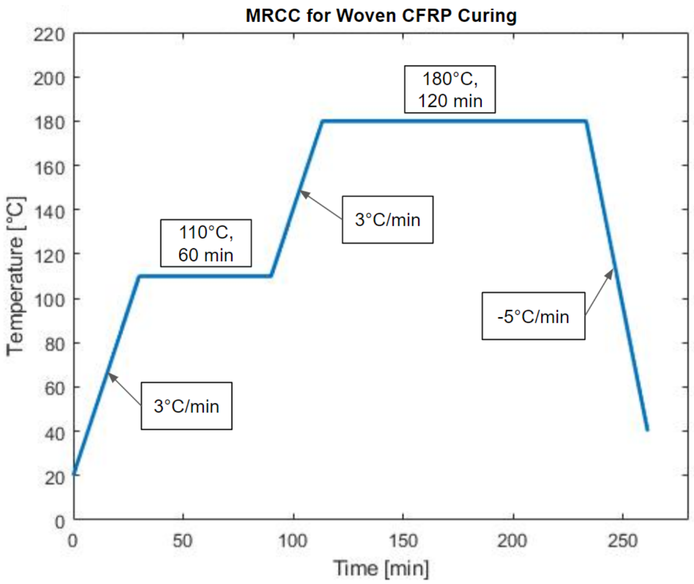

Figure 4-15: MRCC used in curing woven CFRP laminates after a 3-hour debulk at 60°C.

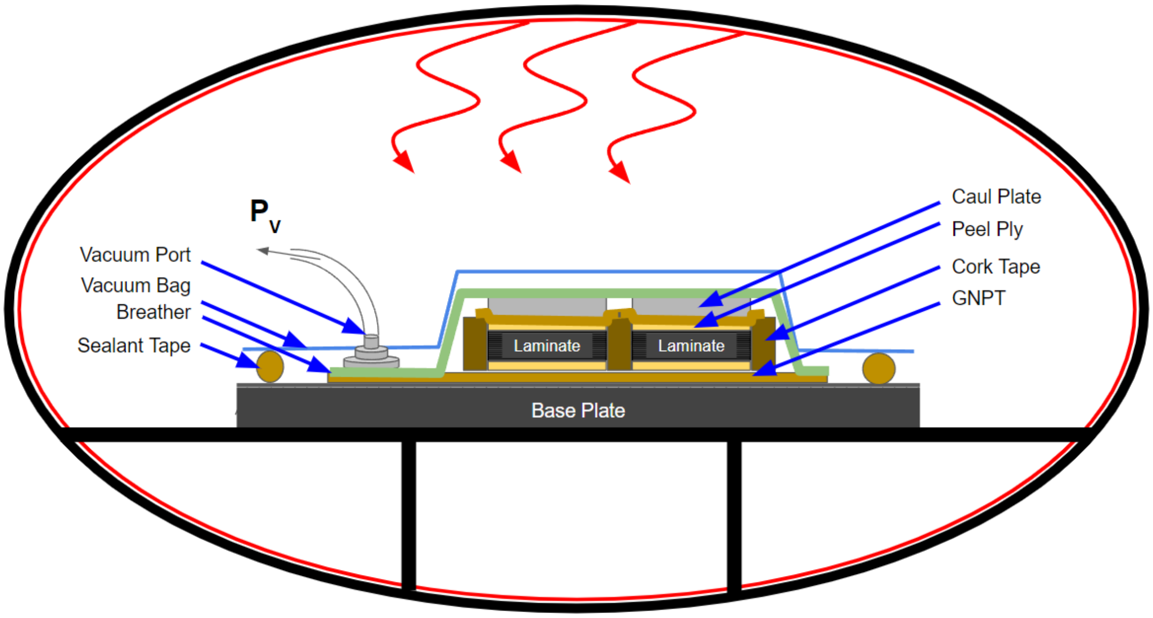

Figure 4-16: Schematic of curing set-up for two simultaneous laminate woven CFRP cures in an oven.

the source, and the detector was set to a 4X objective. A representative µCT image is shown in Fig. 4-17. Thresholding yielded the results shown in Table 4.5 for void content among the two samples scanned from 19 cross sections. Particles with 30 µm^2 area or higher were counted to avoid interference from image noise after thresholding, corresponding to a void diameter of ∼6 µm. Note that this threshold is different than that of the GFRP due to improvements in image contrast.

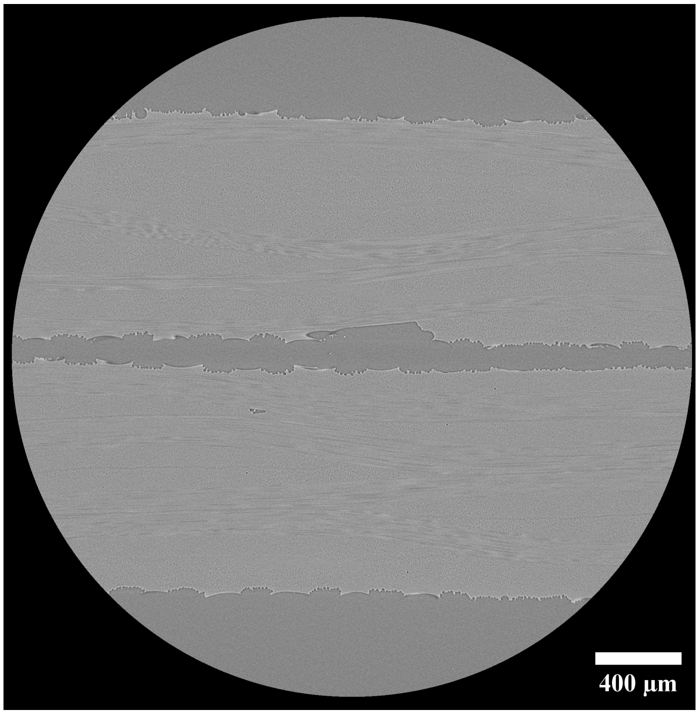

Figure 4-17: Representative cross section of old and new IM7/8552 prepreg manufactured laminates. The top laminate was made with the old IM7/8552 woven prepreg, and the bottom laminate was made with the new IM7/8552 prepreg. There are limited voids present in both laminates.

Table 4.5: Measured void content of the old and new prepreg versions of the IM7/8552 8 ply woven laminate with 50 µm PI aerogel, using the thresholding method.

NPN Material	**Void Content (± Standard Error) [vol%]**
Old IM7/8552 woven	0.021 ± 0.006
New IM7/8552 woven	0.016 ± 0.003

The void content in both laminates is significantly lower than the 1 vol% guideline common in the aerospace industry, boding well for maintaining structural properties. Further investigation is needed for the mechanical properties of the IM7/8552 woven with PI aerogel (via VBO curing), but they are expected to be comparable to the mechanical properties of autoclave baseline laminates, based on the minimal void content.

4.3 Conclusions

In this chapter, two composite laminate material systems were investigated for VBO and NPN curing: unidirectional GFRP and woven CFRP. It was found in both cases that PI aerogel thin films can be an effective replacement of autoclave pressure in the interlaminar region, providing an alternate means for void evacuation in glass and carbon fiber composites. With the unidirectional GFRP material, PI aerogel was able to successfully create a void-free laminate, evacuating both intralaminar and interlaminar voids. VA-CNTs and both EPNs also showed promise as well, but due to secondary considerations were de-prioritized relative to the PI aerogel. With the woven CFRP material, thinner thicknesses of PI aerogel NPN films were found to enable the manufacturing of high quality woven CFRP laminates. The mechanical properties of unidirectional GFRP and woven CFRP manufactured with the VBO and NPN framework are of interest and should be checked for maintained material properties in the future.

Chapter 5

Optimization of Out-of-Oven Curing Cycle

The Out-of-Oven (OoO) manufacturing technique is a powerful tool to significantly reduce cost in the manufacturing of fiber reinforced polymer (FRP) composites. The ability to cure autoclave-grade prepreg laminates without the loss of quality makes the transition to OoO curing in the aerospace industry significantly faster. OoO also allows for manufacturing of larger parts, as the geometric constraint is a non-factor. Cost savings are abundant in the reduction of power requirements, quick procurement and set-up of the OoO system, and the loss of the need for large autoclaves as well as transportation of parts to and from autoclave facilities. OoO is also able to achieve accelerated cure cycles, due to the ability of the conductive heating carbon nanotube (CNT) thin sheet to quickly elevate temperature with adequate power. Using PID control, the cure cycle can be very closely followed [98], allowing for ANSYS Composite Cure Simulation (ACCS) predictions to provide key insights into improving the OoO process.

ACCS can be used to create optimized curing cycles by providing time, temperature, and Degree of Cure (DoC) estimates. The cure cycle optimization problem is one of many minimization problems, where the objective is to find the optimal solution of output values based on an objective function (or functions) that is calculated based on some number of input values. These input values are modified and tested until convergence is found on the globally optimal values for each input. Optimization problems are present in fields such as engineering [99], energy [100], and machine learning [101], among many others. In the field of FRP matrix composites, optimization has been attempted in several areas, including the winding [102, 103], draping [104], and forming [105, 106] of the fiber reinforcement, the prepreg filling stage [107, 108], and the curing stage [109–112], using both single and multi-objective algorithms to achieve improvements in time, quality, throughput, and simplicity.

Generally, minimization optimization problems can be described in the following framework:

$$\mathbf{x} = \begin{bmatrix} x_1 & x_2 & ... \end{bmatrix} \tag{5.1}$$

$$\text{Minimize } \mathbf{G}(\mathbf{x}) = \begin{bmatrix} f(\mathbf{x}) & h(\mathbf{x}) & ... \end{bmatrix} \tag{5.2}$$

$$\text{Subject to constraints } C_1 \leq f(\mathbf{x}) \leq C_2,\ x_1 > C_3, ... \tag{5.3}$$

where $\mathbf{x}$ is the vector of design variables, $\mathbf{G}(\mathbf{x})$ is the vector of objective functions, and $f(\mathbf{x})$ is a single objective function to be optimized for. Note that the constraints listed are examples, and C_1, C_2, and C_3 can be functions of any vector, constant, or objective function as well. In this framework, all input variables in $\mathbf{x}$ are iterated over via an algorithm to find the best set of objective function values in $\mathbf{G}(\mathbf{x})$.

Python has many publicly available libraries and algorithms that are suitable to solve a plethora of minimization optimization problems, including SciPy [113], Pyomo [114], and genetic algorithms [115]. The choice of algorithm depends on the nature of the problem characteristics, such as constraints, number of input variables, number of objective functions, knowledge of the gradient, and other factors [116].

After utilizing a Python optimization algorithm to acquire the ideal accelerated cure cycle, experimental testing was done to test the optimal curing cycle in 152.4 mm (6 in.) x 152.4 mm (6 in.) quasi-isotropic AS4/8552 flat plate composite laminates with electrospun polymer nanofiber (EPN) nanoporous networks (NPNs) in the interlaminar region.

5.1 Optimization of ACCS Model

An ANSYS Composite Cure Simulation (ACCS) model was created in order to model the curing of a carbon fiber reinforced polymer with varying techniques, cure cycles, and configurations. Specifically, Hexcel's Hexply AS4/8552 [70] and its readily available material properties were used to model the traditional autoclave convective curing and OoO conductive curing manufacturing processes. The model was then optimized for optimal cure cycle time and for an ideal laminate degree of cure (DoC). An optimization algorithm from the SciPy Python library [113, 117] was utilized in this work, for reasons outlined in Sec. 5.1.3.

5.1.1 Optimization Approach

The approach taken to optimize the cure cycle can be summarized into 7 key steps, all of which are listed below.

1. **Initialize model geometry in SpaceClaim.** Creating the surface area dimensions for the composite laminate to be cured (thickness depends on number of plies and thickness per ply, which is developed in ACP Pre, a later step), as well as creating the volumetric dimensions for the 1 mm thick aluminum caul plates, the 3.175 mm thick aluminum base plate, and 25 mm thick insulation blocks for the thermal environment.

2. **Create composite laminate in ANSYS Composite PrepPost (ACP Pre).** The material for each of the plies, the layup orientations, and ply thickness are set in this module of ANSYS Workbench.

3. **Put geometry together in ANSYS Mechanical, establish connections, mesh, etc.** This mainly involved establishing part orientation in space, setting parameters for thermal conduction between parts, and meshing.

4. **Establish the Transient Thermal Analysis Environment.** This involved setting the cure cycle of the system, including setting ramp rates and temper-

ature holds that the composite is subjected to, as well as defining the mode of heat transfer for composite curing.

5. **Create the base function that fully defines temperature conditions, runs the analysis, and extracts Time and Degree of Cure Data in ANSYS Mechanical.** This function was made to draw the bridge between the optimization and running of the solver in ANSYS Mechanical (inputs → outputs).

6. **Create parameters to optimize the curing cycle.** Parameters were selected and available for optimization based on experimental attempts at creating an optimized cure cycle [118], as well as prior knowledge of cure kinetics. Further simplifications in defining the cure cycle were made to simplify the optimization process.

7. **Choose and utilize Python optimization algorithm that takes in the input parameters and runs the optimization using the base function, and returns a cost function that is minimized.** Using Python and the Scripting module in ANSYS Mechanical, an optimization algorithm was implemented after a study on the varying algorithms available for use. Inputs that define the cure cycle are updated into a function that uses ANSYS scripting commands to update the model, run the analysis, and use outputs from the model to calculate an objective function that is minimized by the algorithm.

5.1.2 Model

The ANSYS model tree consists of two different curing mechanisms. A convective model was generated in order to demonstrate curing by traditional convective methods (autoclave, oven), using the manufacturer recommended curing cycle (MRCC). Along with the MRCC convective cure, MRCC conductive cure, an extended first hold conductive cure (done in experimental work, see Sec. 5.2), two Python optimization algorithm generated accelerated conductive cures, and a conductive cure with resin flow considerations were modeled. The tree is shown in Fig. 5-1.

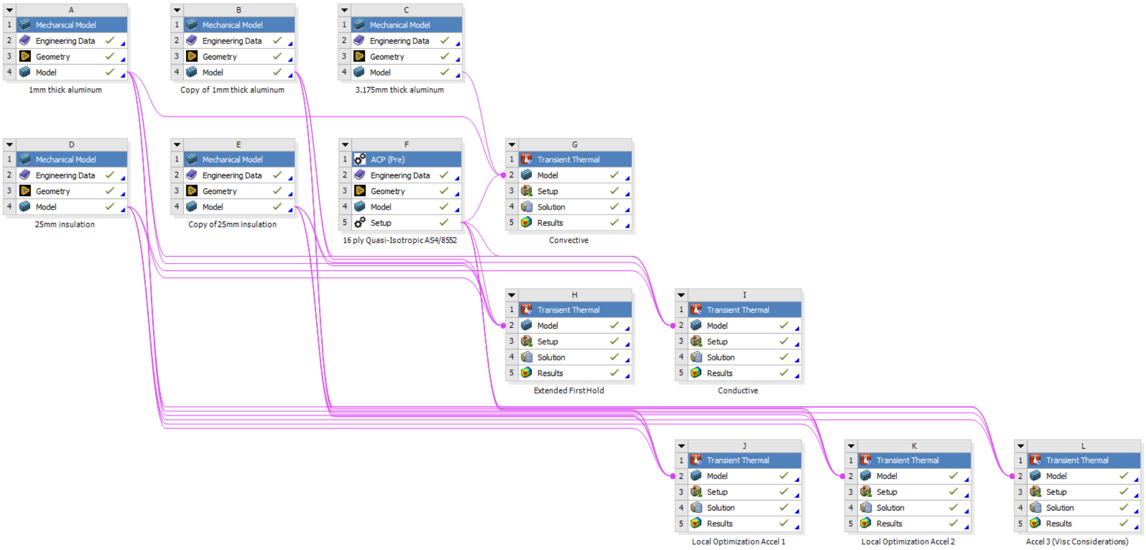

Figure 5-1: ANSYS Workbench model tree, including MRCC convective and conductive cures, an extended first hold conductive cure, two Python optimization generated conductive cures, and a conductive cure with resin flow considerations.

First, material properties for AL-6061-T6, the insulation blocks, and carbon fiber reinforced polymer were implemented. The ANSYS available AL-6061-T6 and ACCS available AS4/8552 material properties were used, as both have an abundance of material property data available. This allows for ACCS to operate correctly, as cure kinetics play a crucial role in the final DoC of the laminate. The insulation blocks were modeled after the commercially available Super Firetemp® X material, an insulating material that is inorganic, non-combustible, and primarily lime, silica, and reinforcing fibers [119]. At the range of temperatures of the cure cycle, the thermal conductivity is sufficiently low for Super Firetemp® X to insulate the laminate well. Important thermal material properties summarize the thermal conductivity of the OoO system in Table 5.1.

The model geometry was initialized using SpaceClaim, an ANSYS module for computer-assisted drafting (CAD). The required geometries were the 1 mm thick aluminum plate, 3.175 mm (0.125 in.) thick aluminum plate, 25 mm thick insulation, and the shell geometry for the composite laminate itself. All geometries were set to a 152.4 mm (6 in.) x 457.2 mm (18 in.) length and width, respectively, as this allows

Material	**Thermal Conductivity, k $\left[\frac{\mathbf{W}}{\mathbf{m\text{-}^\circ C}}\right]$**	**Specific Heat, Const. Pressure, $\mathbf{C_p}\left[\frac{\mathbf{J}}{\mathbf{kg\text{-}^\circ C}}\right]$**	**Density, $\boldsymbol{\rho}\left[\frac{\mathbf{kg}}{\mathbf{m^3}}\right]$**
AL-6061-T6	∼170	∼980	2713
Super Firetemp®X (calcium silicate)	0.101	800*	641
AS4/8552	0.489 (Out-of-Plane)	1300	1580

Table 5.1: Model thermal properties of key materials used in the OoO manufacturing process. Note that approximate values are taken as a rough average over the expected temperature range of OoO curing for 8552 resin laminates (20-200°C). The material properties for AS4/8552 provided by ANSYS are assumed to be constant through the cure. *Specific heat of the Super Firetemp® X was assumed based on similar materials [120].

for the eventual addition of a three-zone heater model study, with each heater being 152.4 mm (6 in.) x 152.4 mm (6 in.) in dimension. The convective set-up traditionally involves surrounding the composite with aluminum caul and base plates of thicknesses 1 mm and 3.175 mm, respectively. The conductive set-up involved surrounding the composite symmetrically, first with 1 mm thick aluminum tool plates, followed by exterior 25 mm thick calcium silicate insulating blocks. Meshing for each of these components was done independently, and left to the program to calculate, due to the simple geometry, as well as the lack of interest in the temperature time history of these components. Resulting geometries and meshes are shown for the 1 mm aluminum plate (Fig. 5-2), 3 mm aluminum plate (Fig. 5-3), and 25 mm calcium silicate block (Fig. 5-4).

The AS4/8552 quasi-isotropic flat plate was created by first initializing the shell geometry in SpaceClaim, which involved creating a shell of dimensions 152.4 mm (6 in.) x 457.2 mm (18 in.). In ANSYS Composite Pre (ACPre), an ANSYS module for initializing a composite material, a $[0/90/+45/-45]_{2s}$ prepreg laminae layup was created, resulting in the geometry in Fig. 5-5. The nominal cured ply thickness was set

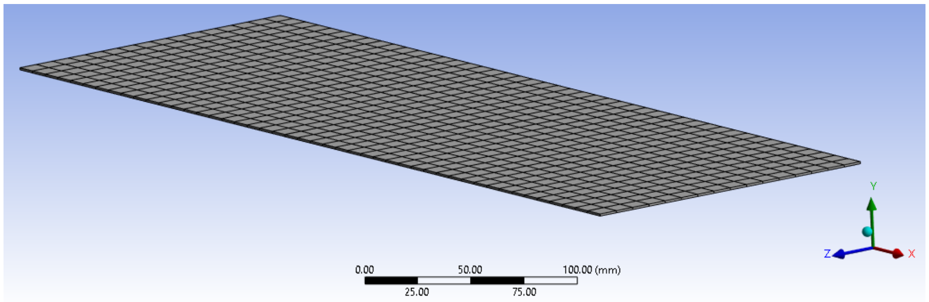

Figure 5-2: 152.4 mm (6 in.) x 457.2 mm (18 in.) by 1 mm aluminum tool plate, used in both convective and conductive cure models.

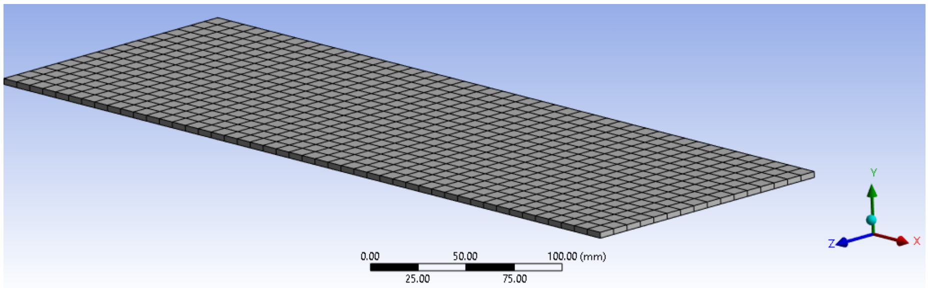

Figure 5-3: 152.4 mm (6 in.) x 457.2 mm (18 in.) by 3.175 mm ($\frac{1}{8}$") aluminum tool plate, used in the convective cure model.

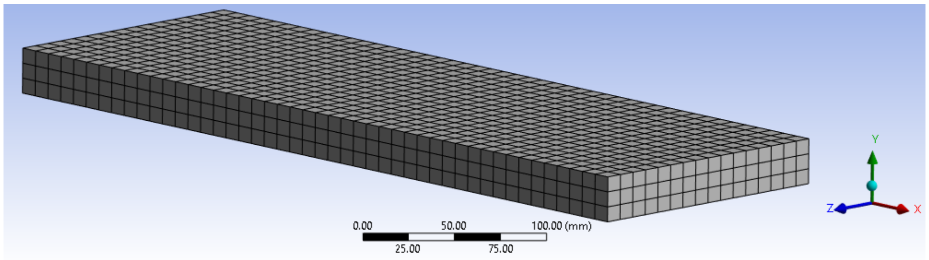

Figure 5-4: 152.4 mm (6 in.) x 457.2 mm (18 in.) by 25 mm Super Firetemp® X (calcium silicate) insulating block, used in the conductive cure model.

to 0.130 mm, resulting in a geometry that is 2.08 mm thick. Material property data for AS4/8552 was supplied by the ANSYS ACCS program material library, which obtained its data from an external composite spring-in study [121].

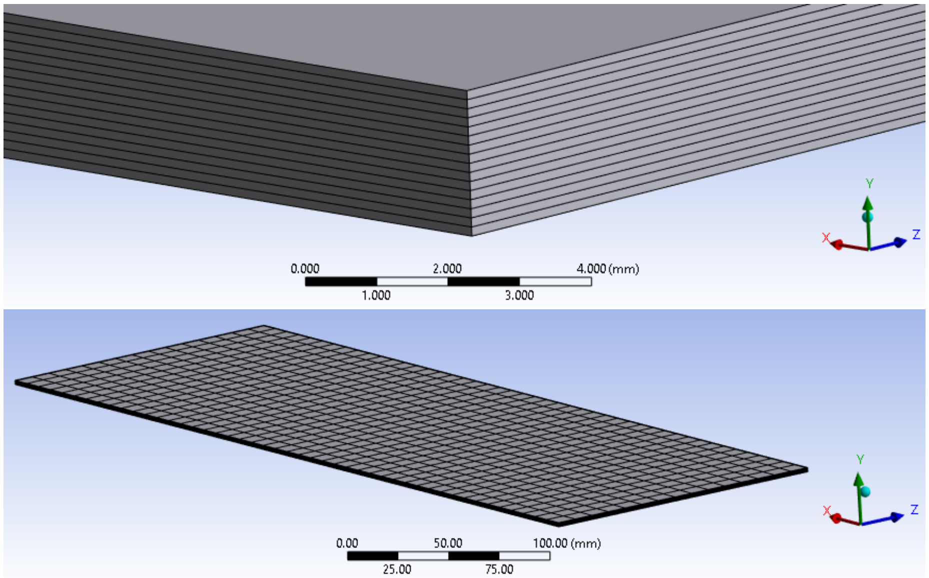

Figure 5-5: 152.4 mm (6 in.) x 457.2 mm (18 in.) by 2.08 mm $[0\ 90 + 45 - 45]_{2s}$ 16 ply AS4/8552 quasi-isotropic flat laminate for ACCS.

After geometries were initialized, the ANSYS Mechanical models were built. Each of the parts was imported into the model and properly transformed to correctly depict the setting. The setting for convective and conductive heating Transient Thermal analyses in ANSYS Mechanical is depicted in Fig. 5-6 and Fig. 5-7, respectively.

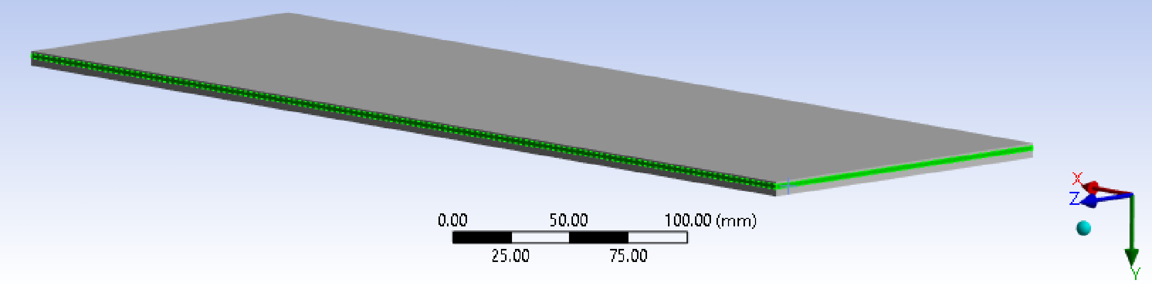

Figure 5-6: Geometry set-up for the convective model. Aluminum is in gray, and AS4/8552 is in green. Note that the thicker base plate is touching the bottom face of the composite in this depiction.

An important note to make is that because the layup is symmetrical, and gravity does not play a factor in the Transient Thermal analysis, the coordinate system is

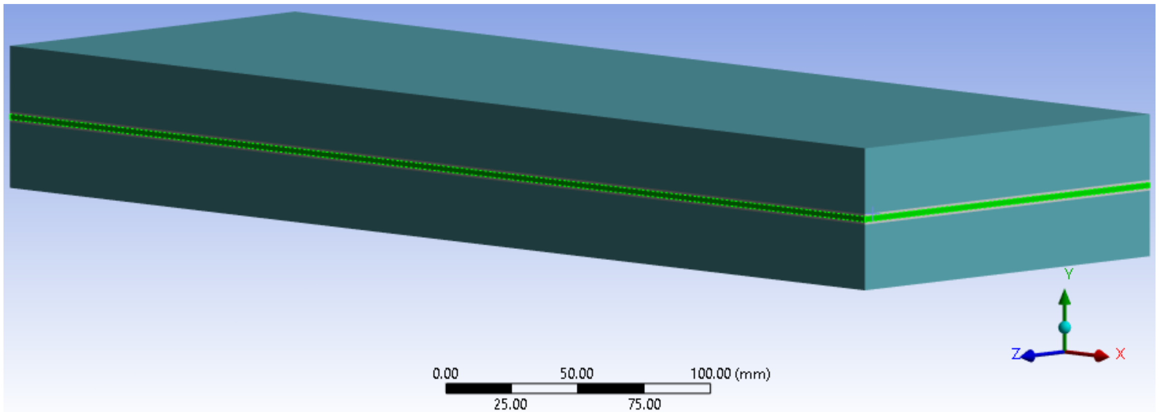

Figure 5-7: Geometry set-up for conductive models. The insulation is in teal, aluminum in gray, and AS4/8552 in green.

only dependent on the y-direction pointing in the out-of-plane direction for the model. The x-direction corresponds to the 0° fiber direction in all cases, and the z-direction corresponds to the 90° fiber direction in all cases. For all models, it was assumed all other materials typically involved in curing (peel ply, guaranteed non-porous Teflon (GNPT) film, breather, vacuum bag, cork tape, sealant tape, CNT heater) did not significantly alter the thermal characteristics of the systems. Furthermore, thermal contact conductance values between components were allowed for the program to control, except for connections involving the composite, where it was assumed to have a high thermal contact conductance between the composite laminate and aluminum plates ($10^6 \frac{W}{m^2\text{-}°C}$), following previous work [118]. The initial temperature of the ambient environment was set to 22°C for all models.

For the convective MRCC cure model, a convection load was applied to the two surfaces facing the external environment on the top and bottom of the stack-up. The convective temperature load was set to the MRCC, and it was assumed that the stack-up was subjected to forced convection by heated dry air. As such, the convection coefficient was set to 15 $\frac{W}{m^2\text{-}°C}$ (from [118], supported by [122]). The cure cycle used for the model is specified in Fig. 5-8 and applied as shown in Fig. 5-9.

The average DoC across the laminate is 91.80% according to the ACCS simulation, fitting into the 90-95% cured range deemed acceptable by the aerospace industry. The distribution of the DoC is uniform across the laminate, as expected from a convective

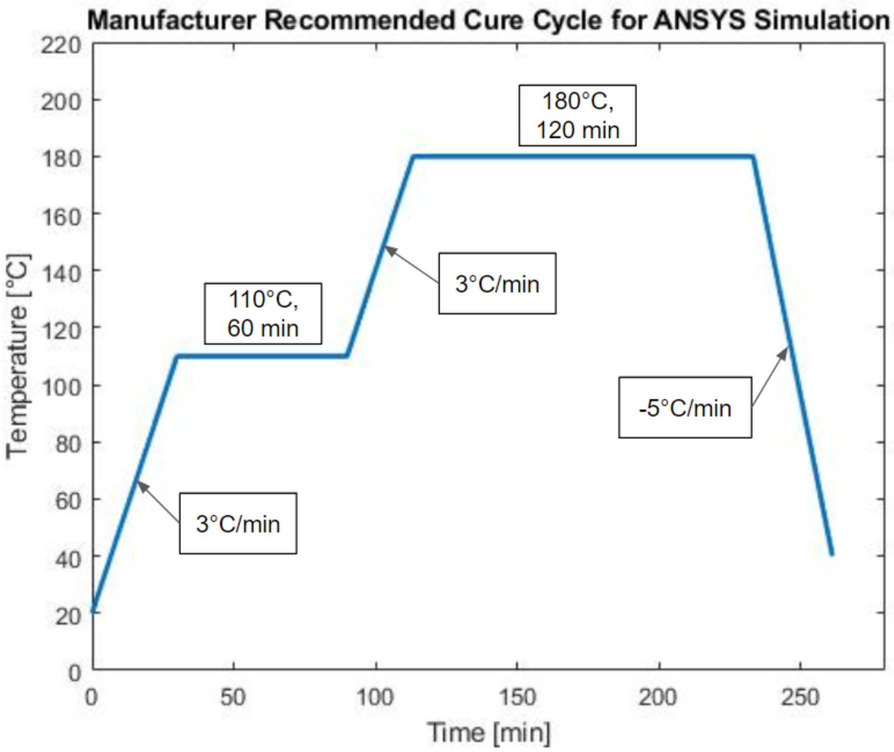

Figure 5-8: MRCC for ANSYS model convective and conductive curing. 3°C/min ramp up rates and a -5°C/min ramp down rate were used.

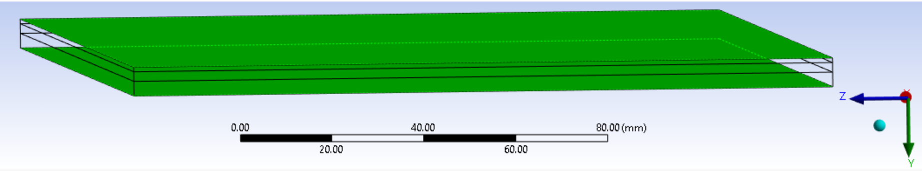

Figure 5-9: Surfaces (in green) on which the convective thermal load was applied in the MRCC convective cure analysis. The temperature of the convective load is set to 22°C.

cure. The temperature of the laminate is generally uniform and follows the cure cycle closely, with some overshoots at the end of ramps (see Fig. 5-10) due to the exothermic nature of the resin in the composite. This matches with laminate temperature profiles during convective curing found in literature [14, 123, 124].

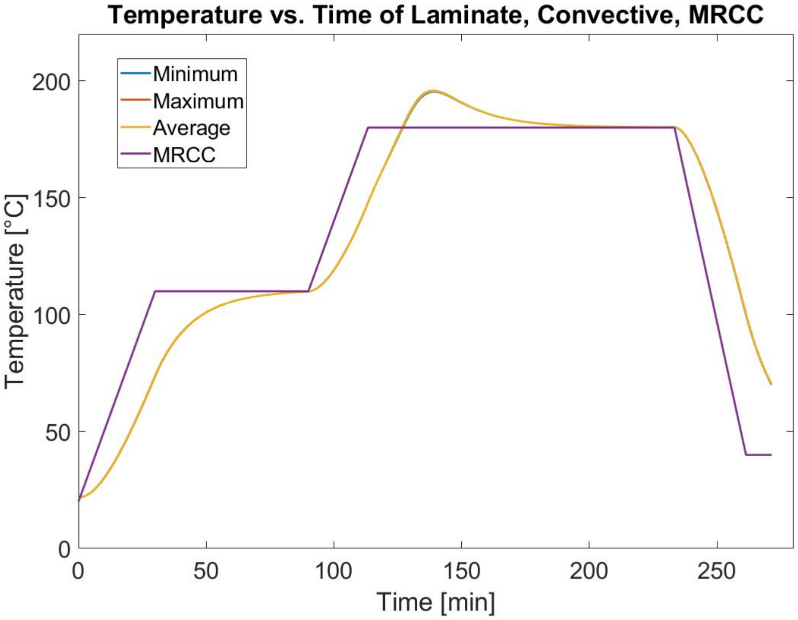

Figure 5-10: Temperature across the laminate in the simulated convective MRCC cure. Note the overlap of the minimum, maximum, and average lines, indicating a uniform temperature across the thickness of the laminate.

For the conductive cure models, a convection load was applied instead to just the top surface of the stack-up, with the temperature set to 22°C for the entire cure cycle, and the convection coefficient was set to 5 $\frac{W}{m^2\text{-}°C}$ under the assumption of natural convection (Fig. 5-11), also following prior work [118]. A temperature load of 22°C was applied to the bottom of the stack-up, coinciding with conduction with an external surface that is under ambient temperature conditions (Fig. 5-12). This was done to best replicate later experimental work, where the stack-up is placed on top of an aluminum plate that is at room temperature, although for parts cured while suspended, a bottom convection load replicating the convection load on the top of the stack-up would be more accurate. Both initial conditions were tested for the model and there was not a significant difference in the results, due to the low thermal conductivity of the insulation material. The cure cycle being tested was applied to the top surface of aluminum touching the laminate (Fig. 5-13), a proxy for the CNT heater.

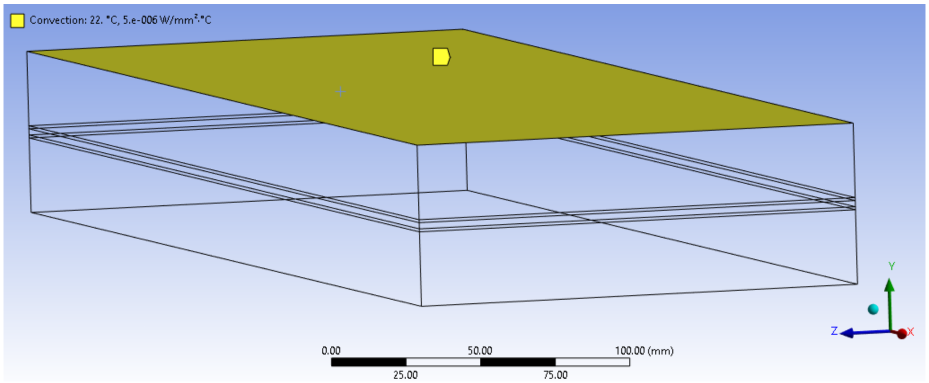

Figure 5-11: Convection load applied under the assumption of natural convection between the top of the stack-up and the environment in the conductive curing analysis.

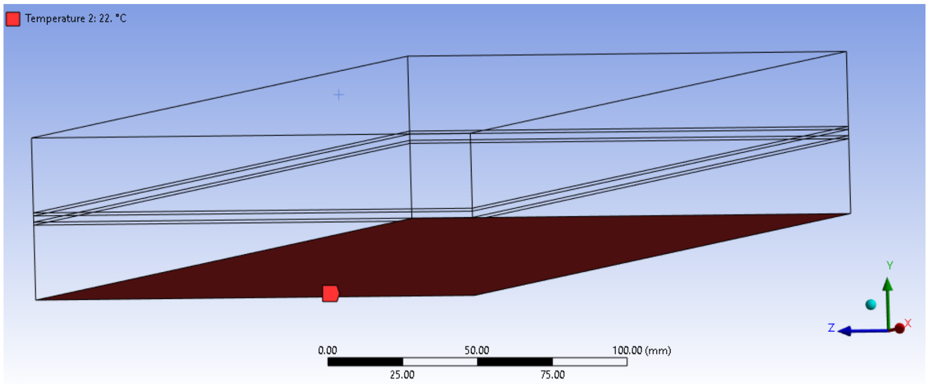

Figure 5-12: Temperature load of stack-up with nearby surroundings at room temperature in the conductive curing analysis.

An initial MRCC via conductive curing was tested to ensure that the predicted DoC was comparable to that of convective curing. The DoC was found to range from 90.33% to 91.24%, with the heater side having the maximum DoC, leaving the opposite side of the laminate with a 0.99% decrease in DoC. The MRCC and temperature of the laminate were very closely intertwined, due to the nature of the heating mechanism, as well as the lack of thermal barriers, an advantage to direct conductive curing (Fig. 5-14). However, it is important to note that the temperature is no longer uniform, with sections of the laminate further from the heater having a

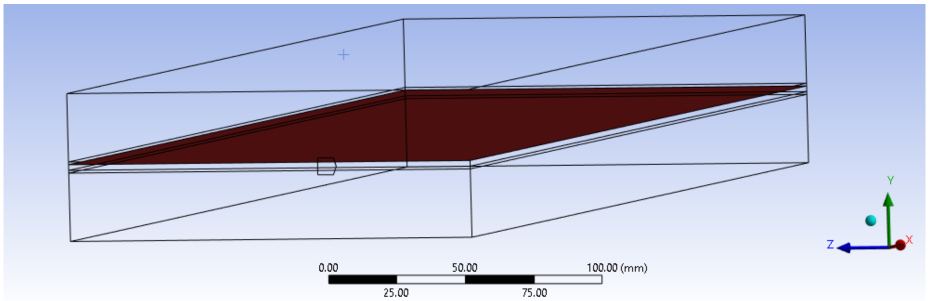

Figure 5-13: CNT Heater representation in conductive curing analysis. A temperature load set to the cure cycle being tested is applied to the top aluminum plate surface that is in contact with the laminate.

larger decrease in temperature, up to ∼ 2°C during the 2 hour 180°C hold (Fig. 5-15). One important observation to make is the lack of thermal runaway behavior observed in the conductive cure. This is due to heat being conducted away from the laminate to both the tooling as well as the insulation, which acts as a heat sink, preventing the exothermal reaction from causing overheating. This proves to be useful in the experimental work as well, allowing for accurate adherence to the cure cycle.

5.1.3 Optimized Cure Cycles

With the MRCC conductive OoO cure model, optimization of the cure cycle can be conducted. Commands in ANSYS Mechanical Scripting can be utilized in a Python script to conduct certain tasks, such as setting values for parameters of any object (mesh, thermal load, step configuration, etc.). An organizational tree of the Mechanical Scripting data structure is shown in Fig. 5-16.

From this, a function that was able to set a cure cycle, adjust step times, and gather solution results was created, utilizing the Mechanical Scripting organizational syntax, and completed the following:

1. Define ramp rates to first and second holds, ramp rate of the final cool down, initial (room) temperature, initial temperature of the first hold, final temperature of the first hold, and temperature of the second hold (see Fig. 5-17.

2. Define each time in which the slope of the temperature vs. time graph is dis-

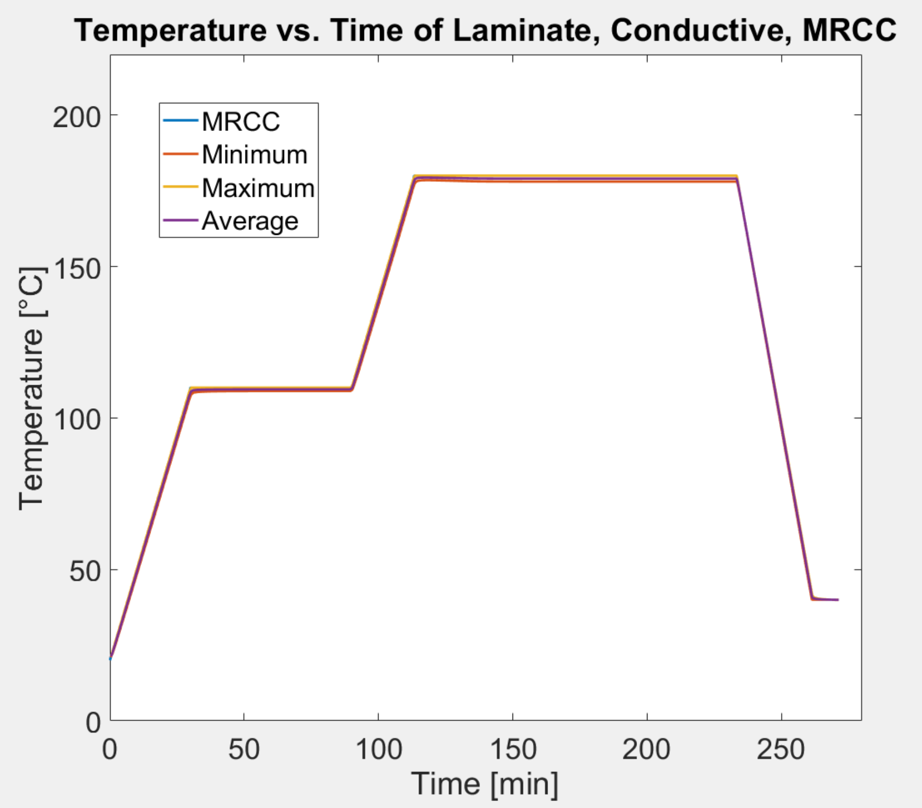

Figure 5-14: Temperature across the laminate in the simulated conductive MRCC cure.

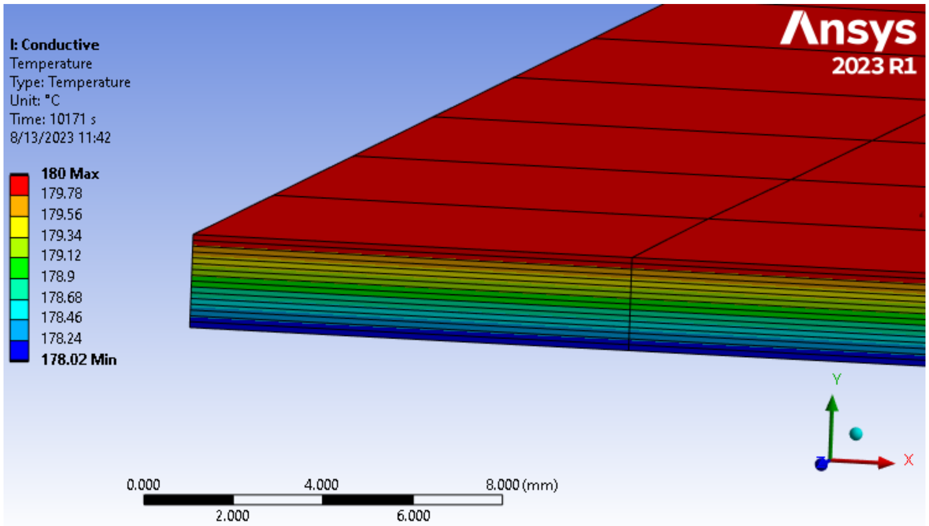

Figure 5-15: Temperature distribution across the thickness of the laminate at ∼170 minutes into the cure (during the 2 hour 180°C hold) in the MRCC conductive OoO (CNT heater) curing.

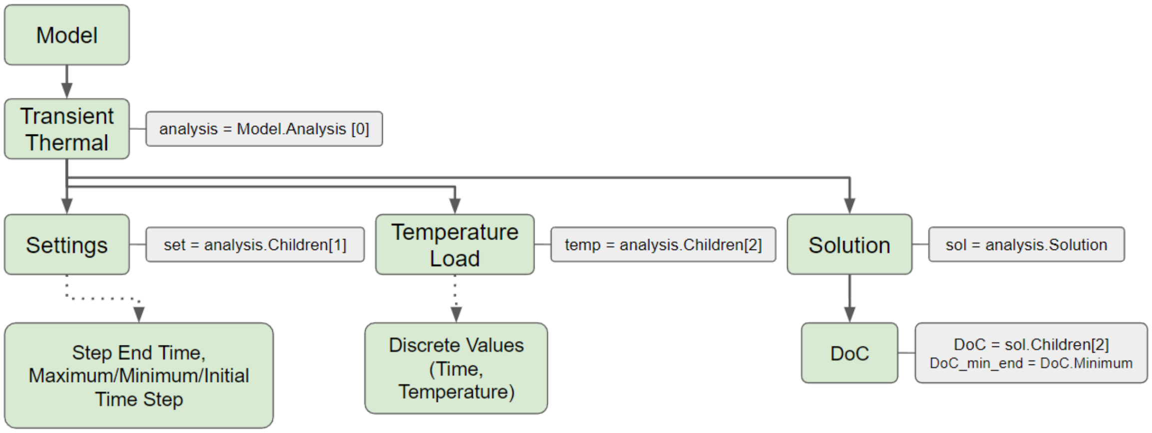

Figure 5-16: Data structure of ANSYS Mechanical, with major Mechanical Scripting objects used in the base function.

continuous.

3. Set step end times for the end of the first hold, end of the second hold, end of the cool down, and the final step after cool down.
4. Using the times gathered in (2) and the temperatures defined in (1), define the temperature vs. time cure cycle using the temperature load already present in the model.
5. Solve the system and gather DoC values from the end of the cure, as well as prior to the second ramp up (when gelation is to occur).
6. Calculate the total time of the cure cycle.

Of the plethora of optimization algorithms to choose from, the final trade came down to two optimization programs: the Limited-memory Broyden-Fletcher-Goldfarb-Shanno with Bound constraints (L-BFGS-B) local optimization method [125, 126] from the scipy.optimize.minimize library, and the differential evolution (DE) global optimization method [127] from the scipy.optimize library. The L-BFGS-B algorithm works by calculating the objective function, then gathering approximations of the gradient and Hessian by taking small steps in a direction with one variable while keeping all others fixed, for each of the free variables being optimized. Variable jumps are calculated based on the information gathered in order to minimize the objective function in subsequent trials. It is inherently a local optimization method as a result of its inability to explore other minima. Alternatively, DE works by creating a population of solutions, evaluating the fitness of each of the solutions in the population, creating solution mutations based on a chosen strategy (of which there are several), crossing over individual parameters between the trial solution from the mutation and the original solution with a prescribed probability, comparing the fitness of the crossover solution to the fitness of the original, and taking the better (smaller objective function value) of the two to redefine the population. The performance of DE heavily relies on the parameters chosen for mutation and crossover, which affect how much of the solution space is explored. Through mutation and crossover, the DE algorithm is able to optimize globally.

The generally monotonically increasing/decreasing nature of time and DoC due to variation in the parameters, the ability to represent the optimization problem by a single objective function value, and the long calculation time for an objective function (due to running the Transient Thermal solver in ANSYS for each calculation of the objective function) are what make the L-BFGS-B algorithm the best candidate for this study. DE might be better suited if a multi-objective optimization was required, but generally, much more runs are required for DE to successfully optimize.

The cure cycle can be defined using many parameters. However, to simplify the cure cycle, it was reduced to the parameters shown in Fig. 5-17. From these parameters, the cure cycle is fully defined, and an objective function is used as a measure of the fitness of the solution. Time, DoC at the end of the cure, DoC prior to Ramp 2, and temperature of the first hold are of interest to the objective function. It is important to minimize time, maintain a DoC of between 90 and 95%, maintain a low viscosity for the entire duration of the first temperature hold by maintaining a sufficiently low DoC prior to Ramp 2, and raise the temperature of the first hold to as high a value as possible to enable the lowest possible viscosity of the resin, enhancing void evacuation.

Time is defined as the total time required to arrive at 40°C during the cool down.

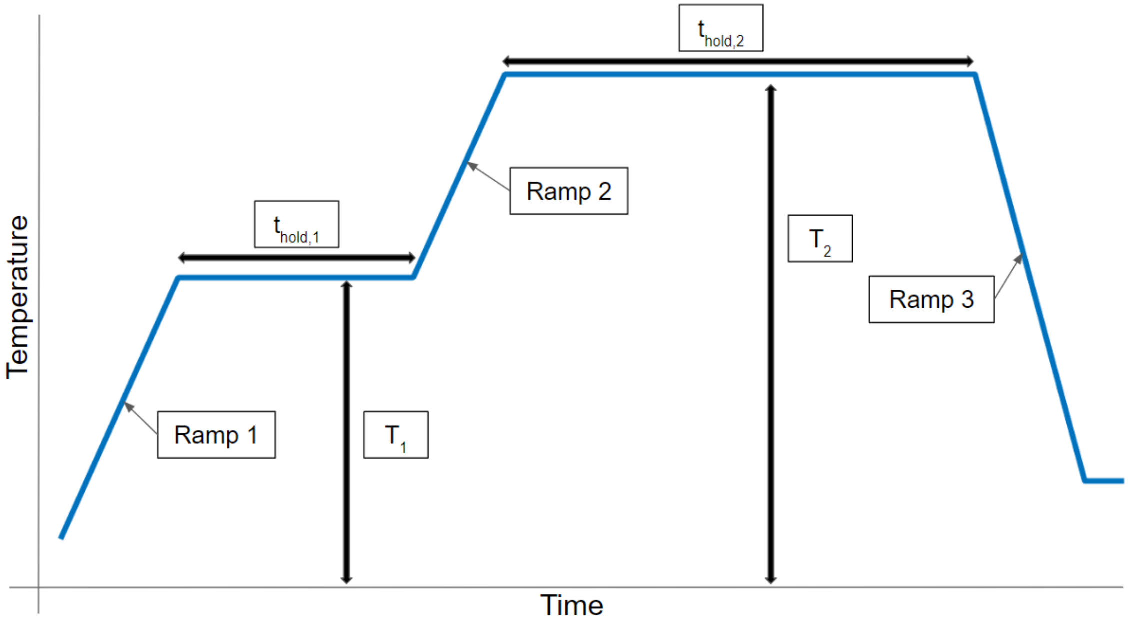

Figure 5-17: Parameters available for optimization in a 2-stage cure cycle framework.

In order to calculate it in the code for the optimization, the following formula was used, finding the time as a function of the cure parameters:

$$t_{cure} = \frac{T_{1,start} - T_{RT}}{Ramp\ 1} + t_{hold,1} + \frac{T_2 - T_{1,end}}{Ramp\ 2} + t_{hold,2} + \frac{T_{final} - T_2}{Ramp\ 3} \tag{5.4}$$

$T_{1,start}$ and $T_{1,end}$ were distinguished to allow for optimization in the case of the first cure cycle, but generally, $T_{1,start} = T_{1,end}$. It is important to include the cooling, as cooling from 200°C takes more time than cooling from 180°C, which should be accounted for in the calculation of time. For the fastest possible MRCC (3°C heating, -5°C cooling), the final time is 261.33 minutes under this framework. It is important to note that for a typical MRCC autoclave run, with 2°C/min ramp up and cool down ramp rates, the final time is 330 minutes. To calculate the time saved, the most conservative value of 261.33 minutes is used.

To enforce constraints on the DoC, a penalty system was implemented into the objective function. Penalties are used to deter the optimization algorithm from solutions that violate constraints and are implemented by adding or multiplying the objective function by a penalty function that increases the value of the objective function artificially [128]. For the optimization of the cure cycle, penalties were applied via additive functions that each equaled 0 if the constraint was met, and equaled 1000 if the constraint was not met for each constraint. 1000 was chosen as it was an order of magnitude higher than typical objective function values, allowing for easy differentiation between acceptable and unacceptable solutions. Penalties were also slightly adjusted to ensure that parameters were not optimized within a penalty region. For example, if the DoC was too low, the penalty would raise the objective function to a high amount. However, as time is part of the objective function, lowering time would still improve the value of the objective function, even though the DoC is failing to meet its constraint. Time would continue to decrease as a result, when in fact, it needed to increase to raise the DoC. In this example, the penalty was adjusted such that the objective function is additionally penalized for lowering the time and rewarded for raising the time, in these types of regions.

To obtain the final objective function, weights were applied on certain values (for example, the distance from a prescribed final DoC value) such that changes in all important values would be reflected on a similar order of magnitude. The objective function structure for the optimization is the following:

$$OBJ = t_{cure} - T_1 + W_1|DoC_{PG} - DoC_{PG,D}| + W_2|DoC_F - DoC_{F,D}| + P_1 + P_2 \quad (5.5)$$

where PG is pre-gelation, or prior to the second ramp, F is final, P is penalty function, W_1(set to 500) and W_2(set to 50) are constants to weigh the effects of constraint variable divergence from an ideal value, and D is desired. DoC in Eq. (5.5) is a number between 0 and 1, rather than a conventional percentage value, as that is the output given by ANSYS. The DoC_F is based on the minimum DoC at the end of curing. This is to ensure the minimum DoC requirement is met across the entire laminate. Overshooting any maximum DoC constraint set in these analyses was not accounted for due to the low variability in the DoC across the laminate.

To simplify the optimization, major assumptions were made based on general knowledge gained from running simulations in order to reduce the number of variables.

First, it was noted that the program always favored high ramp rates, as they reduced time inevitably. Thus, Ramp 1 was permanently set to 15°C/min (5 times increase in speed compared to the highest MRCC ramp rate of 3°C/min), and Ramp 2 was permanently set to 10°C/min (lower Ramp 2 to avoid extreme residual stresses during gelation and post cure, also used in [118]). The maximum magnitude ramp rate of cooling in the MRCC of -5°C/min was used to ensure slow cooling as well (Ramp 3). The temperature T_2 was set to 200°C, as the optimization favored post curing at higher temperatures due to the resulting reduction in hold time. 200°C has also been seen in previous work [118] and approaches the glass transition temperature T_g for cured dry AS4/8552 of 200°C [70].

Viscosity values were not accounted for in the optimization's objective function, resulting in the loss of importance of the first hold time in the perspective of the optimization. As a result, the first hold time was reduced to prescribed values that were assumed to suffice for effective void evacuation, due to the already significantly increased ramp rate that further reduces resin viscosity [129], as well as the increased temperature during the first hold that will maintain a lower viscosity compared to MRCC, allowing for the resin to remove voids in less time. The remaining variables available to optimize, the Hold 2 time and Hold 1 temperature, were used in the optimization. Two initial approaches (leading to Accelerated Cure 1 and Accelerated Cure 2) were taken for the optimization of the first hold, based on the rheology of AS4/8552 (Fig. 5-18).

The L-BFGS-B optimizer was given control of when to end the optimization. However, the step size used while the optimization is probing a location is set to 0.1, which perturbs both T_1 and $t_{hold,2}$ by 0.1. This was found to be low enough for the optimizer to have a sufficiently accurate calculated gradient, as well as high enough for there to be significant changes in the calculated DoC and Time (and objective function as a result) during each function evaluation (i.e. each ANSYS Transient Thermal run with the prescribed cure cycle). The optimization code that runs in the ANSYS Mechanical scripting interface, along with a Python code that runs on any Python shell to convert the text file to CSV values, is included in Appendix A and

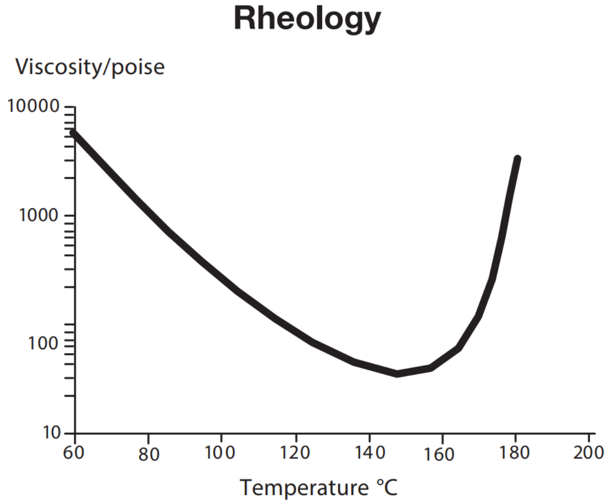

Figure 5-18: Rheology of AS4/8552 at a heating rate of 2°C/min. Note that the resin viscosity is lowest at ∼145°C. Figure from [70].

Appendix B, respectively.

Accelerated Cure 1

The central idea of the first approach was to be aggressive with respect to time. Instead of an initial hold, the optimization was geared to fit an initial spike up to 145°C, the lowest viscosity point based on rheology, and subsequently decrease for 20 minutes such that the DoC was kept to around 0.03 prior to the second ramp. T_1 was optimized to simply the endpoint of the 20 minute ramp down (i.e. $T_{1,start} = 145$, and $T_{1,end}$ is the variable being optimized). Next, $t_{hold,2}$ was optimized such that with the cure history, the DoC would be roughly 92.5%, erring on the side of less cured to minimize time, but going no lower than 91%. This was done using the prescribed DoC ($DOC_{F,D}$). The final ramp parameters are shown in Table 5.2. Convergence of the optimization to final time and DoC values is shown in Fig. 5-19 and Fig. 5-20. An important note to make is that in the graphs with penalties subtracted, the color values in Fig. 5-19 and Fig. 5-20 correspond to calculated objective function values as in Eq. (5.5), except with P_1 and P_2 left out. This is done to demonstrate the gradual adjustment of the objective function value without penalties changing the order of magnitude. Accelerated Cure 1 brings about a 65% decrease in cure time.

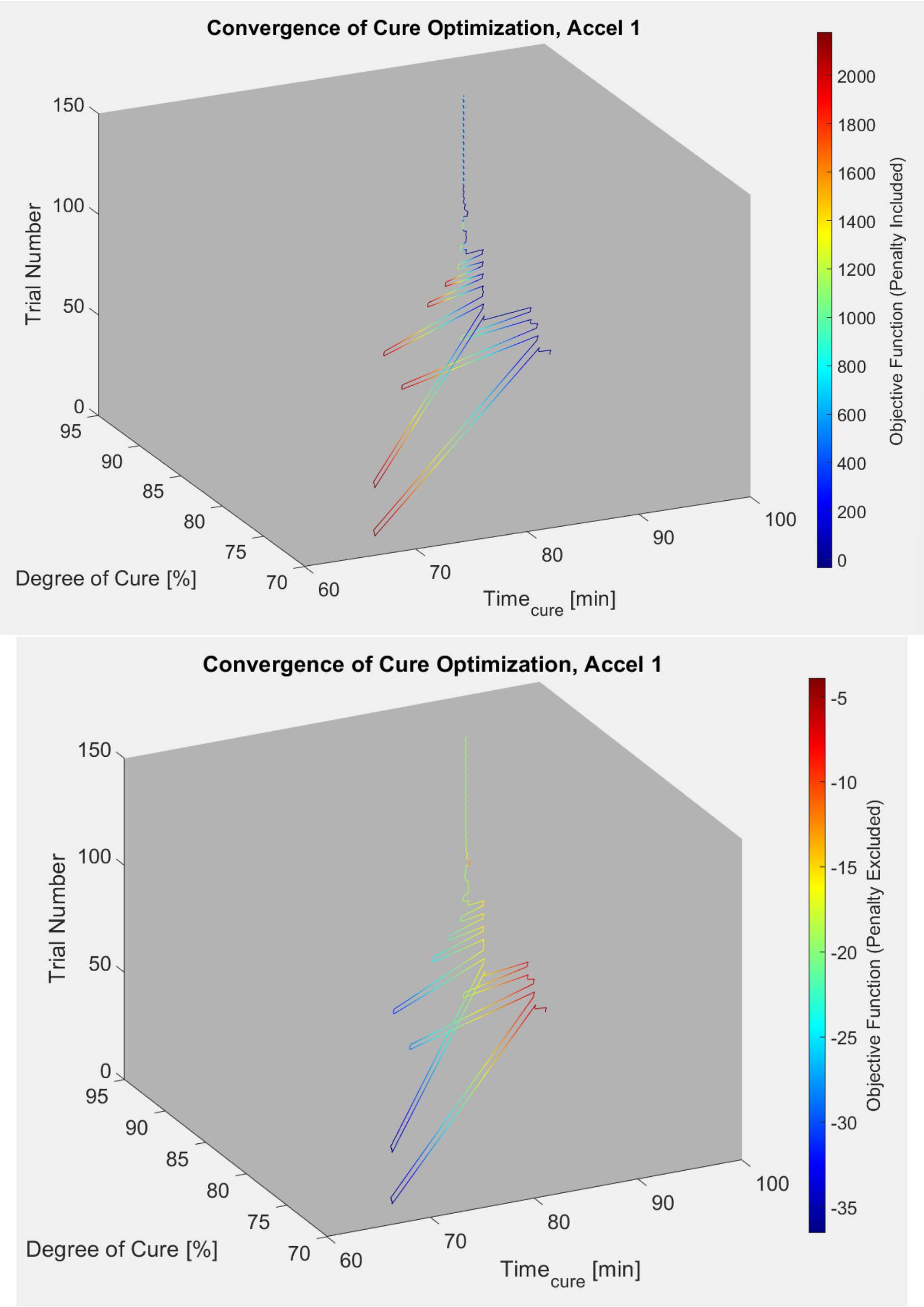

Figure 5-19: Accelerated Cure 1 optimization graphs, with penalty values subtracted in the bottom graph for reference. Convergence is across 144 objective function calculations. The final time of cure is 90.15 min, and the final minimum DoC is 91.53%.

Table 5.2: Final parameters for Accelerated Cure 1. **Note, this cure cycle specifically starts the first hold at 145°C and subsequently ramps down for 20 minutes to the T_1 value.

Cure Cycle Parameter	**Value**
Ramp 1	15°C/min
$t_{hold,1}$	20 min
T_1	119.52°C**
Ramp 2	10°C/min
$t_{hold,2}$	21.78 min
T_2	200°C
Ramp 3	-5°C/min

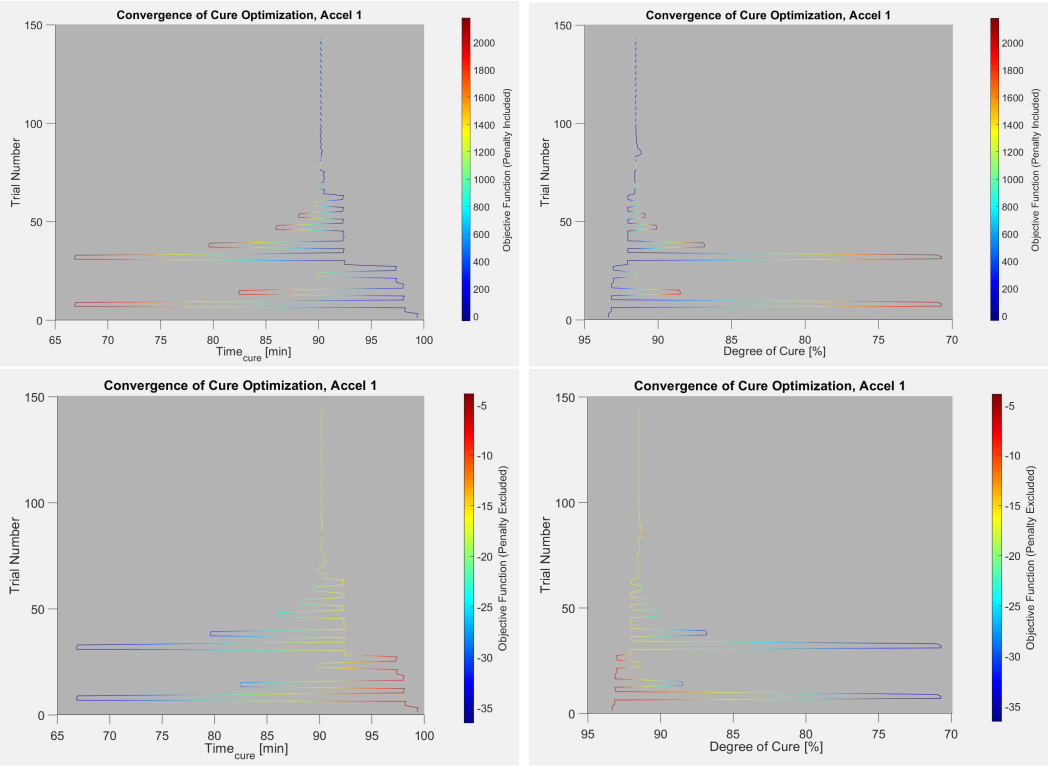

Figure 5-20: Accelerated Cure 1 optimization as a function of key objective function variables, with penalty values subtracted from the objective function calculation in the bottom two graphs for reference. Convergence is across 144 objective function calculations. The final time of cure is 90.15 min, and the final minimum DoC is 91.53%.

As expected, the optimization is highly dependent on time, while simply assuring an acceptable final DoC via penalties. If the DoC in the objective function was weighted too high, this would result in the loss of importance of time, and optimization would not yield the most time efficient values. However, if the DoC is weighted too low, then the optimization will simply converge to a DoC that is at the bottom of the acceptable DoC range, which could be problematic for the bridge to experimental testing. The final values of the constraints and time are shown in Table 5.3.

Table 5.3: Values of constraint and optimized variables for Accelerated Cure 1.

Variable	**Constraint**	**Final Value**
Maximum DoC, before gelation [%]	$\mathrm{DoC_{PG}} < 3$	2.9985
Minimum DoC, final [%]	$91 < \mathrm{DoC_F} < 95$	91.53
t_{cure} [min]	–	90.15

Accelerated Cure 2

The central idea of the second optimization approach was to be aggressive with respect to both desired laminate quality (particularly void removal) and time. This optimization keeps a constant first hold temperature to maintain a constant viscosity throughout the void removal step. Furthermore, the first hold time is increased from 20 to 25 minutes for a longer available window for void evacuation. The desired DoC before gelation is set to 5% instead of 1%, with penalty bounds from 4% to 6%. The desired DoC is set to 94%, and the constraint on the DoC is set from 94% to 95%, to ensure a sufficiently cured laminate. The final ramp parameters are shown in Table 5.4. Convergence of the optimization to final Time and DoC values is shown in Fig. 5-21 and Fig. 5-22. The behavior of the optimization in Accelerated Cure 2 is different than that of Accelerated Cure 1. This is due to the starting point of each optimization. In the Accel 2 optimization, the initial trial is started much closer to the final solution, as a general idea of the solution is already known based on results from Accel 1. This closer initial starting position results in a more gradual convergence that does not experiment with lower objective function values that violate penalty constraints. The convergence slowly approaches the final solution, as the calculated gradient is found to be initially low by the optimizer. This is not the case in the Accel 1 optimization. In the graphs where the penalty is not reflected, Accel 1 appears to optimize to a value that is not ideal (i.e. orange), since it has previously done trials with a low objective function (without penalties). However, in the graphs with penalties included, the optimization shows the behavior of improving as the trial number increases. In the dark blue regions of the Accel 1 graph without penalties included, the objective function value is actually high when the penalty is included. Accelerated Cure 2 brings about a 60% decrease in cure time.

Table 5.4: Final parameters for Accelerated Cure 2.

Cure Cycle Parameter	**Value**
Ramp 1	15°C/min
$t_{hold,1}$	25 min
T_1	134.58°C
Ramp 2	10°C/min
$t_{hold,2}$	33.44 min
T_2	200°C
Ramp 3	-5°C/min

In this case, the optimization was allowed to optimize the DoC toward the minimum bound value of 94%. An important distinction from the first cure optimization is the starting point of the optimization. For this second optimization, the starting point was started close to what was expected to be the final result, making the optimization more local. As such, the range in which the search is conducted is much less compared to the first optimization. Final values of the constraints and time are shown in Table 5.5.

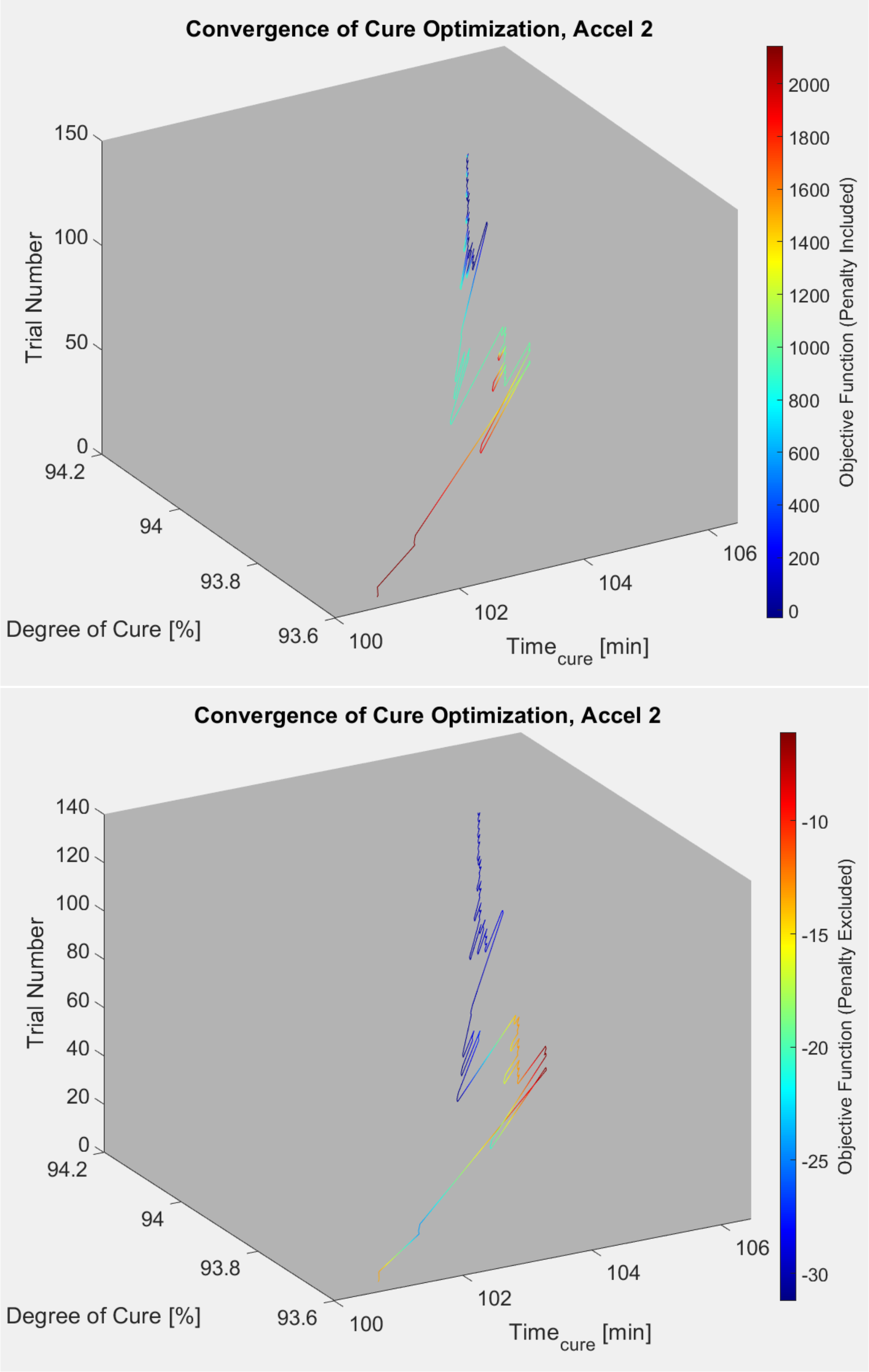

Figure 5-21: Accelerated Cure 2 optimization graphs, with penalty values subtracted in the bottom graph for reference. Convergence is across 137 objective function calculations. The final time of cure is 104.62 min, and the final minimum DoC is 94.08%. Note that penalties are subtracted from the objective function values.

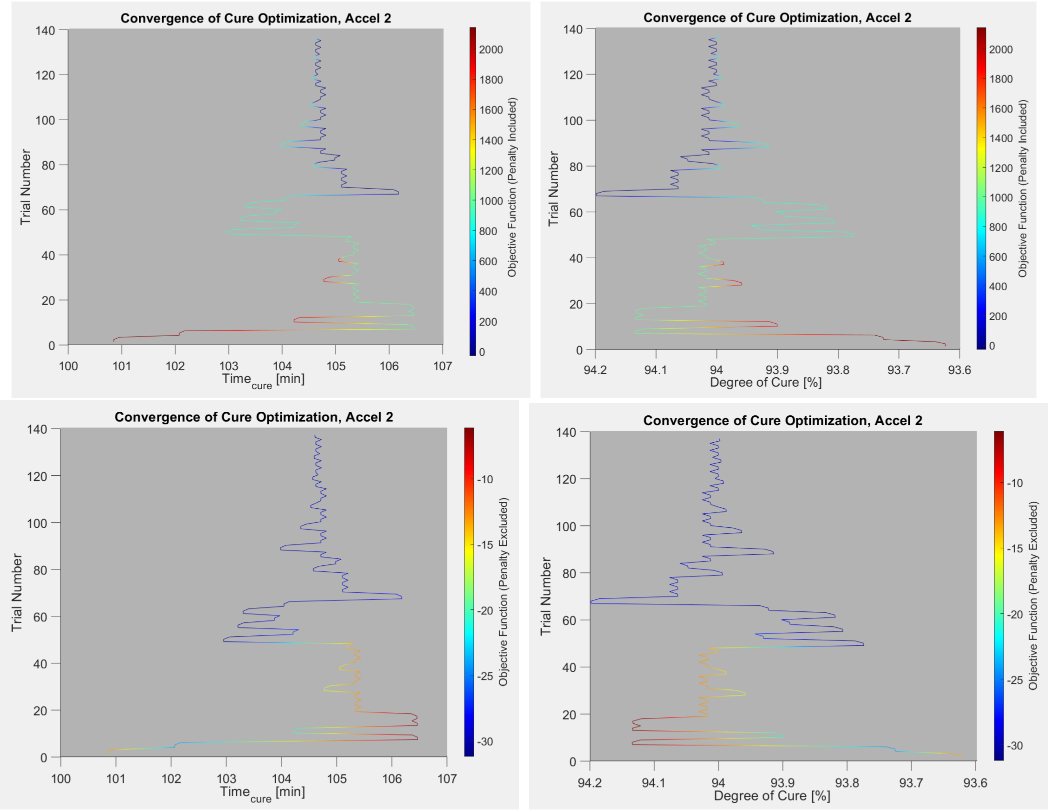

Figure 5-22: Accelerated Cure 2 optimization as a function of key objective function variables, with penalty values subtracted from the objective function calculation in the bottom two graphs for reference. Convergence is across 137 objective function calculations. The final time of cure is 104.62 min, and the final minimum DoC is 94.08%. Note that penalties are subtracted from the objective function values.

Table 5.5: Values of constraint and optimized variables for Accelerated Cure 2.

Variable	**Constraint**	**Final Value**
Maximum DoC, before gelation [%]	$4 < \mathrm{DoC_{PG}} < 6$	4.9976
Minimum DoC, final [%]	$94 < \mathrm{DoC_F} < 95$	94.08
t_{cure} [min]	–	104.62

Accelerated Cure 3

As discussed in the limitations of the model, the cure cycle optimization scheme developed thus far does not account for resin infiltration with any given metric besides the requirement of an initial hold for a prescribed time that is assumed to be sufficient for resin infiltration. In an attempt to account for resin infiltration in accelerated cure cycles, a framework was developed for creating cure cycles that have a similar amount of resin infiltration, measured by a metric defined in previous literature [130]. A measure of resin flow in a given cure cycle as defined by [130] is the following:

$$N_{flow} = \int_0^{t_{gel}} \eta(t)^{-1} dt \tag{5.6}$$

where η is the average viscosity of the resin across the laminate, t_{gel} is the time at which gelation occurs during the cure cycle, and N_{flow} is the coefficient to measure resin flow. is As time increases, N_{flow} increases, and as η decreases, N_{flow} increases, which are the expected relationships between the two variables and resin flow. Due to the relationship between N_{flow} and time, the prescribed time was increased to 40 minutes. Next, in order to calculate the viscosity curves for each modeled cure cycle, the Wichita State model for viscosity for Hexcel 8552 resin [131] was utilized, which has been shown to correlate well in rheology through ramp rates of 1-4°C/min. Eq. (5.7) is used to define viscosity as a function of temperature and DoC, and the parameters that were used for the model (as identified by [131]) are shown in Table 5.6.

$$\eta(T,x) = \begin{cases} \eta_{01} e^{\frac{E_1}{RT}} + \eta_{02} e^{\frac{E_2}{RT}} \left(\frac{x_g}{x_g - x}\right)^{A+Bx+Cx^2} & \eta \leq \eta_{max} \\ \eta_{max} & \eta \geq \eta_{max} \end{cases} \tag{5.7}$$

This viscosity model was implemented into all ANSYS Transient Thermal analyses as a user defined result. In order to create a time history with respect to viscosity to supplement the time histories of temperature and DoC within the ANSYS model. However, with the current optimization framework, optimizing with respect to viscosity is possible, but would take extensive time to do so. ANSYS Mechanical coding supports IronPython, Cython, and Python (via shell). Some ANSYS Mechanical ob-

Table 5.6: Values of parameters for use in the 8552 resin viscosity model from [131], valid in the temperature range of 25°C to 250°C and viscosity range of 0.1 to 10^6.

Variable	**Value**
η_{01}	7.5E-11 Pa-s
η_{02}	4.81E-02 Pa-s
E_1	81908 J/mol
E_2	13228 J/mol
x_g	0.545
A	2.466
B	0
C	0
η_{max}	1E6 Pa-s

jects (namely, the only object that can access time history data of averaged values of temperature and DoC across the laminate) are only available for use within the IronPython interpreter ANSYS provides. However, the optimization scheme implemented uses the SciPy library, which is inaccessible to the IronPython 2.7 interpreter. Due to this version mismatch, importing values of any variable with respect to all time steps from ANSYS is not currently available to utilize in the SciPy library-based optimization code. Variable values from a single time step can be retrieved, but this requires a recalculation of the results across the entire model to make the value available to the optimization, which would require heavy computing or extensive time. Once the proper objects are able to be called in Cython/Python in the ANSYS environment, one could use the viscosity time history, integrate across the time history to obtain values for N_{flow}, and optimize based on time, DoC, and N_{flow}, an avenue for future work. In this work, a manual search across the variable space of cure cycle parameters was conducted until a cure cycle with a comparable N_{flow} to the MRCC was found (551.22 for Accelerated Cure 3, 536.44 for MRCC). From having experience from previous experimental data (as will be explained in Sec. 5.2), the 200°C hold was increased to 36.5 min. The final ramp parameters are shown in Table 5.7. Final values of the constraints and time are shown in Table 5.8. Accelerated Cure 3 brings about a 52% decrease in cure time.

Table 5.7: Final parameters for Accelerated Cure 3.

Cure Cycle Parameter	**Value**
Ramp 1	10°C/min
$t_{hold,1}$	40 min
T_1	132.5°C
Ramp 2	10°C/min
$t_{hold,2}$	36.5 min
T_2	200°C
Ramp 3	-5°C/min

Table 5.8: Values of constraint and optimized variables for Accelerated Cure 3.

Variable	**Constraint**	**Final Value**
Maximum DoC, before gelation [%]	–	10.506
Minimum DoC, final [%]	–	94.46
t_{cure} [min]	–	126.5

Viscosity and Cure Cycle Summary

The cure cycles for all panels done experimentally (see Fig. 5-23), as well as the predicted viscosity profiles based on the NIAR model [131] are displayed for reference (see Fig. 5-24). The extended cure cycle to be further developed in Sec. 5.2 was not obtained from optimization, but the viscosity profile was modeled and displayed for reference. The results are summarized in Table 5.9.

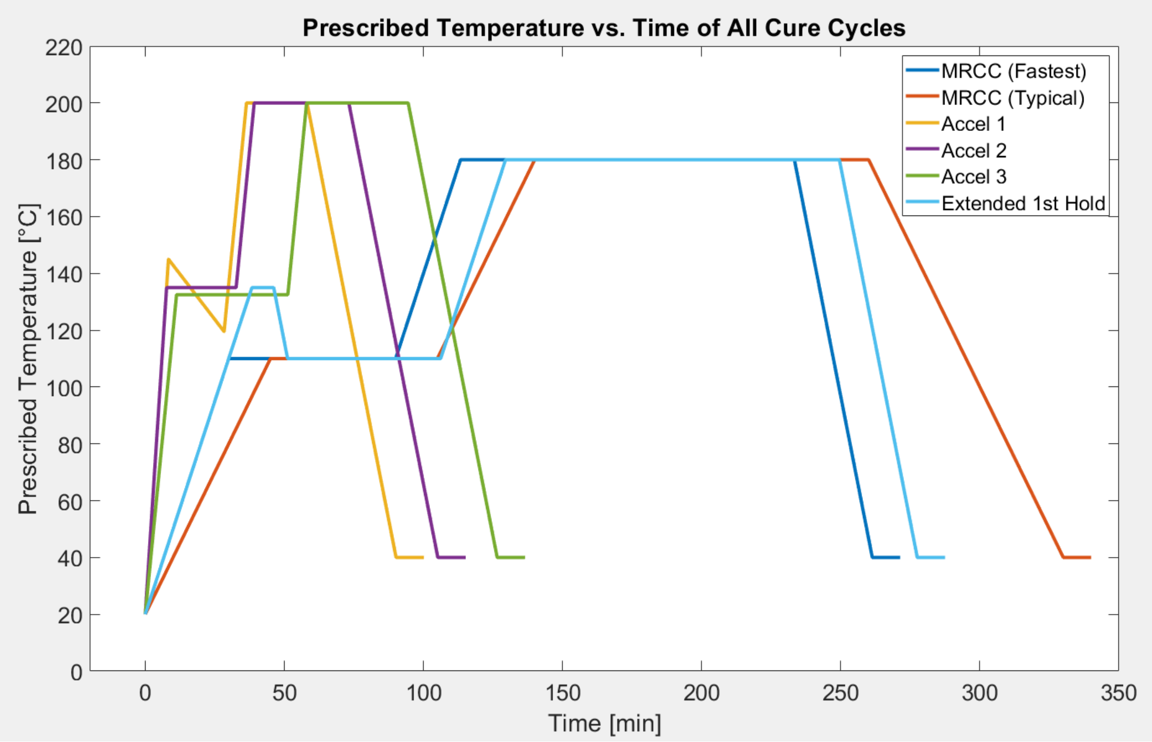

Figure 5-23: All cure cycles studied in modeling and experimental work, and a typical autoclave MRCC cure cycle for reference.

Table 5.9: Cure cycle summary of t_{cure}, modeled DoC (min-max range), and calculated N_{flow} coefficients based on model data.

Cure Cycle	**t_{cure} [min]**	**Modeled DoC [%]**	**N_{flow} [-]**
Extended Cure	277.5	90.37 - 91.28	614.35
MRCC	261.33	90.33 - 91.24	516.44
Accel 1	88.33	91.53 - 92.50	409.02
Accel 2	105.17	94.08 - 94.87	445.54
Accel 3	126.5	94.46 - 95.24	536.22

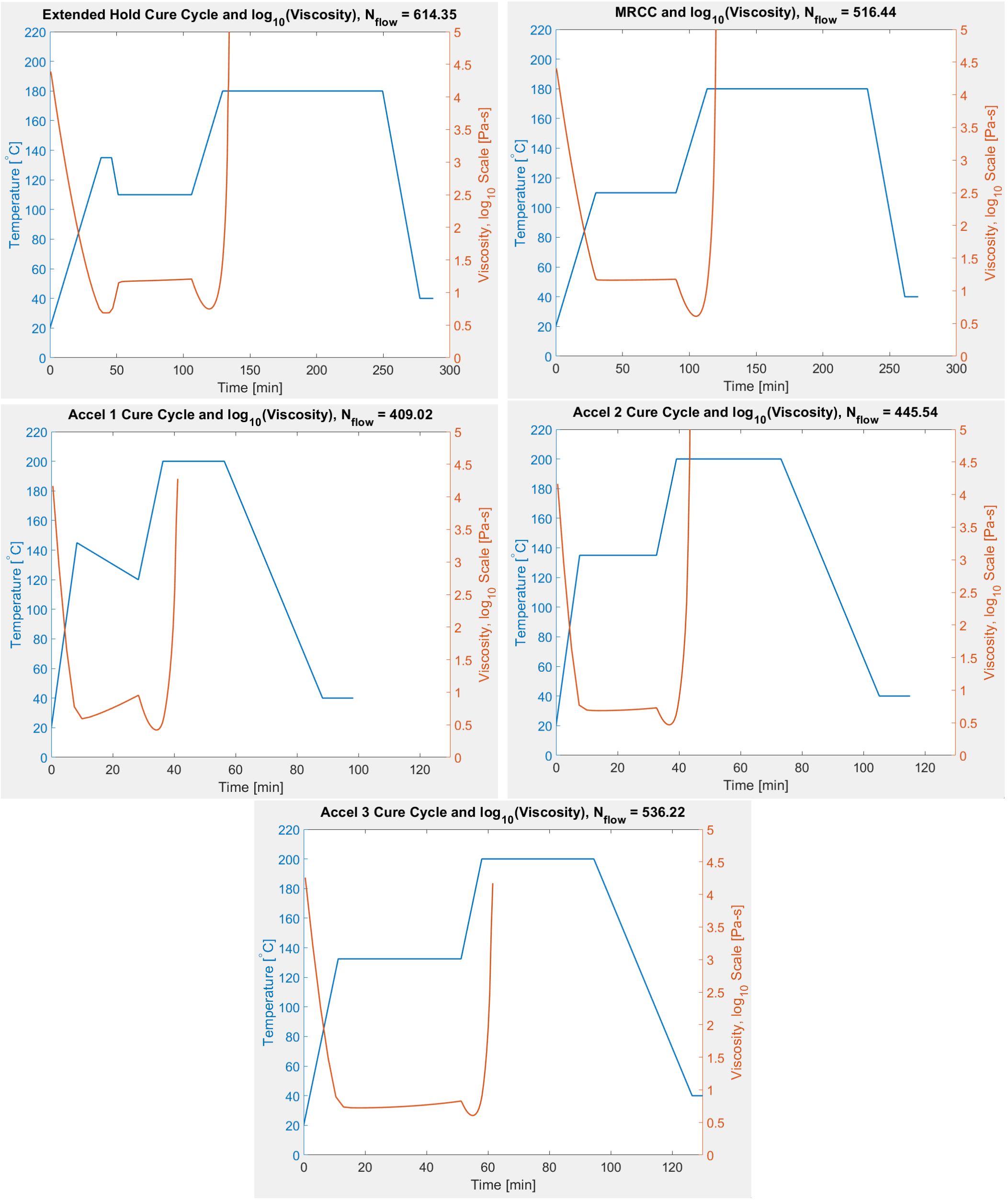

Figure 5-24: All cure cycles with their respective modeled average viscosity profile and calculated N_{flow}. Note the changes in time scale along the x-axis for the accelerated cure cycles.

5.1.4 Limitations of Model

Although the model is of high fidelity with respect to material constants and empirical data, there are still several shortcomings of the model. First, it is assumed that other elements that could potentially have an effect on the thermal properties of the manufacturing process (i.e. cork tape, vacuum breather) do not have a large effect compared to the components that are modeled. Next, the model does not account for variability along the thickness of the laminate as an optimizing metric, although this can be added in future work. The model also uses provided material properties, however, for more accurate results, material properties of the prepreg being used should be obtained experimentally and inputted into the model data. This model is also susceptible to numerical error, a common cause of inaccuracy within FE analyses.

This model serves as a framework for first passes at an optimized cure cycle for a simple geometric configuration and can handle more variables or geometrical configurations than utilized in this study via the objective function and penalty optimization scheme. However, it is important to note that each trial can take anywhere from 1-4 minutes, depending on computer processing power, how fine or coarse the time step mesh is, and especially the number of input variables being optimized, which adds one trial per probing step. This can cause the number of steps to increase significantly before a result is reached. However, simplifications based on knowledge of the system can be made to reduce run time and provide a first pass result for experimental OoO curing. Experimental analysis using the simple framework explores the ability of the model to provide accurate trends and results for important parameters. Void content and resin infiltration are not available for model consideration using ANSYS ACCS, which can lead to cure cycles that cure the laminate effectively but do not take into account void content, which can significantly impact material properties. This is explored in Sec. 5.2.

5.2 Experimental Analysis with CFRP Laminates

In this section, experimental validation of previously developed cures was conducted from the optimization scheme developed in Sec. 5.1.2. All cures are conducted using the OoO set-up in Sec. 5.2.1. Characterization of cured laminates is done by X-ray Computed Tomography (µCT), Differential Scanning Calorimetry (DSC), Dynamic Mechanical Analysis (DMA), and Short Beam Shear (SBS) mechanical testing. The material used is AS4/8552, an autoclave CFRP unidirectional prepreg, and is used in conjunction with electrospun polymer nanofiber (EPN) polyamide veils by Revolution Fibers, here defined as EPN NPNs (Type 1 EPN from Chapter 4). More information about the CFRP unidirectional prepreg can be found in Table 5.10.

Table 5.10: Properties of Hexcel AS4/8552 prepreg [70].

AS4/8552 Property	**Property Value or Characteristic**
Fiber	AS4 carbon fiber unidirectional
Fiber content by volume	~57.42 vol%
Nominal fiber density	1.79 g/cm^3 (0.065 lbs/in^3)
Resin matrix	8552 thermoset polymer
Resin content by weight	35 wt%
Nominal resin density	1.3 g/cm^3 (0.047 lbs/in^3)
Reinforcement reference	AS4 12K
Glass transition temperature T_g, dry	200°C (392°F)
Gel time at 177°C (350°F)	13 min
Cured ply thickness	0.130 mm (0.0051 in)

5.2.1 CNT Heater OoO Set-up

An aluminum plate of dimensions 457.2 mm (18 in.) x 457.2 mm (18 in.) x 3.175 mm (0.125 in.) is used as a holder of all materials in the set-up. On top of this plate resides a 228.6 mm (9 in.) x 215.9 mm (8.5 in.), 25 mm thick block of Super Firetemp® X insulation. Next, a 228.6 mm (9 in.) x 215.9 mm (8.5 in.), 1 mm thick aluminum plate is placed on top of the insulation as a tool surface for the laminate. The insulation/tool surface pair is wrapped in guaranteed non-porous Teflon (GNPT) film (Airtech Release Ease 234 TFNP). Next, the laminate stack-up is completed atop the tool surface as normal, as described in Sec. 5.2.2 and shown in Fig. 5-26. Afer the sample is prepared, a CNT heater is placed in contact with the oversized GNPT film, covering the entire area of the laminate. In this set-up, the area of CNTs in the CNT heater measured 152.4 mm (6 in.) x 152.4 mm (6 in.). The heaters provided by Metis Design Corp. were made with commercially available 7gsm CNT non-woven mats. Two conductive strips of material, each measuring 152.4 mm (6 in.) x 25.4 mm (1 in.) surround two parallel edges of the square CNT mat, creating a heater with final dimensions of 152.4 mm (6 in.) x 203.2 mm (8 in.). The heater is sandwiched by two polymeric films to protect the CNTs from debris and for electrical isolation. The total thickness is 0.18 mm in the heating region, and the heater has a measured ~3 Ω resistance. After the heater is placed on the oversized GNPT film, a 152.4 mm (6 in.) x 152.4 mm (6 in.) replica of the 1 mm thick aluminum tooling plate with 25 mm insulation wrapped in GNPT film that is on the bottom is placed on top, with the aluminum plate side in contact with the CNT heater. To measure the temperature during cure, a K-type thermocouple (Watlow OKK30B10A) is placed between the aluminum plate and the insulation. It is assumed that the CNT heater has negligible thermal mass compared to the laminate and adjacent tooling plates. The tooling plates help not only to maintain an equal pressure across the laminate but also to distribute temperature evenly across the laminate, although further testing is required to ensure there are negligible thermal gradients due to the 1 mm aluminum tooling plates. To provide electricity to the heater, one 18 AWG wire is connected to each of the CNT heater conductive strips via copper tape that utilizes an electrically conductive adhesive. The two 18 AWG wires and the thermocouple wire are guided outside of the vacuum bag by routing them through the vacuum tape in order to connect them to the power circuit.

Proportional-Integral-Derivative (PID) control was utilized to enable highly accurate and power efficient adherence to the cure cycle being prescribed. First, the PID controller (OMEGA CN32PT-440DC) is powered using an AC to DC power adapter that outputs 24 V and 2 A into the DC powered PID controller. The PID controller connects to a laptop via a micro-USB to USB-A connection to utilize the PLATINUM Software for CNPT Series provided by OMEGA. The PID controller takes the thermocouple reading as input, while its output is the power to a solid-state relay (SSR). The SSR (Crydom D1D12) is used as a current switch for the PID controller to utilize. Taking in PID signals as input (i.e. thermocouple readings), the SSR completes or breaks the circuit as output. The SSR is placed within the heater to power supply circuit, which, when completed, runs direct current through the CNT heater at the prescribed voltage and current, a constant value that is adjustable via the power supply. The Multi-Range DC power supply (BK Precision 9201B) outputs maximum power and is bound by either a voltage or current threshold. The circuit is kept separate from the vacuum bag system. The OoO electronics set-up is shown in Fig. 5-25.

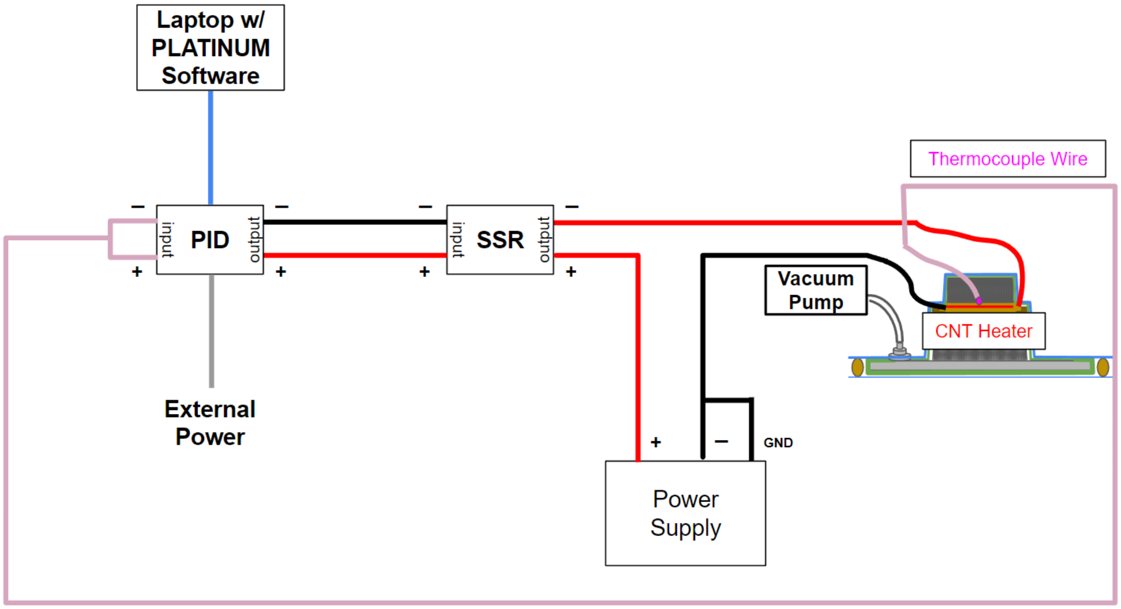

Figure 5-25: OoO cure electronics set-up.

5.2.2 Sample Preparation

An important note to make is that the extended hold cure was not optimized for, but rather done when first starting to set up the new OoO heater system. The cure cycle adhered to was programmed in the past from previous work in the lab and was used as it was mistaken for the MRCC. However, it produced the best results with respect to void content and is studied in detail for that reason, especially as no debulk step was used prior to curing.

For each cure, a 152.4 mm (6 in.) x 152.4 mm (6 in.) quasi-isotropic panel with 16 plies in a $[0/90/+45/-45]_{2S}$ layup was fabricated, with EPN NPN sheets placed between adjacent plies. The NPN was added to the layup in an identical manner as the prepreg. After completing each CFRP with NPN layup, a peel ply was applied to both top and bottom surfaces of both laminates for a smooth surface finish and effective resin wicking. Fully stacked laminates were surrounded by 25.4 mm (1 in.) wide and 3.175 mm (0.125 in.) thick cork tape (Batson Cork Tape- .125) along the edges, stacked in enough layers to exceed the thickness of the laminate. An oversized GNPT film was placed on top of the peel ply, in contact with both the laminate and the cork tape. The heater was then placed on top of the GNPT film, followed by the top tool plate and insulation component. Each cure was then surrounded by vacuum breather material (Northern Composites BR-NB3010) and sealed with a vacuum bag (Airtech Wrightlon 8400). Electrical wires were passed through the vacuum sealant tape (Aerovac SM5126). A Vacuum was pulled with a diaphragm pump (MD1C) and measured to be 28.5 inHg. The final stack-up is shown in Fig. 5-26. Laminates were set to a 3-hour debulk time prior to running the cure cycle, except for the Extended First Hold cure, which had no debulk step, as it was not implemented yet at the time of cure. After the debulk (or immediately for the Extended First Hold cure), the program was allowed to run, recording the time history of the recorded temperature measurements of the thermocouple. The actual temperature compared to the set temperature, along with power consumption data, is shown for all cures in Fig. 5-27.

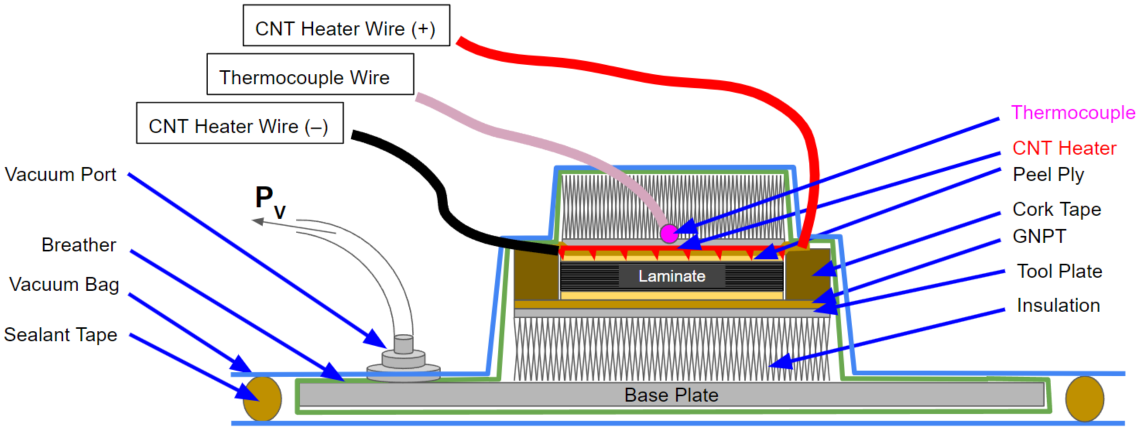

Figure 5-26: OoO laminate stack-up. Note that in the actual set-up, electrical wires are guided through the vacuum sealant tape.

It is important to note the error in the Extended First Hold Cure. This occurred due to the setpoint not being met during a step ramp down to the 110°C hold, which causes the program to cease operation. Besides this loss of signal, the setpoint is followed almost exactly. Another important note is that there are occasional spikes in the temperature reading during the cure that are quickly corrected, due to an error in the thermocouple readings. This causes a large PID compensation, which is visually apparent with the orange spikes in the graphs. These temporary errors do not affect the general shape of the curves.

Another important observation is the total energy consumed. The 232.25 cm^2 in area (2 mm thickness) MRCC OoO cure costs about 433 kJ of energy to cure. In previous work [14], it cost 118.8 kJ for a similar MRCC OoO cure of an IM7/M56 laminate with an area of 30 cm^2 and equal thickness, while the oven cure was found to consume 13.7 MJ (13700 kJ) of power for the same sized part. The energy savings found here for a larger part rival both previously found results, especially in the accelerated cure cycles. One thing to note, however, is that the required power draw for higher ramp rates in these OoO cures is significantly higher than previous work (~160-192 W vs. ~12.5 W), firstly due to oscillations, but also due to the low

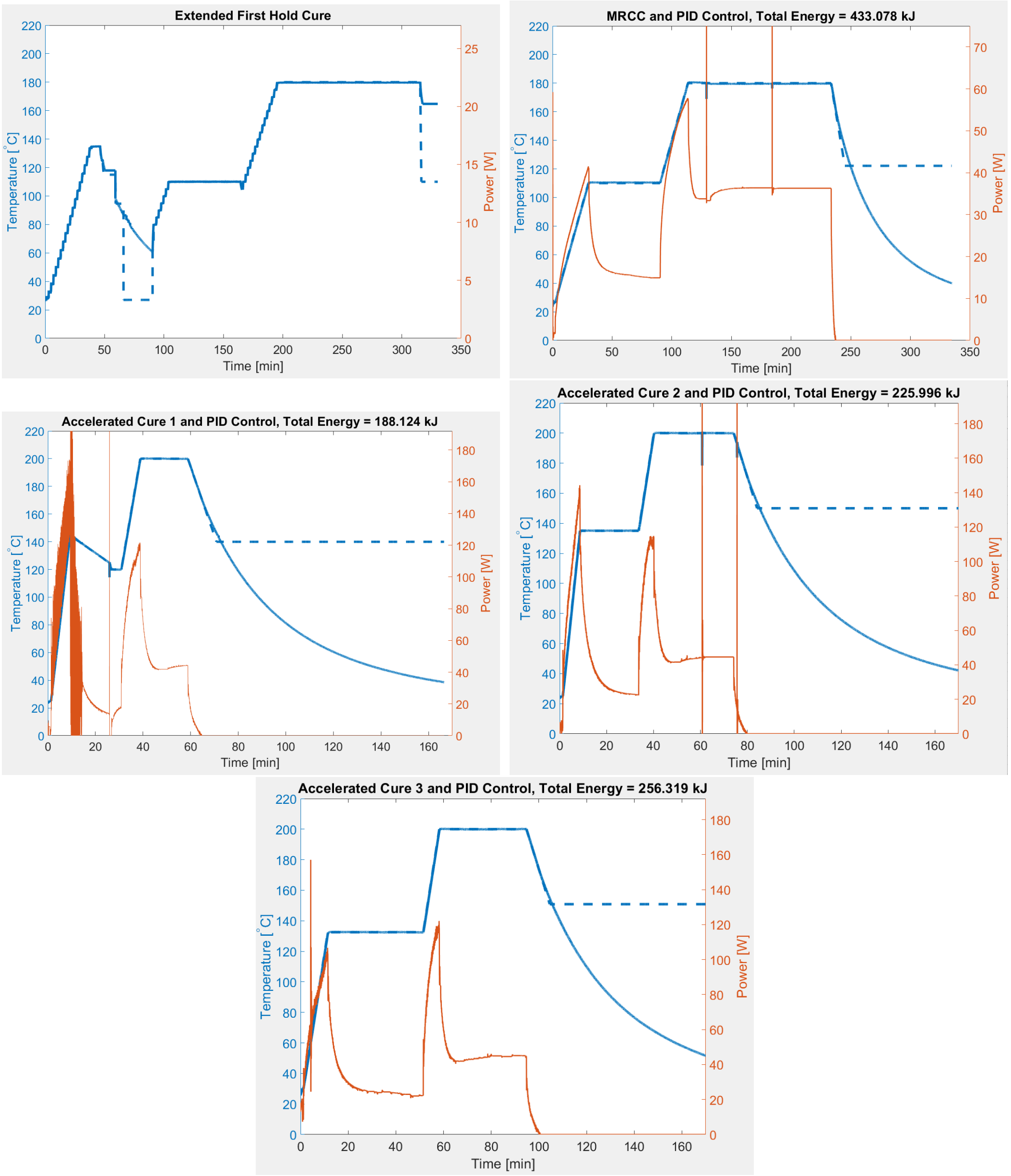

Figure 5-27: OoO cure cycles with power consumption and total energy of cure. Thermocouple temperature readings are in the solid blue line, while the set point is the dashed blue line. Spikes in PID graphs are due to thermocouple reading errors, where temporary jumps in the temperature result in PID compensation. The thick lines in Accelerated Cure 1 are due to PID instability, which was corrected during the run. A step profile and direct on/off control was used for the Extended First Hold cure cycle, so PID and power consumption data are not available for that cure. Once the cure began cooling at a rate slower than 5 °C/min, the cure cycle was manually ended, which produced the straight blue dashed lines in the graphs.

resistance of the CNT heater (3 Ω). With a higher resistance, more thermal energy is provided to the laminate via joule heating, which will reduce the power requirements significantly. This is an avenue for future work. The cures conducted in this study demonstrate the ability of the 152.4 mm (6 in.) x 152.4 mm (6 in.) sized CNT heater to heat the composites to prescribed cure cycles of varying ramp rates and temperature holds.

5.2.3 Quality of Manufactured Laminates

Laminates were checked for quality via µCT, DSC, DMA, and SBS testing. SBS was only done for samples that showed a low void content, which, as shown later in the section, is for both the extended first hold cure cycle, as well as MRCC. To retrieve test specimens from the cured laminate, a table bandsaw (MicroLux Variable Speed Mini Band Saw) with a diamond blade was used. A diagram of locations where specimens were drawn from cured laminates is shown in Fig. 5-28.

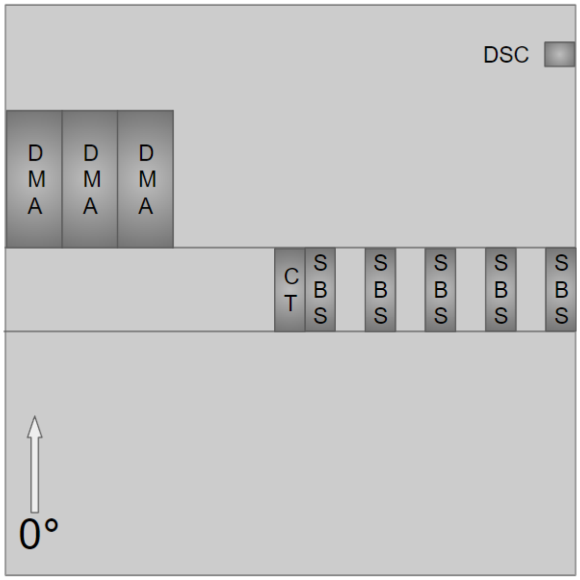

Figure 5-28: OoO laminate specimen locations (top-down view) after edges were removed (roughly 10 mm along each edge). The figure is not to scale.

Micro-Computed Tomography

µCT was used to check the void content of a laminate made with the old roll and the new roll, as well as cured interlaminar thicknesses. Specimens were retrieved from the center of each laminate and measured ∼12 mm x ∼4 mm x ∼2 mm. The scans were obtained using a Zeiss Versa 620 µCT, which uses the Scout-and-Scan™ Control System software to image 3201 projections of the sample as it rotates 360°. For the Extended First Hold cure, the scans were obtained with a field of view of approximately 2.3 mm x 2.3 mm, and a voxel size of approximately 1.16 µm, resulting in a resolution of approximately 3.5 µm. For all other cures, the scans were obtained with a field of view of approximately 3 mm x 3 mm, and a voxel size of approximately 1.5 µm, resulting in a resolution of approximately 4.5 µm. 80 kV and 10 W were used for all scans, with an exposure time of 2 seconds, the LE2 filter applied to the source, and the detector was set to a 4X objective. Representative scans for each laminate are shown in Fig. 5-29.

Voids were quantified using Fiji ImageJ software [95], using a thresholding method to separate void particle area from the area of fibers and resin. Particles with 30 µm^2 area or higher were counted to avoid interference from image noise after thresholding, corresponding to a void diameter of ∼6 µm, slightly less than the threshold in [96] of 10 µm in diameter. As with the woven CFRP studied earlier in this thesis (see Sec. 4.2), the threshold was decreased from that of the GFRP (see Sec. 4.1) due to improvements in image contrast. Void content was analyzed from 19 cross-section slices from each of the µCT scans at an equidistant spacing from each other among the ∼2000 total slices. The percent of area that is from voids for each of the slices is used to calculate the average and standard error of the specimen void content. Thresholding yielded the results shown in Table 5.11 for void content among the two samples scanned from 19 cross sections.

The MRCC and Extended First Hold cure cycles have imperfect void content, but are successfully under the threshold practiced in the aerospace industry of 1 vol% [83]. However, the three accelerated cure cycles miss by a wide margin. With higher

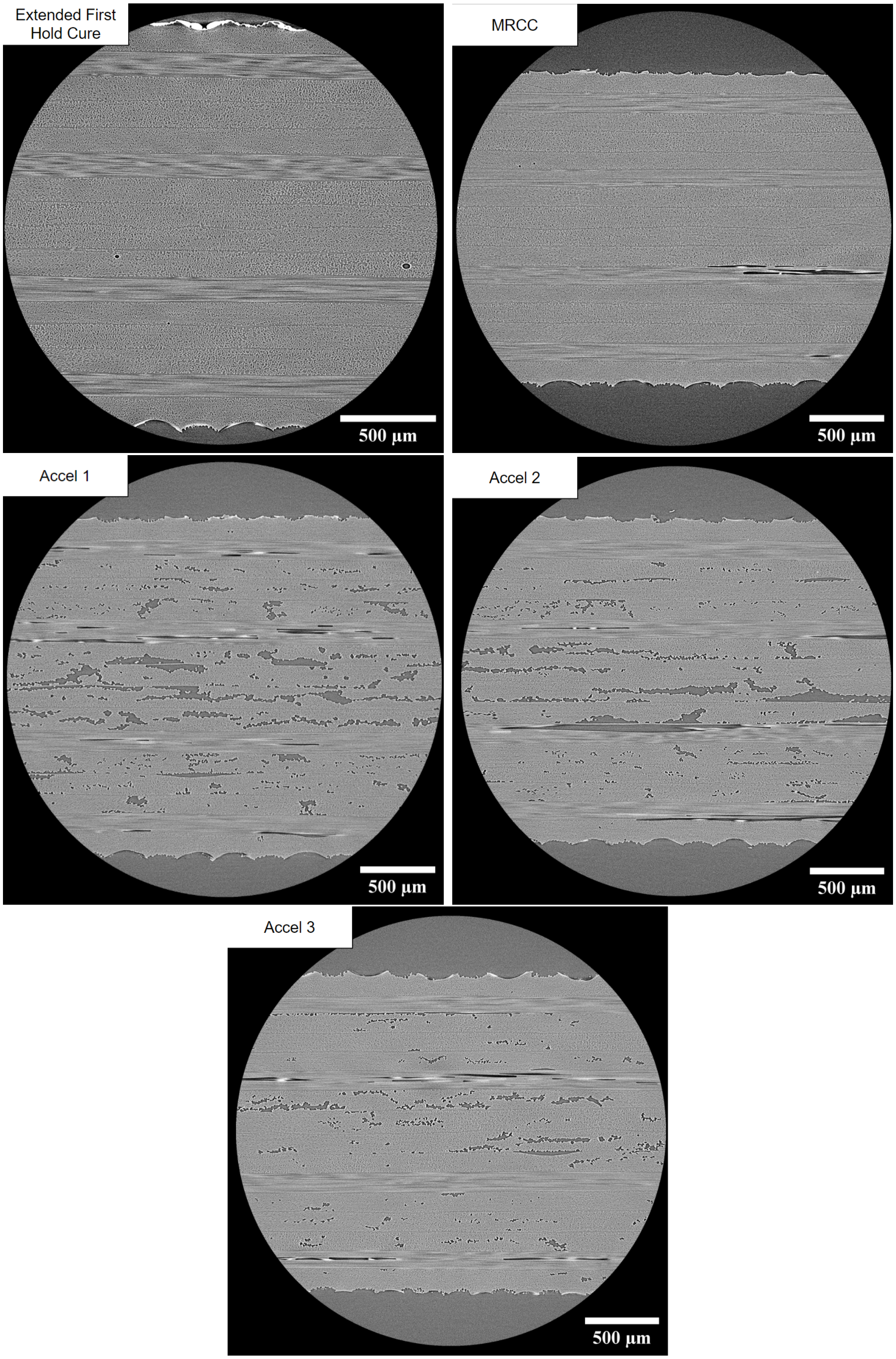

Figure 5-29: Representative µCT images of µCT specimens from each of the cures.

Table 5.11: Measured void content of each OoO curing cycle conducted, using the thresholding method across 19 scans.

Cure Cycle	**Void Content (± Standard Error) [vol%]**
Extended First Hold	0.023 ± 0.002
MRCC	0.076 ± 0.031
Accel 1	9.973 ± 0.245
Accel 2	7.692 ± 0.210
Accel 3	4.316 ± 0.134

ramp rates, it is likely that the NPN is wetted quicker due to the faster drop in resin viscosity, highlighted in the viscosity plots in Fig. 5-24. This is likely causing the flow of air to be constricted too soon, and voids become entrapped as a result.

Differential Scanning Calorimetry

DSC is used to calculate the DoC of each laminate. Samples were taken from a corner of the entire cured laminate, as this is the region that is most susceptible to lower DoC, although the even heating distribution of the tool plates is expected to reduce thermal gradients (further testing is required to measure this). Samples were taken across the entire thickness of the laminate, as the DoC through the thickness has been shown to be the same in previous work [14]. Each DSC run was conducted with aluminum pans (Tzero Hermetic Aluminum Pan) and lids, each weighing roughly 50 mg. Samples were inserted that weighed ∼15-35 mg, ensuring sufficient resin was available for measurement within the fiber-dominant samples. Each sample was subjected to a 5°C/min ramp rate from 40°C to 300°C, based on previous work [14]. Samples were tested using a DSC 2500 (TA Instruments). The heat of reaction is obtained for each of the specimens, and the DoC is calculated using the following formula:

$$DoC = 1 - \left(\frac{\Delta H_{specimen}}{\Delta H_{uncured}} \right) \tag{5.8}$$

where $\Delta H_{uncured}$ corresponds to the heat of reaction of uncured prepreg. 5 uncured AS4/8552 prepreg specimens, 6 MRCC OoO specimens, 4 specimens each for the Extended First Hold, Accel 1, Accel 2, and Accel 3 cure cycles, and 3 specimens for baseline (no NPN) autoclave cured AS4/8552 were tested. The calculated DoCs from DSC curves (Fig. 5-30) are shown in Table 5.12. $\Delta H_{uncured}$ is assumed to be the average value of the prepreg DSC result in the calculation of DoC. It is assumed that the NPN in the laminate does not play a significant role in the DoC calculation, as the mass is negligible compared to the mass of the fibers and resin (total NPN in each sample is roughly on the order of 10^{-2} mg).

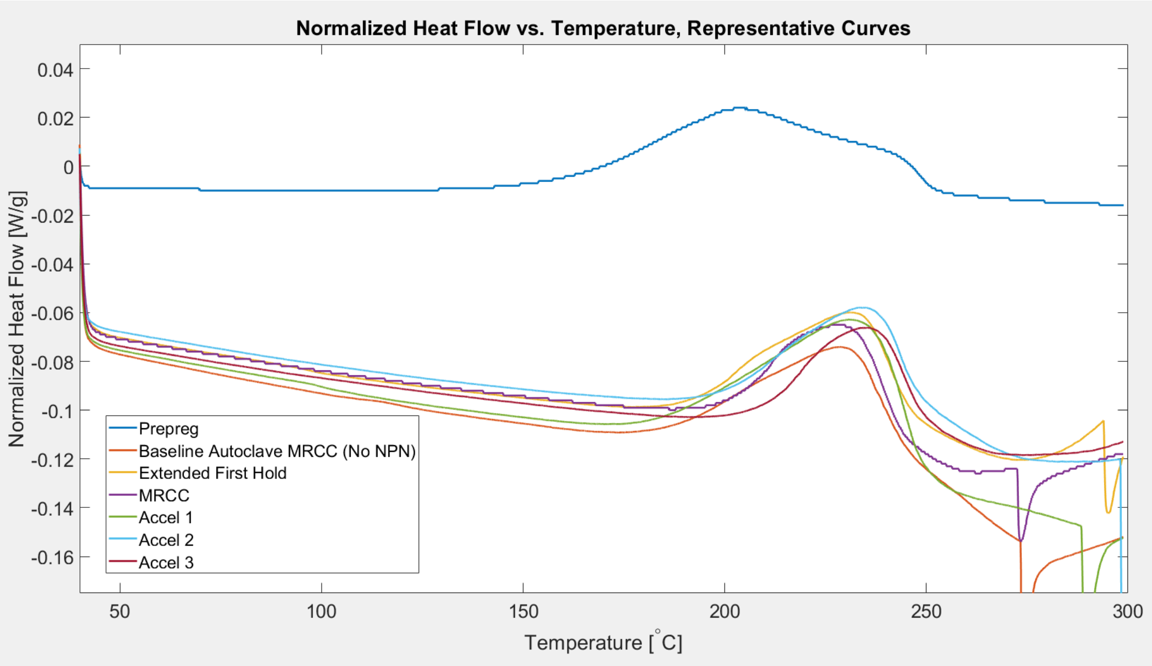

Figure 5-30: Representative DSC curves for each specimen category. Errors were common in the reading of Normalized Heat flow at temperatures above 260°C.

The goal is to obtain a DoC within the range of 90-95% for all cure cycles. However, from the DSC data, it is found that Accelerated Cure 1 and Accelerated Cure 2 are lacking in DoC, as both have significantly lower DoC than the acceptable range. The MRCC cure has no statistically significant difference with the autoclave baseline DoC. The autoclave baseline MRCC also had a poor performance in terms of DoC, pointing to a potential overall underestimate of DoC, which can be due to the remaining shell life of the prepreg or instrument measurement inaccuracy. Accel 3 showed

Table 5.12: Measured heat of reaction and DoC of prepreg, autoclave baseline AS4/8552, and OoO with NPN samples under varying cure cycles, along with the number of samples tested. Note that $\Delta H_{uncured}$ is assumed to be the average value of the prepreg DSC results in the calculation of DoC.

Sample Category	**Heat of Reaction (± Standard Error) [J/g]**	**DoC (± Standard Error) [%]**	**Num. of Samples**
Prepreg	169.399± 4.003	0.00 ± 0.00	5
Baseline Autoclave MRCC (No NPN)	18.967 ± 1.310	88.80 ± 0.77	3
Extended First Hold	21.586 ± 1.227	87.26 ± 0.72	4
MRCC	17.188 ± 2.159	89.85 ± 1.27	6
Accel 1	28.321 ± 1.841	83.28 ± 1.09	4
Accel 2	21.565 ± 1.965	87.26 ± 1.16	4
Accel 3	16.152 ± 0.550	90.47 ± 0.32	4

the highest DoC results, with a DoC that is within the acceptable range (including standard error). The 200°C hold for 36.5 minutes reached an acceptable DoC.

Dynamic Mechanical Analysis

DMA is used to calculate the glass transition temperature T_g of each laminate, as well as to find the storage modulus, loss modulus, and tan delta of each laminate. DMA allows for the comparison of thermomechanical properties to examine the effect of the cure cycles on the properties. Specimens were cut to ∼30 mm x ∼10 mm dimensions and polished using P120, P400, and P1200 sandpaper. 3 samples were used per cure cycle category. A single cantilever clamp was used to acquire data, as samples were subjected to a 50°C to 300°C temperature sweep at a 5°C/min heating rate and a 1 Hz oscillatory load, as recommended by ASTM D7028 [132]. Representative DMA curves for the Extended First Hold, MRCC, Accel 1, Accel 2, and Accel 3 cycles are shown in Fig. 5-31, and T_g, as well as the storage modulus, loss modulus, and tan delta are reported in Table 5.13 and Fig. 5-32. Most observed statistically significant differences between the laminates are between the T_g and Tan Delta of Accelerated Cure 1 with to the rest of the laminates. Accel 3 also has a significantly higher T_g compared to the MRCC cure, pointing to an improvement in the laminate quality.

5.2.4 Short Beam Shear Testing

For SBS, only the Extended First Hold and MRCC cures were tested, as the accelerated cures had a high void content. Specimens were cut and polished to 14 mm x 4.5 mm dimensions, aiming for sufficient length and width of the specimens (6x thickness and 2x thickness, respectively) per the ASTM D2344 standard [133]. SBS testing was conducted with a Zwick Mechanical Tester, with a tool speed of 1 mm/min, a loading nose with a 3 mm radius, and supports with radii of 1.5 mm that were spread apart by 9 mm (4x thickness), adhering to the ASTM D2344 standard. SBS values are shown (see Fig. 5-33, Table 5.14) for the MRCC OoO cure and the Extended First Hold cures that used AS4/8552 with EPN NPN in a quasi-isotropic

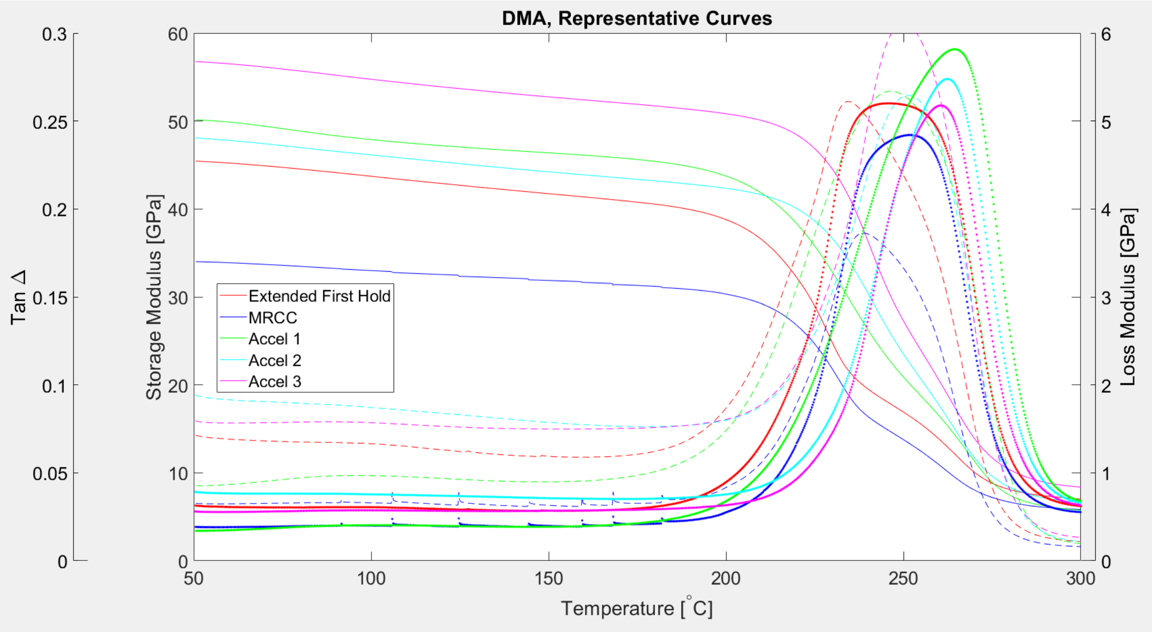

Figure 5-31: Representative DMA curves for each of the laminates tested. Solid lines are storage modulus, dashed lines are loss modulus, and dotted lines are tan delta.

Table 5.13: Measured T_g, storage modulus, loss modulus, and tan delta for the 5 different OoO laminates tested, with 3 samples per laminate.

Sample Category	**T_g (± Standard Error) [°C]**	**Storage Modulus (± Standard Error) [GPa] @ 100°C**	**Loss Modulus (± Standard Error) [GPa] @ 100°C**	**100*$tan\Delta$ (± Standard Error) @ 100°C**
Extended First Hold	216.46 ± 0.35	54.49 ± 5.41	1.15 ± 0.11	2.19 ± 0.44
MRCC	220.54 ± 1.46	44.01 ± 11.23	0.93 ± 0.26	2.09 ± 0.06
Accel 1	210.57 ± 4.77	52.70 ± 2.66	1.00 ± 0.11	1.89 ± 0.14
Accel 2	226.90 ± 3.00	53.13 ± 4.38	1.28 ± 0.23	2.51 ± 0.65
Accel 3	230.76 ± 2.26	55.27 ± 1.33	1.19 ± 0.19	2.16 ± 0.37

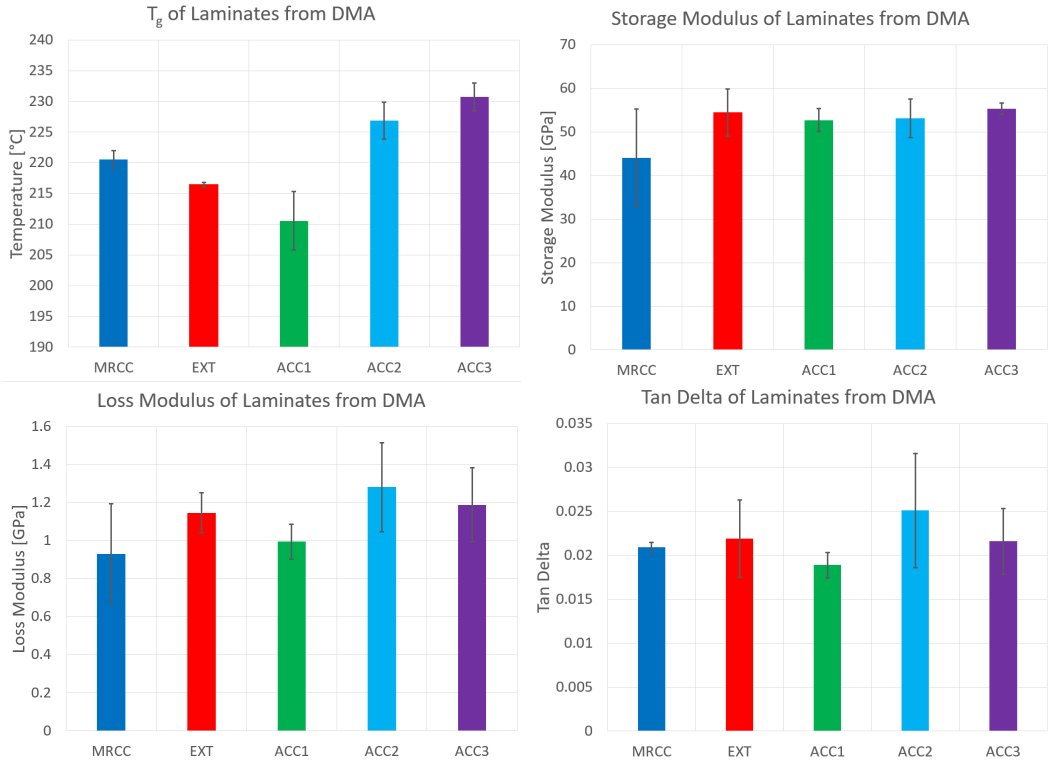
T_g of Laminates from DMA

Storage Modulus of Laminates from DMA

Loss Modulus of Laminates from DMA

Tan Delta of Laminates from DMA

Figure 5-32: DMA values for T_g, as well as storage modulus, loss modulus, and tan delta for all laminates tested at 100°C.

layup sequence ($[0/90/+45/-45]_{2S}$). An autoclave baseline cure from the literature [134] is also included for reference.

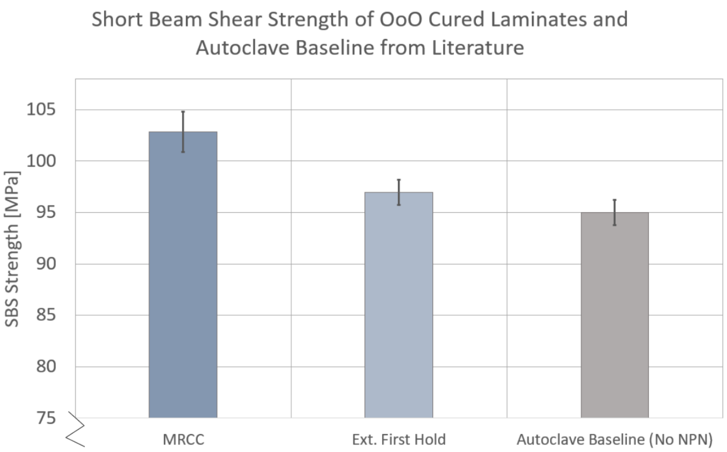

Figure 5-33: SBS strength values for extended first hold and MRCC cured OoO laminates and autoclave baseline from literature [134].

Table 5.14: SBS Strength of tested laminates and autoclave (no NPN) baseline from literature [134], as well as thicknesses across all OoO cured laminates from the same locations as depicted in Fig. 5-28 for reference. Accelerated cures were not tested due to their high void content.

Sample Category	**SBS Strength (± Standard Error) [MPa]**	**Thickness (± Standard Error) [mm]**
Autoclave Baseline [134]	95.0 ± 1.2	–
Extended First Hold	96.97 ± 1.22	2.154 ± 0.006
MRCC	102.87 ± 1.96	2.086 ± 0.008
Accel 1	–	2.196 ± 0.028
Accel 2	–	2.164 ± 0.027
Accel 3	–	2.138 ± 0.023

The results show that the MRCC with OoO cured laminates outperform the Extended First Hold cured laminates by a statistically significant amount. As specimens were found to have failure modes that were nominal, this can be attributed to the difference in DoC, which affects the strength of the material, especially in the resin rich interlaminar region. The Extended First Hold cure was found to have equal strength as an autoclave baseline (with no NPN) of the same material and layup. Furthermore, the MRCC cure was found to have a statistically significant increase of 8.3% in SBS strength compared to an autoclave baseline (with no NPN) from the literature. However, further investigation, including an autoclave baseline using prepreg from the same roll, is required before finding conclusive evidence of any difference in strength between OoO and autoclave laminates.

5.3 Conclusions

5 cure cycles were modeled using ANSYS ACCS, 2 of which were obtained by an optimization scheme in Python using the scipy.optimize library. The predicted viscosity time profiles were calculated using empirical data provided by the literature, and a metric from the literature was used to compare respective cure cycles. Cure cycles were then conducted experimentally, and laminates were tested for quality via µCT, DMA, DSC, and SBS, finding significant differences in the mechanical properties and mostly similarities in the thermal properties. When comparing the model to the experimental data, the most important metric is the DoC. The modeled DoC is shown to generally overestimate the experimental DoC, especially among the accelerated cure cycles, as the 200°C hold changes the DoC at a faster rate compared to the 180°C hold. The model to experimental comparison of DoC is shown in Table 5.15.

This overestimate in DoC can be attributed to the lack of insulation applied on the sides of the laminate in all experimental cures, as well as the model not recognizing natural convection occurring at the sides of the laminate during curing. This can also cause a significant difference in temperature distribution that affects the distribution of DoC across the laminate, although it is unclear by how much at this time. Further analysis is required to fully characterize the OoO system to improve the model fidelity, especially including analysis of the cork tape thermal properties.

Table 5.15: Modeled vs. Experimental DoC for manufactured laminates. Error is calculated from the mid range of the modeled DoC and the average of the experimental DoC. The average error is 5.58 ± 1.57 [%].

Sample Category	**Modeled DoC Range [%]**	**Experimental DoC (± Standard Error) [%]**	**Error [%]**
Extended First Hold	90.37 - 91.28	87.26 ± 0.72	4.08
MRCC	90.33 - 91.24	89.85 ± 1.27	0.93
Accel 1	90.92 - 91.92	83.28 ± 1.09	9.77
Accel 2	94.08 - 94.87	87.26 ± 1.16	8.27
Accel 3	94.46 - 95.24	90.47 ± 0.32	4.84

N_{flow} was not found to correlate to the void content among all cure cycles. However, for groups of cure cycles in a similar time frame (i.e. Accelerated vs. MRCC and Ext. First Hold), void content is found to decrease as N_{flow} increases. To find a correlation among all cure cycles, further investigation is required to adjust for the presence of the NPN, and a redefined coefficient may be more suitable, such as one that has a higher dependence on time. An important finding in the experimental study is the ability to manufacture scaled-up panels with low void contents without the use of a debulk step. The extended first hold cure was done without a debulk step while also producing the highest quality laminate with respect to void content. This is an advantage over OoA based prepregs, which require a debulk step to consolidate the laminate prior to curing. The shortcoming of the extended first hold cure is the lower DoC, which caused issues in the mechanical properties. However, it was found that the temperature profile of Accelerated Cure 3 was able to successfully produce a laminate with the desired DoC in the range of 90-95% with an accelerated second hold. As such, time savings in this study were found in both circumventing the debulk process step, as well as in the second temperature hold in the cure cycle. However, additional considerations must be made to accelerate the first half of the cure cycle due to the presence of the NPN. Further work is required to analyze the acceleration of the first half of the cure cycle in OoA prepregs.

It is recommended for future work that a cure cycle utilizing the first half of the extended first hold cure cycle, up to the second ramp, followed by the second ramp and temperature hold of the cure cycle of Accel 3. This cure cycle may yield a autoclave prepreg VBO with NPN laminate that has low void content without the use of a debulk step, common to OoA prepregs, as well as a DoC high enough to avoid mechanical property degradation due to insufficient curing, although further testing is required.

THIS PAGE INTENTIONALLY LEFT BLANK

Chapter 6

Conclusions and Recommendations

In this thesis, fiber reinforced composite materials (FRPs) fabricated through the prepreg layup process are studied to improve the traditional autoclave curing process. Nanoporous networks (NPNs), when integrated into FRPs, have been shown to enable out-of-autoclave (OoA) manufacturing of autoclave-grade prepregs across a variety of material systems, namely unidirectional GFRPs, woven CFRPs, and unidirectional CFRPs, via vacuum bag-only (VBO) manufacturing. Furthermore, the out-of-oven manufacturing technique is explored and developed further to demonstrate the fidelity of the manufacturing process, and the ability to accelerate the cure cycle used in OoO manufacturing via the robust CNT heating element is explored. A summary of the thesis contributions, as well as avenues for future work, are provided.

6.1 Summary of Thesis Contributions

The following thesis contributions demonstrate the ability of nanomaterials to enable out-of-autoclave and out-of-oven manufacturing of fiber reinforced polymer composites, via both integration within the composite itself, as well as externally as a heating element with negligible thermal mass.

Enabling of autoclave-grade unidirectional GFRP out-of-autoclave manufacturing

It has been shown in this work that GFRP manufacturing by VBO is possible via the use of PI aerogel NPNs, while there is also the possibility for other NPNs (i.e. VA-CNTs, EPNs) to also enable void-free laminate manufacturing in a VBO environment. This was demonstrated through 25.4 mm (1 in.) x 25.4 mm (1 in.) laminates and characterized via SEM and µCT to verify interlaminar void removal using NPNs in unidirectional GFRP.

Demonstration of 40 µm thick PI aerogel layers in the interply of woven CFRP to produce laminates with minimal void content

It has been shown in this work that thinner PI aerogel NPN layers, 40 µm thick instead of previously successful 60 µm thick, are still able to provide the necessary resin wicking characteristics in order to produce woven CFRP laminates with minimal void content (< 0.03 vol%).

Modified manufacturing process of VBO curing of autoclave-grade prepreg woven CFRP with NPN shown to produce laminates with minimal void content

Introduced modifications, including a 3-hour debulk at 60°C, along with temporary heating of plies before placing NPNs, have been shown to produce woven CFRP laminates with minimal void content in a VBO manufacturing process using autoclave-grade prepreg.

Optimization framework for OoO curing developed

An ANSYS ACCS model and accompanying Python script have been developed to allow for cure cycle optimization. The optimization script can accommodate any number of variables via a penalty function (and therefore, any number of CNT heaters in the OoO process), and allows for rapid modification of the ANSYS Transient Thermal analysis through Python code that has been developed.

Framework developed for estimating rheology of resin in AS4/8552 laminates in convective and conductive curing for any given cure cycle

Combining an empirical model [131] with the ANSYS ACCS time history of temperature and DoC data during a cure cycle on an AS4/8552 based composite, the resulting rheology profile over time of the resin within the laminate can be estimated for any cure cycle and/or laminate configuration, within the limits of the empirical data model of 25°C to 250°C. This can be extended to any prepreg material if both the necessary material properties are known for the ANSYS ACCS simulation and an empirical model for the resin has been developed that can be implemented into the ANSYS simulation through a user defined output.

Demonstration of macro-scale minimal void content CFRP laminate OoO manufacturing using autoclave-grade prepreg with EPN NPN and a low aspect ratio heater

152.4 mm (6 in.) x 152.4 mm (6 in.) laminates with unidirectional AS4/8552, an autoclave-grade prepreg, were manufactured via the VBO with NPN OoO process using a single heating element. The DoC of the MRCC cured laminate approaches or is within the acceptable range of 0.90-0.95. Void content was found to be 0.076 vol% for MRCC cured laminates and 0.023 vol% for a modified cure cycle with an extended first hold, both of which were much below 1 vol%, the maximum allowable in the aerospace industry. The set-up developed in this thesis utilizes commercially available insulation and CNT non-woven mats and thin aluminum tooling plates that can be easily modified to fit most shapes, suggesting straightforward implementation in industry, especially given the extensive understanding already developed for autoclave prepregs.

Accelerated second hold in cure cycle for VBO manufacturing of autoclave-prepreg with NPN laminates shown to produce laminates with acceptable DoC

The second hold used in curing autoclave prepreg composite laminates (in this case, AS4/8552 CFRP) of 2 mm thickness had been accelerated to cure to an acceptable DoC using a 200°C hold for 36.5 minutes via the OoO manufacturing process, reducing cure cycle throughput time by 83.5 minutes (32% reduction from fastest MRCC).

Demonstration of CNT Heater with a low aspect ratio to enable heating rates of at least 15°C/min

Via the insulation and power environment, a CNT heater of square dimensions was shown to be capable of heating up the laminate in the OoO environment at a 15°C/min ramp rate, with potential for even higher ramp rates, as the maximum power consumption was not used during the 15°C/min initial ramp of the Accel 2 cure cycle.

PID control shown to enable high accuracy curing of composites under varying cure cycles via OoO curing

PID control was implemented in adherence to the chosen cure cycles, with varying positive ramp rates, as well as low magnitude negative ramp rates (no cooling was implemented in the OoO set-up).

6.2 Recommendations for Future Work

Recommendations for future work are outlined in this section, focusing primarily on material testing, process improvement, and model development.

Mechanical testing of laminates made of autoclave unidirectional GFRP prepreg with NPN and autoclave woven CFRP prepreg with NPN and cured via VBO manufacturing

Having demonstrated void evacuation, the next step in material readiness is to manufacture specimens for mechanical testing, especially SBS and Mode I and II testing, which focus on the strength of the interlaminar region of the laminates. Both unidirectional GFRP and woven CFRP require this next step in validation.

VA-CNTs as NPN for VBO manufactured autoclave-grade GFRP prepreg with NPN

VA-CNTs were found to potentially allow for VBO curing of autoclave GFRP prepreg in the preliminary study, as adjacent plies were found to be void-free in the µCT scan. Manufacturing an all VA-CNT NPN GFRP laminate using VBO pressure is an avenue for future work for the GFRP material.

Thinner PI aerogel NPN for GFRP laminates cured via VBO manufacturing

20 µm PI aerogel was used as an NPN for unidirectional GFRP prepreg laminate void evacuation with successful results. Using a thinner aerogel may reduce the laminate thickness by a significant amount, especially in thicker laminates than those used in this study (8 ply).

Improvement of ANSYS ACCS OoO model fidelity

In the ANSYS ACCS model, a constant DoC and temperature across the length and width is found, as the sides are not prescribed a thermal load. However, from experimental results, major thermal losses are observed that cause the DoC of the model to significantly over-predict the experimental DoC. Modifications to the initial conditions of the model via. adding material elements (i.e. cork tape) allow for conduction between the laminate and adjacent cork tape to be accounted for, which may result in a higher fidelity model. Alternatively, insulation can be applied to the sides of the laminate as an alternative cork dam, and then more insulation can be added to the model with material properties that are known.

Optimization scheme modified to account for resin flow

In this work, optimization considers the cure kinetics and cure cycle throughput. However, resin flow is not accounted for, and cure cycles that produce poor composite quality (i.e. high void content) can be presented as optimal. Considerations of a resin flow coefficient (that can experimentally be shown to correlate to void content) for void removal is an avenue for future work.

Accelerating the first hold of cure cycle with OoA prepreg

Accelerated cure cycles, particularly with an acceleration of the first hold of the cure cycle, did not achieve ideal laminate quality among the autoclave-grade CFRP prepreg laminates with NPN manufactured with the OoO system, as additional considerations must be made in the presence of NPN. However, OoA prepregs can be cured OoO without the use of NPN. Optimizing the first hold of the cure cycle for time, DoC, and resin flow using OoA prepregs is an avenue for future work and investigation.

Using the extended first hold from the extended first hold cycle in conjunction with the accelerated second hold, or a similar variant, as a cure cycle for autoclave-grade prepreg OoO laminates

The extended first hold resulted in the laminate with the lowest void content ($<$ 0.025 vol%) among all the laminates. The second hold of 200°C for 36.5 min from Accelerated Cure 3 showed an acceptable DoC of 90.47 ± 0.32, also the highest among all the laminates. Combining these two halves of the cure cycle into one, or creating a cure cycle with a similar structure, may produce an autoclave-grade AS4/8552 prepreg with NPN laminate with no voids and ideal DoC, which may result in the highest possible material properties of the material system. This cure cycle would be highly efficient, as there is no debulk step, and the second hold is ~25% the time of the MRCC second hold. A cure cycle that requires no debulk may save hours in manufacturing time compared to OoA prepregs.

Appendix A

Optimization Code for Use in ANSYS Mechanical Scripting

The code used in this thesis for cure cycle optimization is included below. Variables to be optimized are adjusted by the user and inserted as inputs via a list of lists containing upper and lower bounds for each input being optimized. Penalty bounds are also set by the user. The code optimizes and writes a text file that logs each run, as well as the input and output parameters. This code is to be ran under the ANSYS Mechanical Cython editor or Python shell. This code will not work using IronPython in ANSYS Mechanical. This code requires a model to already be defined as it was in this thesis, but may be extended a to similar analysis with proper adjustments. A supplementary code for converting the created text file to a CSV file for post processing is included for convenience.

```
"""
ANSYS Mechanical Cure Cycle Optimization Code for OoO process
@author: Steven Serrano, MIT necstlab
"""
import Ansys
from Ansys import Core as acore
import os
from scipy.optimize import minimize, NonlinearConstraint



DOC_global = 1 #do not change
trial_num = 0 #do not change
```

```
Quantity = Ansys.Core.Units.Quantity



#set path for running project, saving text file
setPath = 'C:/Users/steve/Documents/necstlab/ANSYS/'

os.chdir(setPath)
file = open("results_file_LB.txt", "w")
file.close()

#SET PARAMETERS HERE

ramp_1_init = 10 #C/min, ramp rates
ramp_2_init = 10 #C/min
ramp_3 = -5 #C/min
T_init_1 = 131 #C
t_hold_init_1 = 40 #min
T_init_2 = 200 #C, 2nd hold temp
t_hold_init_2 = 35 #min
T_final = 40 #C

time = (T_init_1 - 20)/ramp_1_init + t_hold_init_1 + \
    (T_init_2-T_init_1)/ramp_2_init  + t_hold_init_2 + \
    (T_final - T_init_2)/ramp_3

DOC_desired = 0.95

DOC_lower_bound = 0.945
DOC_higher_bound = 0.955
DOC_pre_gel_min_bound = 0.09
DOC_pre_gel_max_bound = 0.11

initial_inputs = [T_init_1,t_hold_init_2]
bounds_input = [[125,145],[18,50]]

def objective_function(inputs):
    global Quantity
    file = open("results_file_LB.txt","a")
    ramp_1 = ramp_1_init
    ramp_2 = ramp_2_init
    global ramp_3
    global T_final
    global trial_num
    trial_num = trial_num + 1
```

```
    T_1 = inputs[0]
    T_2 = 200
    t_hold_1 = t_hold_init_1
    t_hold_2 = inputs[1]

    ramp_rate_first = ramp_1 #C/min, to optimize
    ramp_rate_second = ramp_2 #C/min, to optimize
    init_temp = 20 #C
    hold_temp_first = T_1 #C
    hold_temp_second = T_2 #C, to optimize
    end_temp = T_final #C
    hold_time_first = t_hold_1 #min
    hold_time_second = t_hold_2 #min, to optimize

    t1 = 0
    t2 = t1 + ((hold_temp_first-init_temp)/ramp_rate_first)*60
    t3 = t2 + hold_time_first*60
    t4 = t3 + ((hold_temp_second-hold_temp_first)/ramp_rate_second)*60
    t5 = t4 + hold_time_second*60
    t6 = t5 + (T_2 - end_temp)/5 * 60
    t7 = t6 + 600

    t1_str = str(t1) + '␣[sec]'
    t2_str = str(t2) + '␣[sec]'
    t3_str = str(t3) + '␣[sec]'
    t4_str = str(t4) + '␣[sec]'
    t5_str = str(t5) + '␣[sec]'
    t6_str = str(t6) + '␣[sec]'
    t7_str = str(t7) + '␣[sec]'

    analysis = Model.Analyses[0]
    settings = analysis.Children[1]

   # analysis.ClearGeneratedData()
    step_1_time = t3
    step_2_time = t5
    step_3_time = t6
    step_4_time = t7

    str1 = str(step_1_time) + '␣[sec]'
    str2 = str(step_2_time) + '␣[sec]'
    str3 = str(step_3_time) + '␣[sec]'
    str4 = str(step_4_time) + '␣[sec]'

    settings.NumberOfSteps = 1
```

```
settings.CurrentStepNumber = 1
settings.StepEndTime = Quantity(str1)
settings.SetAutomaticTimeStepping(1, AutomaticTimeStepping.On)
settings.MaximumTimeStep = Quantity("150 [sec]")
settings.MinimumTimeStep = Quantity("20 [sec]")
settings.InitialTimeStep = Quantity("30 [sec]")

settings.NumberOfSteps = 4
settings.CurrentStepNumber = 4
settings.StepEndTime = Quantity(str4)
settings.SetAutomaticTimeStepping(4, AutomaticTimeStepping.On)
settings.MaximumTimeStep = Quantity("600 [sec]")
settings.MinimumTimeStep = Quantity("20 [sec]")
settings.InitialTimeStep = Quantity("30 [sec]")

settings.CurrentStepNumber = 3
settings.StepEndTime = Quantity(str3)
settings.SetAutomaticTimeStepping(3, AutomaticTimeStepping.On)
settings.MaximumTimeStep = Quantity("600 [sec]")
settings.MinimumTimeStep = Quantity("20 [sec]")
settings.InitialTimeStep = Quantity("30 [sec]")

settings.CurrentStepNumber = 2
settings.StepEndTime = Quantity(str2)
settings.SetAutomaticTimeStepping(2, AutomaticTimeStepping.On)
settings.MaximumTimeStep = Quantity("30 [sec]")
settings.MinimumTimeStep = Quantity("5 [sec]")
settings.InitialTimeStep = Quantity("10 [sec]")

#set cure cycle

temperature = analysis.Children[2]



init_temp_str = str(init_temp) + ' [C]'
hold_1_str = str(hold_temp_first) + ' [C]'
hold_2_str = str(hold_temp_second) + ' [C]'
end_temp_str = str(end_temp) + ' [C]'
temperature.Magnitude.Inputs[0].DiscreteValues = [Quantity("0 [sec]")]
temperature.Magnitude.Output.DiscreteValues = [Quantity("20 [C]")]
temperature.Magnitude.Inputs[0].DiscreteValues=[Quantity(t1_str), \
    Quantity(t2_str),Quantity(t3_str),Quantity(t4_str),Quantity(t5_str),\
    Quantity(t6_str),Quantity(t7_str)]
```

```
temperature.Magnitude.Output.DiscreteValues=[Quantity(init_temp_str),\
    Quantity(hold_1_str),Quantity(hold_1_str),Quantity(hold_2_str),\
    Quantity(hold_2_str),Quantity(end_temp_str),Quantity(end_temp_str)]

#evaluate new time
time = (T_1 - 20)/ramp_1 + t_hold_1 + (T_2-T_1)/ramp_2 + t_hold_2 + \
    (T_final - T_2)/ramp_3

#run analysis
sol = analysis.Solution
sol.Solve()

#get values for cost function and constraints

DOC = sol.Children[2]
DOC.DisplayTime = Quantity("0 [sec]")
sol.EvaluateAllResults()
DOC_min_quant = DOC.Minimum
DOC_min_end = float(DOC_min_quant.ToString())

global DOC_global
DOC_global = DOC_min_end


DOC.DisplayTime = Quantity(t3_str)
sol.EvaluateAllResults()
DOC_max_ramp_up_quant = DOC.Maximum
DOC_max_ramp_up = float(DOC_max_ramp_up_quant.ToString())


DOC.Activate()

global DOC_lower_bound
global DOC_higher_bound

penalty_1 = 0
penalty_2 = 0
if DOC_min_end > DOC_higher_bound or DOC_min_end < DOC_lower_bound:
    penalty_1 = 1000
    if DOC_min_end < DOC_lower_bound:
        penalty_1 = penalty_1 - 2*t_hold_2
if DOC_max_ramp_up > DOC_pre_gel_max_bound or\
    DOC_max_ramp_up < DOC_pre_gel_min_bound:
    penalty_2 = 1000
    if DOC_max_ramp_up > DOC_pre_gel_max_bound:
```

```
            penalty_2 = penalty_2 + 1.5*T_1

    global DOC_desired

    obj_fxn_1 = time -T_1 + 500*abs(DOC_max_ramp_up - 0.10) + \
        50*abs(DOC_min_end - DOC_desired) + penalty_1 + penalty_2


    file.write("\n" +"Trial␣#:␣" + str(trial_num) + "\n" + "ramp_1:␣=␣" +\
        str(ramp_1) + ",␣ramp_2:␣=␣" + str(ramp_2) + ",␣T_1␣=␣" + str(T_1) +\
        ",␣t_hold_1␣=␣" + str(t_hold_1) + ",␣T_2␣=␣" + str(T_2) +\
        ",␣t_hold_2␣=␣" + str(t_hold_2) + "\n" + "Time␣=␣" + str(time) +\
        ",␣DOC␣=␣" + str(DOC_min_end) + ",␣DOC_t3␣=␣" + str(DOC_max_ramp_up)+\
        "\n" + "Objective␣Function␣=␣" + str(obj_fxn_1) +  "\n")
    file.close()


    return obj_fxn_1


#extra constraint function on DoC, but not necessary
def constraint_function(x):
    global DOC_global
    global DOC_lower_bound
    global DOC_upper_bound
    DOC = DOC_global

    if (DOC - DOC_lower_bound) < 0 or (DOC - DOC_higher_bound) > 0:
        return -1
    else:
        return 1

nonlinear_constraint = NonlinearConstraint(constraint_function, lb=0, ub=None)

result = minimize(objective_function,initial_inputs,method = 'L-BFGS-B',\
    constraints = nonlinear_constraint,bounds = bounds_input, tol = 1e-7,\
    options = {'eps':0.1}) # options ={'eps':0.1})# tol = 1e-3) #
result_array = result.x
ramp_1 = ramp_1_init
ramp_2 = ramp_2_init
T_1 = result_array[0]
T_2 = 200
t_hold_1 = 20
t_hold_2 = result_array[1]
file = open("results_file_LB.txt","a")
```

```
file.write("\n" +"\n" + "————————OPTIMAL␣PARAMETERS————————" + "\n" +\
    "ramp_1:␣=␣" + str(ramp_1) + "ramp_2:␣=␣" + str(ramp_2) + ",␣T_1␣=␣" +\
    str(T_1) + ",␣t_hold_1␣=␣" + str(t_hold_1) + ",␣T_2␣=␣" + str(T_2) +\
    ",␣t_hold_2␣=␣" + str(t_hold_2) + "\n")
file.close()
```

THIS PAGE INTENTIONALLY LEFT BLANK

Appendix B

Supplementary Code for Text File to CSV Conversion

This code supplements the main optimization code by converting the created text file to CSV containing each of the parameters for post-processing.

```
"""
@author: Steven Serrano, MIT necstlab
"""

import re
import os

setPath = ’C:/Users/steve/Documents/necstlab/’

os.chdir(setPath)
file = open("results_file_TO_CSV.txt", "r")
string = file.read()
file.close()

string2 = re.sub(":␣(\d+)","",string)
string3 = re.sub("_(\d+)","",string2)
string4 = re.sub("[^=␣0-9|.|\n|-]","",string3)
string5 = re.sub("\n␣=", "␣=",string4)
string6 = re.sub("\n␣␣=", "␣=",string5)
string7 = re.sub("\n␣,␣","\n",string6)
string8 = re.sub("=",",",string7)
string9 = re.sub("␣","",string8)
string10 = re.sub("\n\n\n","\n",string9)
```

```
string11 = re.sub("\n\n","\n",string10)
string12 = re.sub("———————————————",""",string11)
string13 = re.sub("\n,","\n",string12)
string14 = string13[1:-1]

text_file = open("results_file_TO_CSV.txt", "w")
n = text_file.write(string14)
text_file.close()
```

Bibliography

[1] Bradley A. Newcomb. Processing, structure, and properties of carbon fibers. *Composites Part A: Applied Science and Manufacturing*, 91:262–282, 2016.

[2] Larissa Gorbatikh, Brian L Wardle, and Stepan V Lomov. Hierarchical lightweight composite materials for structural applications. *Mrs Bulletin*, 41(9):672–677, 2016.

[3] Michel Biron. *Thermosets and composites: material selection, applications, manufacturing and cost analysis*, pages 8–12. Elsevier, 2013.

[4] Michael F. Ashby. *Materials selection in mechanical design*, page 57–58. Elsevier, 2004.

[5] Carl T Herakovich. Mechanics of composites: a historical review. *Mechanics Research Communications*, 41:1–20, 2012.

[6] FC Campbell. Introduction to composite materials. *Structural composite materials*, 1:1–29, 2010.

[7] F.C. Campbell. Chapter 7 - polymer matrix composites. In *Manufacturing Technology for Aerospace Structural Materials*, pages 273–368. Elsevier Science, Oxford, 2006.

[8] L. C. Hollaway. The evolution of and the way forward for advanced polymer composites in the civil infrastructure. *Construction and Building Materials*, 17(6-7):365–378, 2003.

[9] P. Beardmore. Composite structures for automobiles. *Composite structures*, 5(3):163–176, 1986.

[10] M-S Scholz, Jamie P Blanchfield, LD Bloom, Broderick H Coburn, M Elkington, Jonathan D Fuller, Mark E Gilbert, Salah A Muflahi, MF Pernice, Steven I Rae, et al. The use of composite materials in modern orthopaedic medicine and prosthetic devices: A review. *Composites Science and Technology*, 71(16):1791–1803, 2011.

[11] A Lewis. Making composite repairs to the 787. *Aero*, 56:04–13, 2014.

[12] Airbus. FAST (Flight Airworthiness Support Technology)—special edition A350XWB. *Airbus Technical Magazine*, 2013.

[13] J. Schlimbach and A. Ogale. 14 - out-of-autoclave curing process in polymer matrix composites. In Suresh G. Advani and Kuang-Ting Hsiao, editors, *Manufacturing Techniques for Polymer Matrix Composites (PMCs)*, Woodhead Publishing Series in Composites Science and Engineering, pages 435–480. Woodhead Publishing, 2012.

[14] Jeonyoon Lee, Xinchen Ni, Frederick Daso, Xianghui Xiao, Dale King, Jose Sánchez Gómez, Tamara Blanco Varela, Seth S. Kessler, and Brian L. Wardle. Advanced carbon fiber composite out-of-autoclave laminate manufacture via nanostructured out-of-oven conductive curing. *Composites Science and Technology*, 166:150–159, 2018. Carbon nanotube composites for structural applications.

[15] T. Centea, L.K. Grunenfelder, and S.R. Nutt. A review of out-of-autoclave prepregs – material properties, process phenomena, and manufacturing considerations. *Composites Part A: Applied Science and Manufacturing*, 70:132–154, 2015.

[16] Dilmurat Abliz, Yugang Duan, Leif Steuernagel, Lei Xie, Dichen Li, and Gerhard Ziegmann. Curing methods for advanced polymer composites - a review. *Polymers and Polymer Composites*, 21(6):341–348, July 2013.

[17] Peng Liu, Zeng Fan, Anastasiia Mikhalchan, Thang Q Tran, Daniel Jewell, Hai M Duong, and Amy M Marconnet. Continuous carbon nanotube-based fibers and films for applications requiring enhanced heat dissipation. *ACS applied materials & interfaces*, 8(27):17461–17471, 2016.

[18] Satyaprakash Sahoo, Venkateswara Rao Chitturi, Radhe Agarwal, Jin-Wu Jiang, and Ram S Katiyar. Thermal conductivity of freestanding single wall carbon nanotube sheet by raman spectroscopy. *ACS applied materials & interfaces*, 6(22):19958–19965, 2014.

[19] Bartolomé Mas, Juan P Fernández-Blázquez, Jonathan Duval, Humphrey Bunyan, and Juan J Vilatela. Thermoset curing through joule heating of nanocarbons for composite manufacture, repair and soldering. *Carbon*, 63:523–529, 2013.

[20] Bogumiła Kumanek and Dawid Janas. Thermal conductivity of carbon nanotube networks: A review. *Journal of materials science*, 54(10):7397–7427, 2019.

[21] Jeonyoon Lee, Itai Y Stein, Mackenzie E Devoe, Diana J Lewis, Noa Lachman, Seth S Kessler, Samuel T Buschhorn, and Brian L Wardle. Impact of carbon nanotube length on electron transport in aligned carbon nanotube networks. *Applied Physics Letters*, 106(5):053110, 2015.

[22] Jeonyoon Lee, Itai Y Stein, Erica F Antunes, Seth S Kessler, and Brian L Wardle. Out-of-oven curing of polymeric composites via resistive microheaters comprised of aligned carbon nanotube networks. In *Twentieth International Conference On Composite Materials (ICCM20)*, 2015.

[23] Ling Zhang, Guang Zhang, Changhong Liu, and Shoushan Fan. High-density carbon nanotube buckypapers with superior transport and mechanical properties. *Nano letters*, 12(9):4848–4852, 2012.

[24] V Meunier, AG Souza Filho, EB Barros, and MS Dresselhaus. Physical properties of low-dimensional s p 2-based carbon nanostructures. *Reviews of Modern Physics*, 88(2):025005, 2016.

[25] TW Ebbesen, HJ Lezec, H Hiura, JW Bennett, HF Ghaemi, and T Thio. Electrical conductivity of individual carbon nanotubes. *Nature*, 382(6586):54–56, 1996.

[26] Xiaochen Li, Frederick Daso, Jeonyoon Lee, Joe Spangler, Jean-Philippe Canart, Mike Kinsella, and Brian L. Wardle. Consolidation of aerospace-grade high-temperature thermoplastic carbon fiber composites via nano-engineered electrothermal heating. *Composites Part B: Engineering*, 262:110814, 2023.

[27] Frederick Daso, Jeonyoon Lee, Tomasz Garstka, Alan McMillan, and Brian L Wardle. Cure cycle acceleration via nano-driven thermal processing of out-of-autoclave thermosetting composites. In *Twenty-second International Conference On Composite Materials (ICCM22)*, 2019.

[28] Jeonyoon Lee, Seth S Kessler, and Brian L Wardle. Void-free layered polymeric architectures via capillary-action of nanoporous films. *Advanced Materials Interfaces*, 7(4):1901427, 2020.

[29] Jingyao Dai, Alisa Webb, Jeonyoon Lee, Lauren Randaccio, Justin Griffin, Steven A. Steiner, and Brian L. Wardle. Out of autoclave manufacturing of void-free woven aerospace-grade carbon fiber reinforced plastic composite laminates using capillary effects of aerogel nanoporous networks. In *AIAA SCITECH 2023 Forum*, page 0516, 2023.

[30] Travis J. Hank, Jeonyoon Lee, Shannon Cassady, Seth Kessler, Stephen Steiner, and Brian L. Wardle. Void-free vacuum-bag-only composite manufacturing with autoclave-grade prepreg using capillary effects of polymer electrospun nanofibers and aerogel nanoporous networks. In *AIAA SCITECH 2022 Forum*, page 1094, 2022.

[31] Dipen K. Rajak, Pratiksha H. Wagh, and Emanoil Linul. Manufacturing technologies of carbon/glass fiber-reinforced polymer composites and their properties: A review. *Polymers*, 13(21), 2021.

[32] Flake C Campbell Jr. *Manufacturing technology for aerospace structural materials*. Elsevier, 2011.

[33] Charles E Harris. *An assessment of the state-of-the-art in the design and manufacturing of large composite structures for aerospace vehicles*. National Aeronautics and Space Administration, Langley Research Center, 2001.

[34] P. Hubert, G. Fernlund, and A. Poursartip. 13 - Autoclave processing for composites. In Suresh G. Advani and Kuang-Ting Hsiao, editors, *Manufacturing Techniques for Polymer Matrix Composites (PMCs)*, Woodhead Publishing Series in Composites Science and Engineering, pages 414–434. Woodhead Publishing, 2012.

[35] Qing Wang, Lingyun Wang, Weidong Zhu, Qiang Xu, and Yinglin Ke. Design optimization of molds for autoclave process of composite manufacturing. *Journal of reinforced plastics and composites*, 36(21):1564–1576, 2017.

[36] NEJ Kluge, TS Lundström, Anna-Lena Ljung, Lars-Göran Westerberg, and Tony Nyman. An experimental study of temperature distribution in an autoclave. *Journal of reinforced plastics and composites*, 35(7):566–578, 2016.

[37] S.G. Advani and K.-T. Hsiao. 1 - introduction to composites and manufacturing processes. In Suresh G. Advani and Kuang-Ting Hsiao, editors, *Manufacturing Techniques for Polymer Matrix Composites (PMCs)*, Woodhead Publishing Series in Composites Science and Engineering, pages 1–12. Woodhead Publishing, 2012.

[38] James K Sutter, W Scott Kenner, Larry Pelham, Sandi G Miller, Danel L Polis, Chaitra Nailadi, Thomas J Zimmerman, Richard D Lort, Tan-Hung Hou, Derek J Quade, et al. Comparison of autoclave and out-of-autoclave composites. In *SAMPE 2010 Technical Conference*, number E-17964, 2010.

[39] James Kratz, Kevin Hsiao, Goran Fernlund, and Pascal Hubert. Thermal models for mtm45-1 and cycom 5320 out-of-autoclave prepreg resins. *Journal of Composite Materials*, 47(3):341–352, 2013.

[40] T Centea and P Hubert. Measuring the impregnation of an out-of-autoclave prepreg by micro-ct. *Composites Science and Technology*, 71(5):593–599, 2011.

[41] S Thomas, C Bongiovanni, and SR Nutt. In situ estimation of through-thickness resin flow using ultrasound. *Composites Science and Technology*, 68(15-16):3093–3098, 2008.

[42] Rahul Harshe. A review on advanced out-of-autoclave composites processing. *Journal of the Indian Institute of Science*, 95(3):207–220, 2015.

[43] Pascal Hubert, Timotei Centea, Lessa Grunefelder, Steven Nutt, James Kratz, and Arthur Lévy. Out-of-Autoclave Prepreg Processing. In *Comprehensive Composite Materials II*, volume 2, pages 63–94. Elsevier, 2018.

[44] Christian Decker. Kinetic study and new applications of uv radiation curing. *Macromolecular Rapid Communications*, 23(18):1067–1093, 2002.

[45] Ajit Singh. Radiation processing of carbon fibre-reinforced advanced composites. *Nuclear Instruments and Methods in Physics Research Section B: Beam Interactions with Materials and Atoms*, 185(1):50–54, 2001.

[46] C Dispenza, S Alessi, and G Spadaro. Carbon fiber composites cured by γ-radiation-induced polymerization of an epoxy resin matrix. *Advances in Polymer Technology: Journal of the Polymer Processing Institute*, 27(3):163–171, 2008.

[47] Giuseppe Spadaro, Sabina Alessi, and Clelia Dispenza. Ionizing radiation-induced crosslinking and degradation of polymers. *Applications of ionizing radiation in materials processing*, 1:167–182, 2017.

[48] Grażyna Przybytniak, Andrzej Nowicki, Krzysztof Mirkowski, and Leszek Stobiński. Gamma-rays initiated cationic polymerization of epoxy resins and their carbon nanotubes composites. *Radiation Physics and Chemistry*, 121:16–22, 2016.

[49] Vincent J. Lopata, Chris B. Saunders, Ajit Singh, Christopher J. Janke, George E. Wrenn, and Stephen J. Havens. Electron-beam-curable epoxy resins for the manufacture of high-performance composites. *Radiation Physics and Chemistry*, 56(4):405–415, 1999.

[50] Xavier Coqueret, Mickael Krzeminski, Philippe Ponsaud, and Brigitte Defoort. Recent advances in electron-beam curing of carbon fiber-reinforced composites. *Radiation Physics and Chemistry*, 78(7-8):557–561, 2009.

[51] S.W. Lye and F.Y.C Boey. Pc-based monitoring and control system for microwave curing of polymer composites. *Materials and Manufacturing Processes*, 9(5):851–868, 1994.

[52] Yiben Zhang, Lingyu Sun, Lijun Li, and Junlei Wei. Effects of strain rate and high temperature environment on the mechanical performance of carbon fiber reinforced thermoplastic composites fabricated by hot press molding. *Composites Part A: Applied Science and Manufacturing*, 134:105905, 2020.

[53] Thomas Bayerl, Miro Duhovic, Peter Mitschang, and Debes Bhattacharyya. The heating of polymer composites by electromagnetic induction – a review. *Composites Part A: Applied Science and Manufacturing*, 57:27–40, 2014.

[54] Christian J Yungwirth, Eric D Wetzel, and James M Sands. Induction curing of a phase-toughened adhesive. Technical report, ARMY RESEARCH LAB ABERDEEN PROVING GROUND MD, 2003.

[55] Junmo Kang, Hyeongkeun Kim, Keun Soo Kim, Seoung-Ki Lee, Sukang Bae, Jong-Hyun Ahn, Young-Jin Kim, Jae-Boong Choi, and Byung Hee Hong. High-performance graphene-based transparent flexible heaters. *Nano letters*, 11(12):5154–5158, 2011.

[56] Sophie Sorel, Daniel Bellet, and Jonathan N Coleman. Relationship between material properties and transparent heater performance for both bulk-like and percolative nanostructured networks. *ACS nano*, 8(5):4805–4814, 2014.

[57] Y-H Yoon, J-W Song, Duckjong Kim, Joondong Kim, J-K Park, S-K Oh, and C-S Han. Transparent film heater using single-walled carbon nanotubes. *Advanced Materials*, 19(23):4284–4287, 2007.

[58] Zi Ping Wu and Jian Nong Wang. Preparation of large-area double-walled carbon nanotube films and application as film heater. *Physica E: Low-dimensional Systems and Nanostructures*, 42(1):77–81, 2009.

[59] Duckjong Kim, Hyun-Chang Lee, Ju Yeon Woo, and Chang-Soo Han. Thermal behavior of transparent film heaters made of single-walled carbon nanotubes. *The Journal of Physical Chemistry C*, 114(13):5817–5821, 2010.

[60] Hoon-Sik Jang, Sang Koo Jeon, and Seung Hoon Nahm. The manufacture of a transparent film heater by spinning multi-walled carbon nanotubes. *Carbon*, 49(1):111–116, 2011.

[61] Song-Lin Jia, Hong-Zhang Geng, Luda Wang, Ying Tian, Chun-Xia Xu, Pei-Pei Shi, Ze-Zeng Gu, Xue-Shuang Yuan, Li-Chao Jing, Zhi-Ying Guo, et al. Carbon nanotube-based flexible electrothermal film heaters with a high heating rate. *Royal Society open science*, 5(6):172072, 2018.

[62] Bing Zhou, Xueqing Han, Liang Li, Yuezhan Feng, Tao Fang, Guoqiang Zheng, Bo Wang, Kun Dai, Chuntai Liu, and Changyu Shen. Ultrathin, flexible transparent joule heater with fast response time based on single-walled carbon nanotubes/poly(vinyl alcohol) film. *Composites Science and Technology*, 183:107796, 2019.

[63] Junjie Ma, Huilei Jiang, Shujie Hu, Jinwei Song, Xuanhe Zhang, Te Hu, Huijian Ye, and Lixin Xu. Ultraviolet light crosslinked graphene/multi-walled carbon nanotube hybrid films for highly robust, efficient and flexible electrothermal heaters. *Composites Science and Technology*, 221:109183, 2022.

[64] P D Mangalgiri. Composite materials for aerospace applications. *Bulletin of Materials Science*, 22(3):657–664, May 1999.

[65] Brian G. Falzon and Robert S. Pierce. *Thermosetting Composite Materials in Aerostructures*, pages 57–86. Springer International Publishing, Cham, 2020.

[66] A.T. Marques. 7 - fibrous materials reinforced composites production techniques. In R. Fangueiro, editor, *Fibrous and Composite Materials for Civil Engineering Applications*, Woodhead Publishing Series in Textiles, pages 191–215. Woodhead Publishing, 2011.

[67] Michel Biron. *Thermoplastics and thermoplastic composites.* William Andrew, 2018.

[68] Zhongliang Cao, Mingjun Dong, Kailei Liu, and Hongya Fu. Temperature field in the heat transfer process of PEEK thermoplastic composite fiber placement. *Materials*, 13(19):4417, October 2020.

[69] Jeonyoon Lee, Itai Y Stein, Seth S Kessler, and Brian L Wardle. Aligned carbon nanotube film enables thermally induced state transformations in layered polymeric materials. *ACS applied materials & interfaces*, 7(16):8900–8905, 2015.

[70] Hexcel. Hexply 8552 Product Data Sheet. Downloaded June 19, 2023 from https://www.hexcel.com/Resources/DataSheets/Prepreg.

[71] S. Hernández, F. Sket, J.M. Molina-Aldareguı´a, C. González, and J. LLorca. Effect of curing cycle on void distribution and interlaminar shear strength in polymer-matrix composites. *Composites Science and Technology*, 71(10):1331–1341, 2011.

[72] S Hernández, Federico Sket, C González, and J Llorca. Optimization of curing cycle in carbon fiber-reinforced laminates: void distribution and mechanical properties. *Composites Science and Technology*, 85:73–82, 2013.

[73] Anqi Dong, Yan Zhao, Xinqing Zhao, and Qiyong Yu. Cure cycle optimization of rapidly cured out-of-autoclave composites. *Materials*, 11(3):421, 2018.

[74] Sérgio Frascino Müller de Almeida and Zabulon dos Santos Nogueira Neto. Effect of void content on the strength of composite laminates. *Composite Structures*, 28(2):139–148, 1994.

[75] Mikhail R Stukan, Patrice Ligneul, John P Crawshaw, and Edo S Boek. Spontaneous imbibition in nanopores of different roughness and wettability. *Langmuir*, 26(16):13342–13352, 2010.

[76] Mingfu Zhang, Priyanka Dobriyal, Jiun-Tai Chen, Thomas P Russell, Jessica Olmo, and Aurora Merry. Wetting transition in cylindrical alumina nanopores with polymer melts. *Nano letters*, 6(5):1075–1079, 2006.

[77] Kyusoon Shin, Sergei Obukhov, Jiun-Tai Chen, June Huh, Yoontae Hwang, Soonchun Mok, Priyanka Dobriyal, Pappannan Thiyagarajan, and Thomas P Russell. Enhanced mobility of confined polymers. *Nature materials*, 6(12):961–965, 2007.

[78] DI Dimitrov, A Milchev, and K Binder. Capillary rise in nanopores: molecular dynamics evidence for the lucas-washburn equation. *Physical review letters*, 99(5):054501, 2007.

[79] Jianchao Cai, Edmund Perfect, Chu-Lin Cheng, and Xiangyun Hu. Generalized modeling of spontaneous imbibition based on hagen–poiseuille flow in tortuous capillaries with variably shaped apertures. *Langmuir*, 30(18):5142–5151, 2014.

[80] Alisa Webb, Jingyao Dai, Kwasi Asamoah-Addo, Justin Griffin, Stephen A. Steiner, and Brian L Wardle. Fundamental study of nanoporous network (NPN) characteristics enabling out of autoclave manufacturing of aerospace-grade composite laminates. In *Twenty-third International Conference On Composite Materials (ICCM23)*, 2023.

[81] LMAT LTD (2016). ACCS User Guide. Accessed June 20, 2023 from https://storage.ansys.com/mbu-assets/accs/v211/ug/index.html.

[82] SR Ghiorse. Effect of void content on the mechanical properties of carbon/epoxy laminates. *SAMPE quarterly*, 24(2):54–59, 1993.

[83] Ling Liu, Bo-Ming Zhang, Dian-Fu Wang, and Zhan-Jun Wu. Effects of cure cycles on void content and mechanical properties of composite laminates. *Composite structures*, 73(3):303–309, 2006.

[84] Priyadarsini Morampudi, Kiran Kumar Namala, Yeshwanth Kumar Gajjela, Majjiga Barath, and Ganaparthy Prudhvi. Review on glass fiber reinforced polymer composites. *Materials Today: Proceedings*, 43:314–319, 2021.

[85] TP Sathishkumar, S Satheeshkumar, and Jesuarockiam Naveen. Glass fiber-reinforced polymer composites–a review. *Journal of reinforced plastics and composites*, 33(13):1258–1275, 2014.

[86] Hua Zhu and SK Khanna. A novel transparent glass fiber-reinforced polymer composite interlayer for blast-resistant windows. *Journal of Engineering Materials and Technology*, 138(3):031007, 2016.

[87] Hexcel. Hexply 913 Product Data Sheet. Downloaded July 30, 2023 from https://www.hexcel.com/Resources/DataSheets/Prepreg.

[88] Palak B. Patel. Experimental nanoengineering of multifunctionality into an advanced composite laminate, 2022.

[89] R Guzman De Villoria, P Hallander, L Ydrefors, P Nordin, and BL Wardle. In-plane strength enhancement of laminated composites via aligned carbon nanotube interlaminar reinforcement. *Composites Science and Technology*, 133:33–39, 2016.

[90] Enrique J Garcia, Brian L Wardle, and A John Hart. Joining prepreg composite interfaces with aligned carbon nanotubes. *Composites Part A: Applied Science and Manufacturing*, 39(6):1065–1070, 2008.

[91] Collaboration results in interleaving veils for composite toughening. *NZ Manufacturer*, page 8, Jul 2019.

[92] Xinchen Ni, Carolina Furtado, Nathan K Fritz, Reed Kopp, Pedro P Camanho, and Brian L Wardle. Interlaminar to intralaminar mode I and II crack bifurcation due to aligned carbon nanotube reinforcement of aerospace-grade advanced composites. *Composites Science and Technology*, 190:108014, 2020.

[93] Mahoor Mehdikhani, Larissa Gorbatikh, Ignaas Verpoest, and Stepan V Lomov. Voids in fiber-reinforced polymer composites: A review on their formation, characteristics, and effects on mechanical performance. *Journal of Composite Materials*, 53(12):1579–1669, 2019.

[94] Nathan K Fritz, Reed Kopp, Abigail K Nason, Xinchen Ni, Jeonyoon Lee, Itai Y Stein, Estelle Kalfon-Cohen, Ian Sinclair, S Mark Spearing, Pedro P Camanho, et al. New interlaminar features and void distributions in advanced aerospace-grade composites revealed via automated algorithms using micro-computed tomography. *Composites Science and Technology*, 193:108132, 2020.

[95] Caroline A Schneider, Wayne S Rasband, and Kevin W Eliceiri. NIH Image to ImageJ: 25 years of image analysis. *Nature methods*, 9(7):671–675, 2012.

[96] S Paciornik, , and JRM d'Almeida. Measurement of void content and distribution in composite materials through digital microscopy. *Journal of Composite Materials*, 43(2):101–112, 2009.

[97] FYC Boey and SW Lye. Void reduction in autoclave processing of thermoset composites: Part 1: High pressure effects on void reduction. *Composites*, 23(4):261–265, 1992.

[98] Jeonyoon Lee. *Nanomaterial-enabled manufacturing for next-generation multifunctional advanced composite prepreg laminate architectures*. PhD thesis, Massachusetts Institute of Technology, 2018.

[99] Singiresu S Rao. *Engineering optimization: theory and practice*. John Wiley & Sons, 2019.

[100] Yunfei Cui, Zhiqiang Geng, Qunxiong Zhu, and Yongming Han. Review: Multi-objective optimization methods and application in energy saving. *Energy*, 125:681–704, 2017.

[101] Ajay Shrestha and Ausif Mahmood. Review of deep learning algorithms and architectures. *IEEE access*, 7:53040–53065, 2019.

[102] S. Koussios, O.K. Bergsma, and A. Beukers. Filament winding: kinematics, collision control and process optimisation through application of dynamic programming. *Composites Part A: Applied Science and Manufacturing*, 37(11):2088–2104, 2006.

[103] E Wilson, CL Karr, and S Messimer. Genetic algorithm optimization of a filament winding process modeled in witness. *Practical Applications of Computational Intelligence Techniques*, pages 223–239, 2001.

[104] M. Kaufmann, D. Zenkert, and M. Åkermo. Cost/weight optimization of composite prepreg structures for best draping strategy. *Composites Part A: Applied Science and Manufacturing*, 41(4):464–472, 2010.

[105] Shuai Chen, Lee T Harper, Andreas Endruweit, and Nicholas A Warrior. Optimisation of forming process for highly drapeable fabrics. In *20th international conference on composite materials*, 2015.

[106] S. Chen, O.P.L. McGregor, L.T. Harper, A. Endruweit, and N.A. Warrior. Optimisation of local in-plane constraining forces in double diaphragm forming. *Composite Structures*, 201:570–581, 2018.

[107] J. Wang, P. Simacek, and S.G. Advani. Use of centroidal voronoi diagram to find optimal gate locations to minimize mold filling time in resin transfer molding. *Composites Part A: Applied Science and Manufacturing*, 87:243–255, 2016.

[108] Tomonaga Okabe, Yutaka Oya, Go Yamamoto, Junki Sato, Tsubasa Matsumiya, Ryosuke Matsuzaki, Shigeki Yashiro, and Shigeru Obayashi. Multi-objective optimization for resin transfer molding process. *Composites Part A: Applied Science and Manufacturing*, 92:1–9, 2017.

[109] Mehdy Vafayan, Mir Hamid Reza Ghoreishy, Hossein Abedini, and Mohammad Hossein Beheshty. Development of an optimized thermal cure cycle for a complex-shape composite part using a coupled finite element/genetic algorithm technique. *Iranian Polymer Journal*, 24:459–469, 2015.

[110] PH Shah, VA Halls, JQ Zheng, and RC Batra. Optimal cure cycle parameters for minimizing residual stresses in fiber-reinforced polymer composite laminates. *Journal of Composite Materials*, 52(6):773–792, 2018.

[111] Niraj Kumbhare, Reza Moheimani, and Hamid Dalir. Analysis of composite structures in curing process for shape deformations and shear stress: basis for advanced optimization. *Journal of Composites Science*, 5(2):63, 2021.

[112] Min Li, Qi Zhu, Philippe H Geubelle, and Charles L Tucker III. Optimal curing for thermoset matrix composites: thermochemical considerations. *Polymer Composites*, 22(1):118–131, 2001.

[113] Pauli Virtanen, Ralf Gommers, Travis E Oliphant, Matt Haberland, Tyler Reddy, David Cournapeau, Evgeni Burovski, Pearu Peterson, Warren Weckesser, Jonathan Bright, et al. Scipy 1.0: fundamental algorithms for scientific computing in python. *Nature methods*, 17(3):261–272, 2020.

[114] William E Hart, Carl D Laird, Jean-Paul Watson, David L Woodruff, Gabriel A Hackebeil, Bethany L Nicholson, John D Siirola, et al. *Pyomo-optimization modeling in python*, volume 67. Springer, 2017.

[115] Sourabh Katoch, Sumit Singh Chauhan, and Vijay Kumar. A review on genetic algorithm: past, present, and future. *Multimedia Tools and Applications*, 80:8091–8126, 2021.

[116] G. Struzziero, J.J.E. Teuwen, and A.A. Skordos. Numerical optimisation of thermoset composites manufacturing processes: A review. *Composites Part A: Applied Science and Manufacturing*, 124:105499, 2019.

[117] Konstantinos Varelas and Marie-Ange Dahito. Benchmarking multivariate solvers of scipy on the noiseless testbed. In *Proceedings of the Genetic and Evolutionary Computation Conference Companion*, pages 1946–1954, 2019.

[118] Frederick Odien Daso. Manufacture of aerospace-grade thermoset and thermoplastic composites via nanoengineered thermal processing, 2019.

[119] Johns Manville. SUPER FIRETEMP® X Data Sheet. Downloaded July 11, 2023 from https://www.jm.com/content/dam/jm/global/en/industrial-insulation/calcium-silicate/super-firetemp-x/JM_IND_Super_FireTemp_X_DS.pdf.

[120] Olli Tuominen, Eero Tuominen, Maarit Vainio, Tiina Ruuska, and Juha Vinha. Thermal and moisture properties of calcium silicate insulation boards. In *MATEC Web of Conferences*, volume 282, page 02065. EDP Sciences, 2019.

[121] Nuri Ersoy, Tomasz Garstka, Kevin Potter, Michael R Wisnom, David Porter, and Graeme Stringer. Modelling of the spring-in phenomenon in curved parts made of a thermosetting composite. *Composites Part A: Applied Science and Manufacturing*, 41(3):410–418, 2010.

[122] Ernani Sartori. Convection coefficient equations for forced air flow over flat surfaces. *Solar Energy*, 80(9):1063–1071, 2006.

[123] Martin Szarski and Sunita Chauhan. Composite temperature profile and tooling optimization via deep reinforcement learning. *Composites Part A: Applied Science and Manufacturing*, 142:106235, 2021.

[124] Dilmurat Dolkun, Han Wang, Haijin Wang, and Yinglin Ke. An efficient thermal cure profile design method for autoclave curing of large size mold. *The International Journal of Advanced Manufacturing Technology*, 114:2499–2514, 2021.

[125] Richard H Byrd, Peihuang Lu, Jorge Nocedal, and Ciyou Zhu. A limited memory algorithm for bound constrained optimization. *SIAM Journal on scientific computing*, 16(5):1190–1208, 1995.

[126] Ciyou Zhu, Richard H Byrd, Peihuang Lu, and Jorge Nocedal. Algorithm 778: L-BFGS-B: Fortran subroutines for large-scale bound-constrained optimization. *ACM Transactions on mathematical software (TOMS)*, 23(4):550–560, 1997.

[127] Rainer Storn and Kenneth Price. Differential evolution--a simple and efficient heuristic for global optimization over continuous spaces. *Journal of global optimization*, 11:341–359, 1997.

[128] Helio JC Barbosa, Afonso CC Lemonge, and Heder S Bernardino. A critical review of adaptive penalty techniques in evolutionary computation. *Evolutionary constrained optimization*, pages 1–27, 2015.

[129] Pascal Hubert, Andrew Johnston, Anoush Poursartip, and Karl Nelson. Cure kinetics and viscosity models for hexcel 8552 epoxy resin. In *International SAMPE symposium and exhibition*, pages 2341–2354. SAMPE; 1999, 2001.

[130] D Kim and SR Nutt. Effective cure cycle development via flow optimization and advanced cure environments. *Advanced Manufacturing: Polymer & Composites Science*, 6(3):164–172, 2020.

[131] David Van Ee and Anoush Poursartip. Hexply 8552 material properties database for use with compro cca and raven. *Version 0.9. NCAMP. Wichita, KS*, 2009.

[132] ASTM Committee D-30 on Composite Materials. *Standard Test Method for Glass Transition Temperature (DMA Tg) of Polymer Matrix Composites by Dynamic Mechanical Analysis (DMA).* ASTM International, 2016.

[133] ASTM Committee D-30 on Composite Materials. *Standard test method for short-beam strength of polymer matrix composite materials and their laminates.* ASTM International, 2022.

[134] Xinchen Ni, Carolina Furtado, Estelle Kalfon-Cohen, Yue Zhou, Gabriel A Valdes, Travis J Hank, Pedro P Camanho, and Brian L Wardle. Static and fatigue interlaminar shear reinforcement in aligned carbon nanotube-reinforced hierarchical advanced composites. *Composites Part A: Applied Science and Manufacturing*, 120:106–115, 2019.